AD
A065490

Author: Richard R. Babcock, Jr.
Title: The Dependence of the Circulation of the Termosphere on
        Solar Activity
Rank and Service: Captain, USAF
Number of pages: 191
Degree: Ph.D.
Institution: Massachusetts Institue of Technology

ABSTRACT

Incoherent scatter radar measurements of the ionospheric electron density, electron and ion temperature, and vertical ion drift made at the Millstone Hill Observatory (42.6°N, 71.5°W) were used to derive the neutral temperature and a measure of the neutral winds in the mid-thermosphere. Neutral densities for all calculations were taken from the MSIS model of Hedin et al (1977). The experimental data was applied to the dynamic model of Emery (1978) to obtain the diurnal patterns of the zonal and meridional winds.

Over the six year period 1970, near solar maximum, through 1975, at solar minimum, 83 days of diurnally averaged winds were examined to determine if there was a change in the seasonal variation in the circulation as solar activity decreased. It was found that the magnitude of the seasonal variation in both the zonal and meridional winds remains about the same, although the winter averaged winds become more poleward near solar minimum, consistent with the model of Roble et al (1977).

For several geomagnetically disturbed days examined, it was found that the diurnal wind pattern was significantly different from quiet days. The nighttime meridional winds were markedly stronger equatorward and the zonal winds tended to be more westward. Also, the neutral temperature showed periods of large enhancement during the night, indicative of the transport of auroral heating to mid-latitudes by the strong winds. There was a consistent evidence of an equatorward surge in the meridional winds near local midnight on disturbed days.

In the analysis procedures, it was demonstrated that frictional heating by the neutrals is an important factor in deriving the neutral temperature from the ion heat balance equation. It was also shown that electric field effects are important in the derivation of winds during disturbed periods.

References:

Emery, B.A., 1978; Neutral winds deduced above Millstone Hill: II. seasonal winds variations, 1970-1971, submitted to JGR.

Evans, J.V., 1976; The dynamics of the ionosphere and upper atmosphere, Proc Intl Symp STP, Boulder, CO, Voll II, 630.

Hedin, A.E. et al, 1977; A global thermospheric model based on mass spectrometer and incoherent scatter data (MSIS), 2, composition, J. Geophys. Res., 82, 2148.

Roble, R.G. et al, 1977; Seasonal and solar cycle variations of the zonal mean circulation in the thermosphere, J. Geophys. Res., 82, 5493.

79 02 26 233

REPORT DOCUMENTATION PAGE		READ INSTRUCTIONS BEFORE COMPLETING FORM
1. REPORT NUMBER CI79-78D	2. GOVT ACCESSION NO.	3. RECIPIENT'S CATALOG NUMBER
4. TITLE (and Subtitle) The Dependence of the Circulation of the Termosphere on Solar Activity		5. TYPE OF REPORT & PERIOD COVERED Disseratation
		6. PERFORMING ORG. REPORT NUMBER
7. AUTHOR(s) Captain Richard R. Babcock, Jr.		8. CONTRACT OR GRANT NUMBER(s)
9. PERFORMING ORGANIZATION NAME AND ADDRESS AFIT student at the Massachusetts Institute of Technology		10. PROGRAM ELEMENT, PROJECT, TASK AREA & WORK UNIT NUMBERS
11. CONTROLLING OFFICE NAME AND ADDRESS AFIT/CI WPAFB OH 45433		12. REPORT DATE September 1978
		13. NUMBER OF PAGES 191
14. MONITORING AGENCY NAME & ADDRESS(if different from Controlling Office)		15. SECURITY CLASS. (of this report) UNCLASSIFIED
		15a. DECLASSIFICATION/DOWNGRADING SCHEDULE

16. DISTRIBUTION STATEMENT (of this Report)

Approved for Public Release, Distribution Unlimited

17. DISTRIBUTION STATEMENT (of the abstract entered in Block 20, if different from Report)

18. SUPPLEMENTARY NOTES
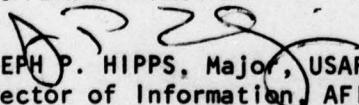
FEB 8 1979

JOSEPH P. HIPPS, Major, USAF
Director of Information, AFIT

19. KEY WORDS (Continue on reverse side if necessary and identify by block number)

20. ABSTRACT (Continue on reverse side if necessary and identify by block number)

DD $_{1\ JAN\ 73}^{FORM}$ 1473   EDITION OF 1 NOV 65 IS OBSOLETE

THE DEPENDENCE OF THE CIRCULATION OF THE
THERMOSPHERE ON SOLAR ACTIVITY.

by

RICHARD ROBERT BABCOCK, JR.

B.S., College of William and Mary
1967

M.S., University of Michigan
1972

AFIT-CI-79-78D

SUBMITTED IN PARTIAL FULFILLMENT
OF THE REQUIREMENTS FOR THE
DEGREE OF

DOCTOR OF PHILOSOPHY

Doctoral
thesis

at the

MASSACHUSETTS INSTITUTE OF TECHNOLOGY

SEPTEMBER, 1978

Signature of Author..
Department of Meteorology, August 16, 1978

Certified by..
Thesis Supervisor

Accepted by...
Chairman, Departmental Committee on Graduate Students

1

79 02 26 233

THE DEPENDENCE OF THE CIRCULATION OF THE
THERMOSPHERE ON SOLAR ACTIVITY

by

Richard Robert Babcock, Jr.

ABSTRACT

Incoherent scatter radar measurements of the ionospheric parameters electron density, electron and ion temperature, and vertical ion drift made above the Millstone Hill Observatory (42.6°N, 71.5°W, 57°N invariant latitude) are used to derive the neutral parameters of exospheric temperature, T_∞, and the horizontal component of the neutral wind along the magnetic meridian. These data were used in a semi-empirical dynamic model of Emery(1977) to calculate the zonal and meridional winds in the thermosphere. Neutral densities required in the calculations were derived from the mass spectrometer/incoherent scatter (MSIS) model of Hedin et al (1977).

The present analysis included data taken in 1972 through 1975 to which was added the 37 days in 1970-1971 analyzed by Emery (1977) to *give 83 days of observations over the six year period 1970*, near solar cycle maximum, through 1975, at solar minimum. The dynamic model integrates the momentum equations over a 24 hour period in the height range 120 to 600 km The primary output from the model is diurnal wind patterns at 300 km and the diurnally averaged mean of each component at 300 km.

Considering the changes in the seasonal variation of the diurnally averaged winds, it was found that the annual variation in both the meridional and zonal velocities stayed about the same through the solar cycle, at 57 and 30 m/sec, respectively. The annual mean meridional wind did decrease from 15 m/sec equatorward near solar maximum to about 0 m/sec at solar minimum. The annual mean zonal wind stayed about the same at 2—3 m/sec westward. The approximately constant value of the annual mean, and the increase in the poleward mean wind in winter near solar minimum are consistent with the model predictions of Roble et al (1977). A comparison of the diurnally averaged winds with the auroral electrojet (AE) index showed a generally linear trend of more   westward average winds as AE increases. Near equinox the meridional winds showed a weak trend of more equatorward average winds as AE increased, but the complete data set showed no statistically significant trend.

The solar cycle variation analysis did not consider electric field-induced ion drifts in any of the calculations. A series of moderately disturbed days (AE $\geq$ 300) was analyzed using a "disturbed" model electric field. For one disturbed day, there were coincident electric field

observations which could be applied. The frictional heating of the ions by the neutral wind was included in the derivation of T_∞ from the ion heat balance equation. Although the diurnally averaged winds did not follow the correlation with AE as consistently as the less disturbed days, the diurnal wind pattern showed clear evidence of increased equatorward winds during the nighttime. All the days also exhibited some enhancement of the nighttime temperature, indicative of a deposition of heat from high latitudes by the winds. Three distinct features could be seen in the derived meridional winds, viz. i) enhanced equatorward winds at night which reflect a planetary scale response to the high latitude heating, ii) an equatorward surge in the winds near local midnight that is probably an extension of the midnight surge seen by Bates and Roberts (1977a) at Chatanika, and iii) equatorward pulses in the winds and increases in T_∞ associated with large scale gravity waves initiated by onset of separate auroral substorms.

For the one disturbed day for which coincident electric field data was available, comparison of the winds computed with and without electric fieldinduced ion drifts showed a clear difference in the structure of the diurnal pattern of both components. For the diurnally averaged winds, the meridional wind showed only a small difference of a few m/sec, while the zonal wind was much more westward when the electric field was included.

Name and Title of Thesis Advisor:

John V. Evans   Senior Lecturer

3

ACKNOWLEDGEMENTS

4

TABLE OF CONTENTS

LIST OF FIGURES

8

9

10

LIST OF TABLES

1. INTRODUCTION

1.1 General Description and Definitions

1.1.1 The Neutral Atmosphere

The thermosphere is that region of the atmosphere above the mesopause extending from about 80 km to 600 km. As shown in Figure 1.1, the neutral temperature profile has a minimum at the mesopause of about $180^{\circ}K$ and increases rapidly to reach a limiting value, known as the exospheric temperature, T_{∞}. The height at which the vertical temperature gradient becomes essentially zero is called the thermopause. A region above which there is a constant temperature arises because the molecular thermal conductivity eventually becomes very large and can readily redistribute the small amount of heat absorbed above this level.

The dominant energy source for the thermosphere, and the reason for the large temperature gradient, is the absorption of solar extreme ultraviolet (EUV), most of which is absorbed in the region between 100 and 200 km. There are no efficient radiators in the thermosphere so most of the absorbed energy is transported downward, either by thermal conduction or by diffusion in the form of potential chemical energy.

The intensity of the solar EUV, most of which is absorbed in the thermosphere, has much larger variations than the intensity of the visible spectra which reaches the surface. The total EUV flux is well correlated with the 10.7 cm solar radio flux, and exhibits two basic fluctuations, the 27-day variation associated with the rotation of the sun, and the 11-year sunspot cycle. There are fluctuations within these periods associated with increases in activity over a period of days and

12
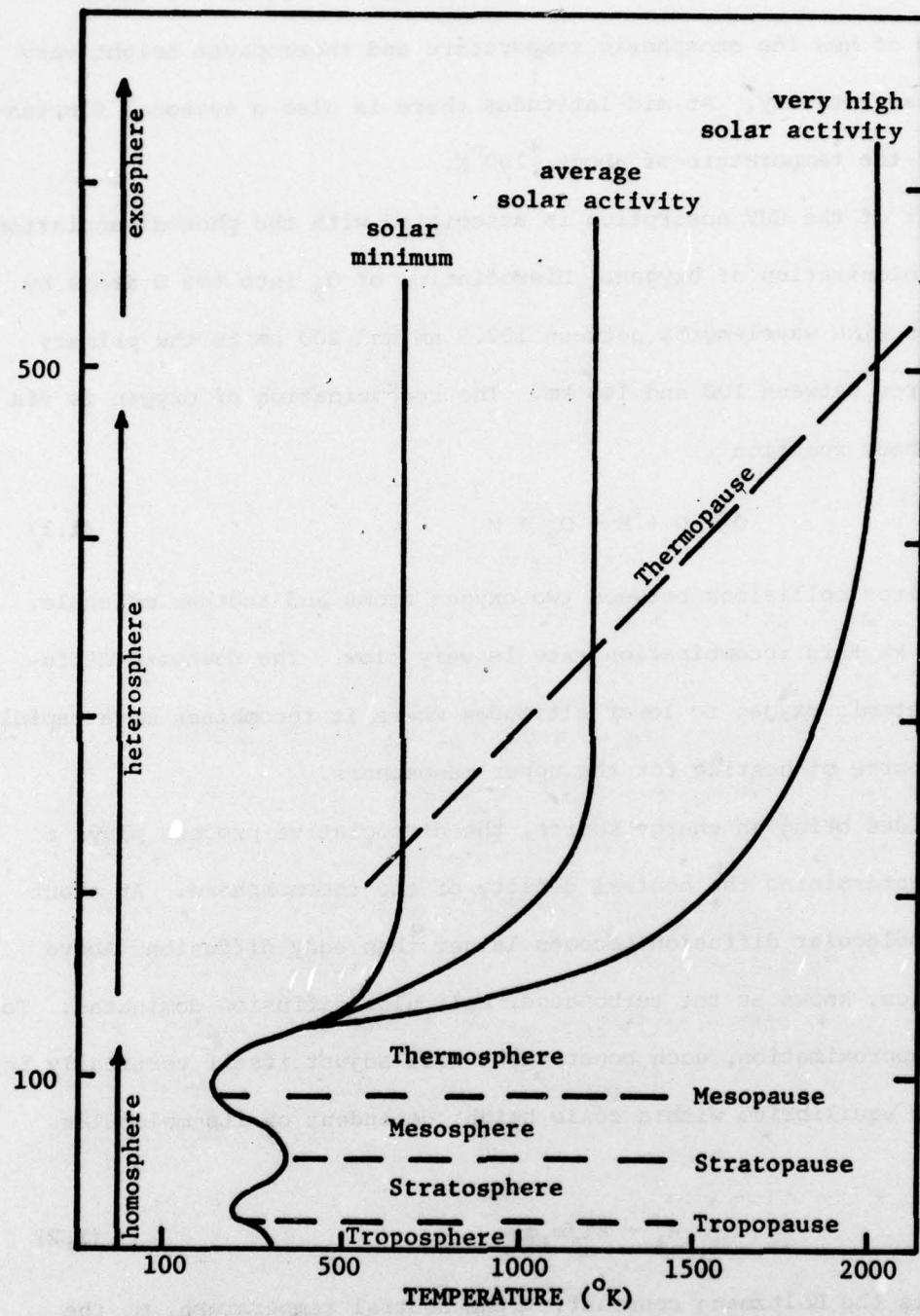
Figure 1.1 Vertical distribution of temperature in the atmosphere.

13

with the short-time events such as solar flares. Figure 1.1 shows examples of how the exospheric temperature and thermopause height vary with solar activity. At mid-latitudes there is also a seasonal fluctuations of the temperature of about $\pm 100^{\circ} K$.

Most of the EUV absorption is associated with the photodissociation and photoionization of oxygen. Dissociation of O_2 into two O atoms by radiation with wavelengths between 102.5 nm and 200 nm is the primary heat source between 100 and 140 km. The recombination of oxygen is via a three body reaction

$$O + O + M \rightarrow O_2 + M \qquad (1.1)$$

and requires collisions between two oxygen atoms and another molecule. Above 90 km this recombination rate is very slow. The downward diffusion of atomic oxygen to lower altitudes where it recombines more rapidly is one source of heating for the upper mesosphere.

Besides being an energy source, the dissociative process plays a role in determining the neutral density of the thermosphere. At about 110 km, molecular diffusion becomes larger than eddy diffusion. Above this region, known as the turbopause, molecular diffusion dominates. To a first approximation, each constituent will adjust itself vertically in diffusive equilibrium with a scale height dependent on its molecular weight

$$H_i = kT/m_i g \qquad (1.2)$$

where k is the Boltzmann constant, T the neutral temperature, m_i the mass of the ith constituent, and g the gravitational acceleration. At the turbopause, N_2 and O_2 are the dominant species, with atomic oxygen

14

being a minor constituent. Because atomic oxygen has about twice the scale height of the molecular constituents, it becomes the major constituent above about 150 km (Figure 1.2). At still higher heights, in the region known as the exosphere, He and H become dominant.

The exosphere is that region where the neutral collision frequency is low enough that particles whose thermal velocity is larger than the escape velocity (11.4 km/sec) are able to escape from the atmosphere. Below this region collisions are frequent enough to maintain a Boltzmann energy distribution and the fluid equations can be used to describe the atmosphere. The "exobase" is generally about 600 km.

1.1.2 The Ionosphere

Photons with wavelengths shorter than 102.5 nm can cause photoionization of the neutral atoms and molecules. The region of the atmosphere where the density of these ions is large enough to effect radio transmission is known as the ionosphere and extends from about 60 km upward to a height at the base of the magnetosphere, generally considered to be about 1000 km. As shown in Figure 1.3, the peak ion density occurs at a mid-thermospheric altitude of about 300 km. Photoionization occurs over a broader height region than molecular dissociation, though peak production is centered at about 150 km. Molecular ions recombine with electrons fairly quickly, while the atomic ions have recombination rates about four orders of magnitude smaller. The atomic ions are more likely to react with a neutral molecule to form a molecular ion, e.g.

$$O^+ + N_2 \rightarrow NO^+ + N \tag{1.3}$$

This reaction controls the ion concentration profile. As shown in

15
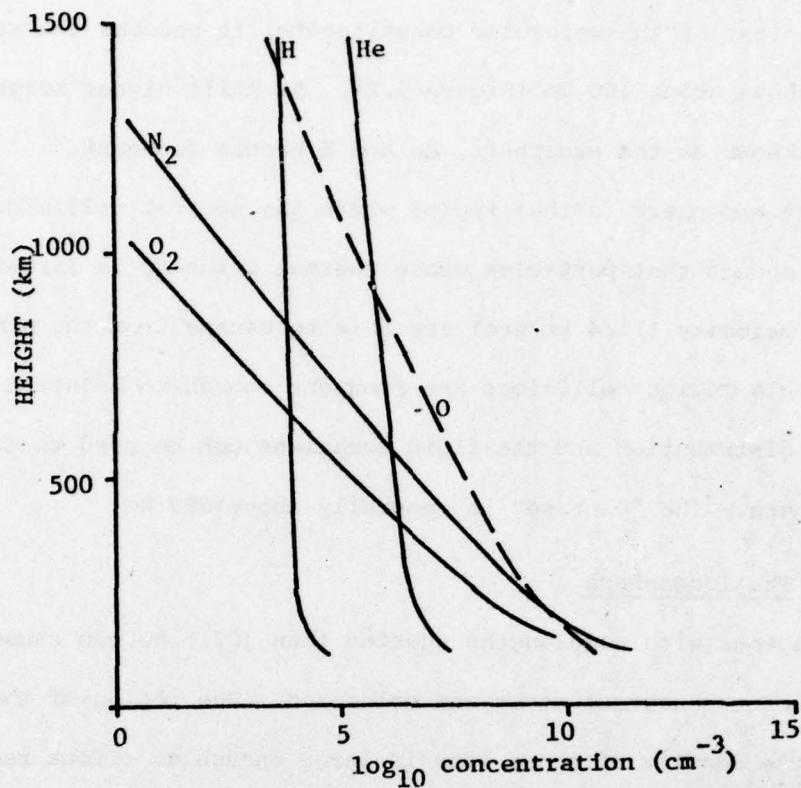
Figure 1.2 Vertical profile of main thermospheric constituents.
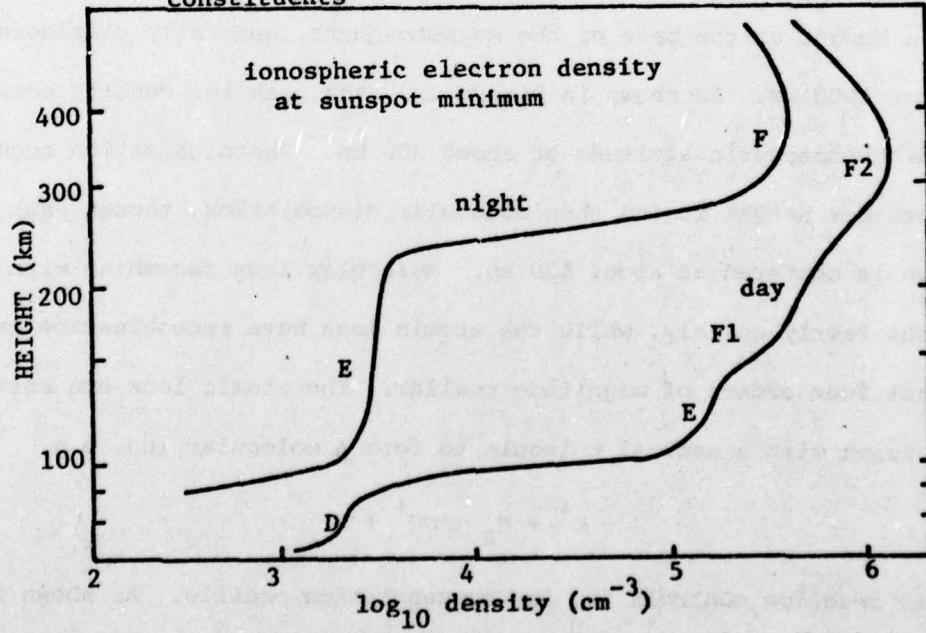
Figure 1.3 An idealized electron density distribution of the ionosphere at sunspot maximum for a typical mid-latitude station.

16

Figure 1.4, molecular ions O_2^+ and NO^+ are the dominant ions in the E region of the ionosphere (100 - 150 km) where the neutral molecular constituents are relatively abundant. Above about 180 km, the molecular densities are too small to significantly affect the ion composition, and O^+ becomes the dominant ion. Above about 1000 km, H^+ becomes dominant. The effect of this atomic-molecular ion separation on the diurnal variation of the ionosphere is depicted in the sample profiles in Figure 1.3. At night the rapid recombination of the molecular ions results in the E region almost completely dissappearing. At F region altitudes the recombination rate of O^+ is much slower, and the nighttime decrease at the peak is as much due to downward diffusion as to recombination. The presence of a maximum in the electron density near 300 km represents a balance between the downward diffusion of ions from F région heights, where the photoionization rate is higher than the recombination rate, and the loss due to charge exchange. Because the ionospheric structure is so dependent on the relative abundance of atomic and molecular constituents and their ratios, it should be clear that any dynamical process which changes the density profiles of the various neutral constituents will have a profound effect on the ionosphere.

In the absence of other forces, a charged particle in a magnetic field will revolve about the field line with an angular frequency given by

$$\omega = qB/m \qquad (1.4)$$

where q isthe charge of the particle, m is its mass, and B the field strength. Below about 120 km, the gyrofrequency is less than the ion-

17
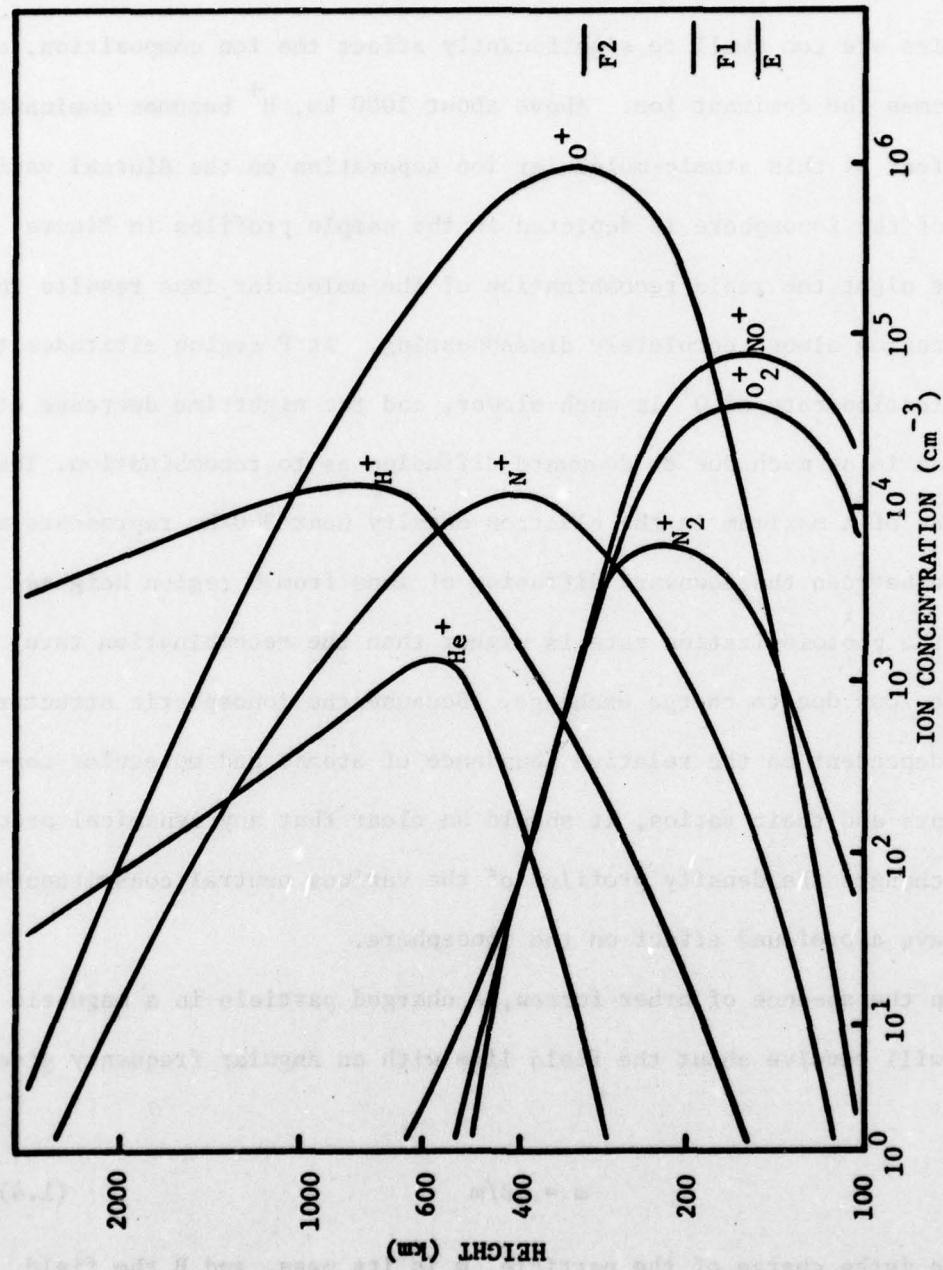
Figure 1.4 Profiles of ion concentration of ionospheric daytime conditions.

neutral collision frequency, ν_{in}, so that ions are not forced to spiral around the field lines and will move across the field lines with the horizontal winds. Above 120 km, $\omega > \nu_{in}$, so it can be assumed the ions are constrained to move up and down the magnetic field lines. For electrons $\omega \simeq \nu_{en}$ at 90 km.

1.2 Purpose of this Research

The primary purpose of this research has been to expand the data base of experimental observations of F region thermospheric winds, and improve our understanding of the dynamics of the thermosphere. Using the data base, an analysis can then be made of the effect fluctuations in solar activity have on the thermospheric circulation, and the results can be compared with theoretical models and other observations.

Although absorption of solar EUV is the primary driving force for the thermospheric winds, the deposition of solar wind energy in the form of Joule heating and particle precipitation into high latitudes can be more intense per unit volume, albeit over a smaller portion of the earth's surface. Such relatively large amounts of energy deposited over a small range of latitude can have dramatic effects on the winds on a global scale. The transport of this high latitude heating by the winds to lower latitudes and the accompanying redistribution of the neutral constituents can also have global effects.

There have been two basic goals of the analysis presented here. The first is to extend the results obtained by Emery (1977) for the years 1970 1971 through 1975 to determine if there is any variation in the diurnally averaged mid-latitude winds as solar activity decreases. This

19

six year period extends from near solar cycle maximum to solar cycle minimum. Emery placed particular emphasis on the seasonal variation. Ionospheric variations over the solar cycle suggest that these seasonal variations should exhibit a change with sunspot cycle. Also, the semi-empirical model of Roble et al (1978) predicts a change in the strength of the circulation. The results obtained here permit these predictions to be tested.

A second goal has been to examine the effect of high latitude heating on the mid-latitude circulation, both generally, in terms of changes in the zonally averaged winds, and more specifically, in the changes in the diurnal circulation pattern, including electric field effects, and how these variations can be related to different high latitude phenomena. These differences will be related to observed ionospheric changes and satellite measurements of variations in neutral density.

The primary data source for this research is measurements of the ionospheric parameters electron density, electron and ion temperature, and vertical ion drift between 225 and 1000 km made at the Millstone Hill Incoherent Scatter Radar (42.6° N, 71.5° W, 57° N invariat latitude) located in Westford, MA.

Chapter 2 gives a brief review of thermospheric dynamics and current understanding of the effects of geomagnetic disturbances. Chapter 3 describes the theory and practice of incoherent scatter radar observations and the specific data that is gathered at the Millstone Hill Radar. The procedure used to derive neutral parameters from the iono-

20

spheric measurements is explained in Chapter 4 along with a brief description of the model used to compute neutral winds. New types of data and new analysis techniques which were included in this research are discussed in Chapter 5. The results of the solar cycle variation in the seasonal pattern of the F region thermospheric circulation are presented in Chapter 6 with a comparison with other measurements and models. The deviation of the diurnally averaged winds from the normal pattern caused by high latitude events is also presented. In Chapter 7 there is a detailed examination of how the diurnal wind pattern changes during geomagnetic disturbances. Chapter 8 provides a summary and suggestions for future work.

21

2. REVIEW OF THERMOSPHERIC DYNAMICS

2.1 Models of the Global Circulation

In the early 1960's, the developement of global models of the thermospheric neutral density and temperature deduced from satellite drag observations provided an opportunity to make a theoretical analysis of the F-region circulation. Using diurnal temperature and density variations derived from the atmospheric model of Jacchia (1965) to compute the pressure force and a simple model of the ion densities, Kohl and King (1967) and Geisler (1967) developed semi-empirical models to calculate neutral winds using the linearized equations of motion. These equations included two terms not normally included in models of the troposphere and middle atmosphere. The first was an ion drag term. Since the ions are bound to the magnetic field lines at F-region altitudes, they impede the motion of the neutral wind across the field lines via ion-neutral collisions. The second was the molecular viscosity term, with the vertical gradient of horizontal velocity being the most significant. Viscosity is not important in the balance of forces, but it establishes the upper boundary condition. The exponential growth of the coefficient of molecular viscosity with height requires that $\partial U/\partial z \to 0$ as $z \to 600$ km, their upper boundary. The lower boundary condition was $U = 0$ at $z = 120$ km. (This is not thought to be the real situation, but better boundary conditions were not known.)

The basic results of these two models was to establish the importance of ion drag in thermospheric dynamics. The first order balance in the momentum equation is between the pressure and the ion drag terms.

GLOBAL WIND FIELD
HEIGHT 300 KM SOLSTICE
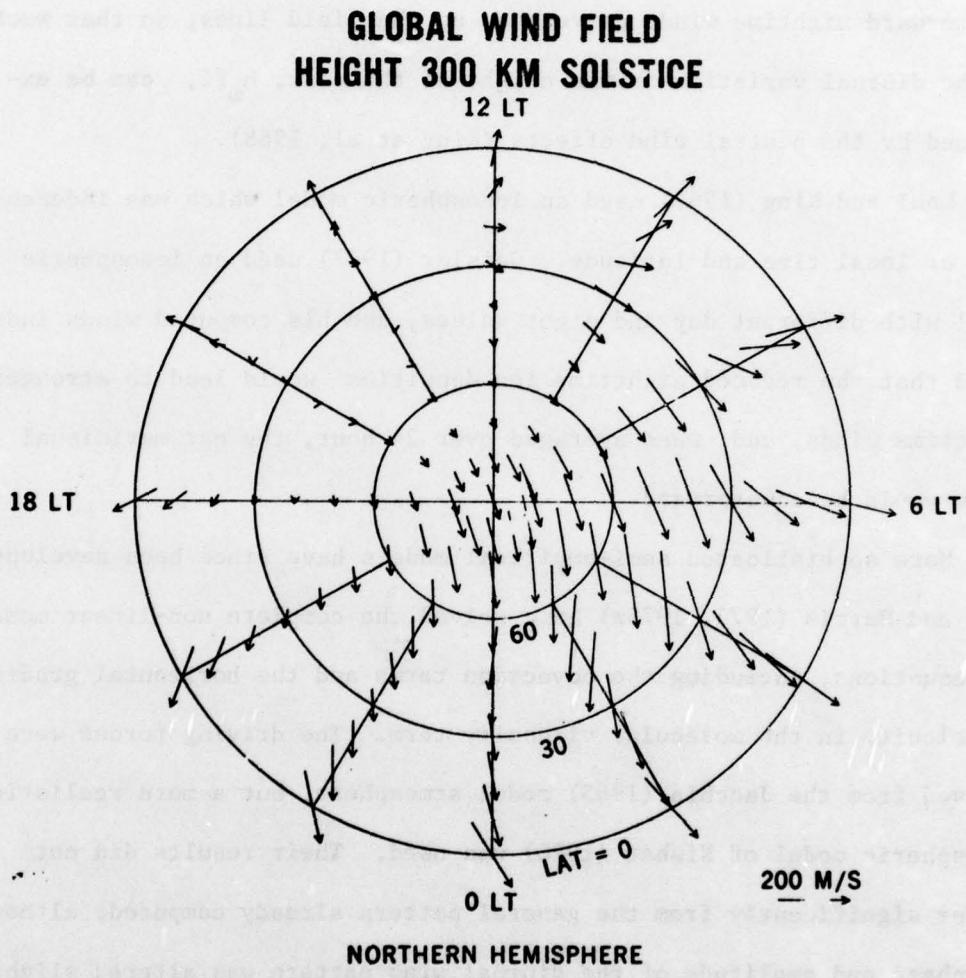
Figure 2.1 Depiction of the day-to-night global thermospheric wind pattern. (From Blum and Harris, 1975).

Rather than a geostrophic flow, as in the lower atmosphere, the thermospheric winds blow in great circle paths along the pressure gradient from the high pressure on the day side to the low pressure on the night side (Figure 2.1). One effect of these F-region winds is that the poleward daytime winds drive the ions down the field lines while the equatorward nighttime winds drive them up the field lines, so that much of the diurnal variation in the height of the peak, $h_m F2$, can be explained by the neutral wind effects (King et al, 1968).

Kohl and King (1967) used an ionospheric model which was independent of local time and latitude. Geisler (1967) used an ionospheric model with different day and night values, and his computed winds indicated that the reduced nighttime ion densities would lead to stronger nighttime winds, and, when averaged over 24 hour, the net meridional winds would be equatorward.

More sophisticated semi-empirical models have since been developed. Blum and Harris (1975, 1975a) have solved the complete non-linear momentum equations, including the advection terms and the horizontal gradients of velocity in the molecular viscosity term. The driving forces were derived from the Jacchia (1965) model atmosphere, but a more realistic ionospheric model of Nisbet (1970) was used. Their results did not differ significantly from the general pattern already computed, although the phase and amplitude of the diurnal wind pattern was altered slightly by the non-linear effects. One interesting observation was the inverse relationship between the strength of the winds and the solar activity. With decreasing $F_{10.7}$, the ion densities decreased, which meant a smaller

24

ion drag coefficient and larger velocities required to balance the
pressure force. This result was probably due to the relative simplicity
of the atmospheric and ionospheric models. As has been found in more
recent models and as will be shown in this research, such an increase in
the winds apparently does not occur. Using a Galerkin method to solve
the momentum equations, Creekmore et al (1975) employed an improved
Jacchia (1971) model and a newer global ionospheric model of Ching and
Chiu (1973) in calculations which also confirmed the earlier results.

The Jacchia model assumes the diurnal temperature and density
variations were coincident. Incoherent scatter results, however, have
shown that the temperature maximum occurred 2 - 3 hours after the pressure
maximum (Salah and Evans, 1973). It was suggested that the transport of
heat from the region of highest temperature by the winds could account
for this effect. This was explored by Straus et al (1975), who derived
the pressure force in a self-consistent manner using the solar EUV flux
to compute the temperature variation. They found a phase difference
between the temperature and density maximums in the afternoon, with the
temperature maximum occurring an hour or more later than the density
maximum. As discussed below, it is now believed that the transport of
light constituents (O and He) from the most heated regions towards
cooler regions is the major contributor to this phase difference.

Straus et al (1975) also found that the observed EUV flux was too
small to reproduce the winds calculated using the semi-empirical model,
and in particular, the model could not reproduce the day-night asymmetry
in the meridional winds. Compared to observations, the meridional

25

pressure gradients were too strong (the pole was too cold), and the diurnal temperature variation was too large, suggesting the presence of another heat source (specifically Joule heating) at high latitudes. To test the effect of the Joule heating, Straus et al (1975a) added a simple parameterization of high latitude heating to the model. With the addition of this heat source, the pressure gradients and calculated winds were brought into better agreement with previous empirical models, and the redistribution of the high latitude heating to lower latitudes through adiabatic warming brought the diurnal temperature variation into better agreement with observations.

One of the most sophisticated self-consistent models of the F-region energetics has been developed by Roble (1975). His model includes the most recent theoretical understanding of the photochemistry and heat balance of the F-region, including detailed calculations of heat transport and secondary ionization by fast photoelectrons, and of excess energy from chemical reactions. Roble found that observed EUV fluxes (Hinteregger, 1970,1976) were about a factor of two too small to reproduce observed electron, ion, and neutral temperatures. Dickinson et al (1975, 1977) and Roble et al (1977) used the neutral gas heating from a self-consistent model to compute the driving force for a model of the zonally averaged thermospheric circulation from the jointly solved dynamic equations of motion and the thermodynamic equations. A phenomenological model was used to describe the neutral density (first the OGO-6 model of Hedin et al (1974) and later, the improved Mass Spectrometer/Incoherent Scatter (MSIS) of Hedin et al (1977a,b)). The zonal

momentum force which arises from the asymmetry in the ion density and the ion drag was computed using the ionospheric model of Ching and Chiu (1973). High latitude Joule heating was derived from scaling a global estimate obtained by Roble and Matsushita (1975). The actual magnitude of the Joule heating was adjusted to give resultant winds which matched observations, in particular those at Millstone Hill. The results of Dickinson et al (1975,1977) considered the solstice and equinox circulations at solar maximum. Figure 2.2 shows the zonally averaged mass flow in one hemisphere for equinox, assuming only EUV heating at solar maximum. In Figure 2.3, the high latitude heating has been included and is seen to produce a large reverse circulation at the pole which results in a net equatorward flow at mid-latitudes. The size of this reverse cell is dependent on the magnitude of the Joule heating. On a global scale, the net transport at the F-region heights is balanced by a return flow in the lower thermosphere.

Roble et al (1977) included latitudinal variations in EUV flux and Joule heating to simulate the seasonal transition in the circulation. In Figures 2.4, the transition from the symmetrical equinoctial circulation to an asymmetric summer-winter pattern is shown to occur over a period of about three weeks. This suggests that a midlatitude station, such as Millstone Hill, should observe two basic circulation patterns at F-region heights: a winter pattern with weak poleward mean meridional flow, and a summer pattern with stronger equatorward mean meridional flow. At the transition around equinox, the length of the transition period was sensitive to the level of Joule heating, i.e. geomagnetic activity.

27
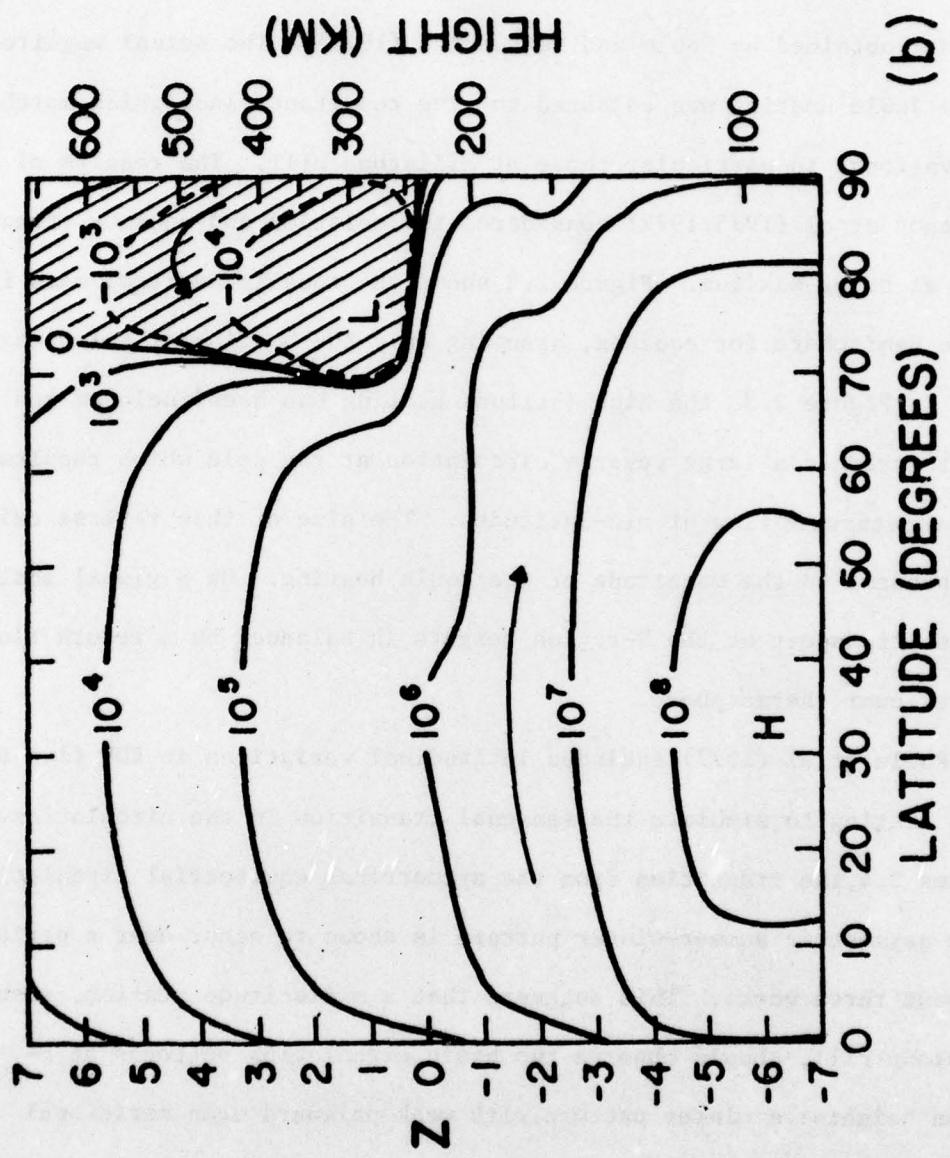
Figure 2.2 Zonally averaged meridional mass flow in the thermosphere at equinox with only EUV heating. (Dickinson et al, 1975)
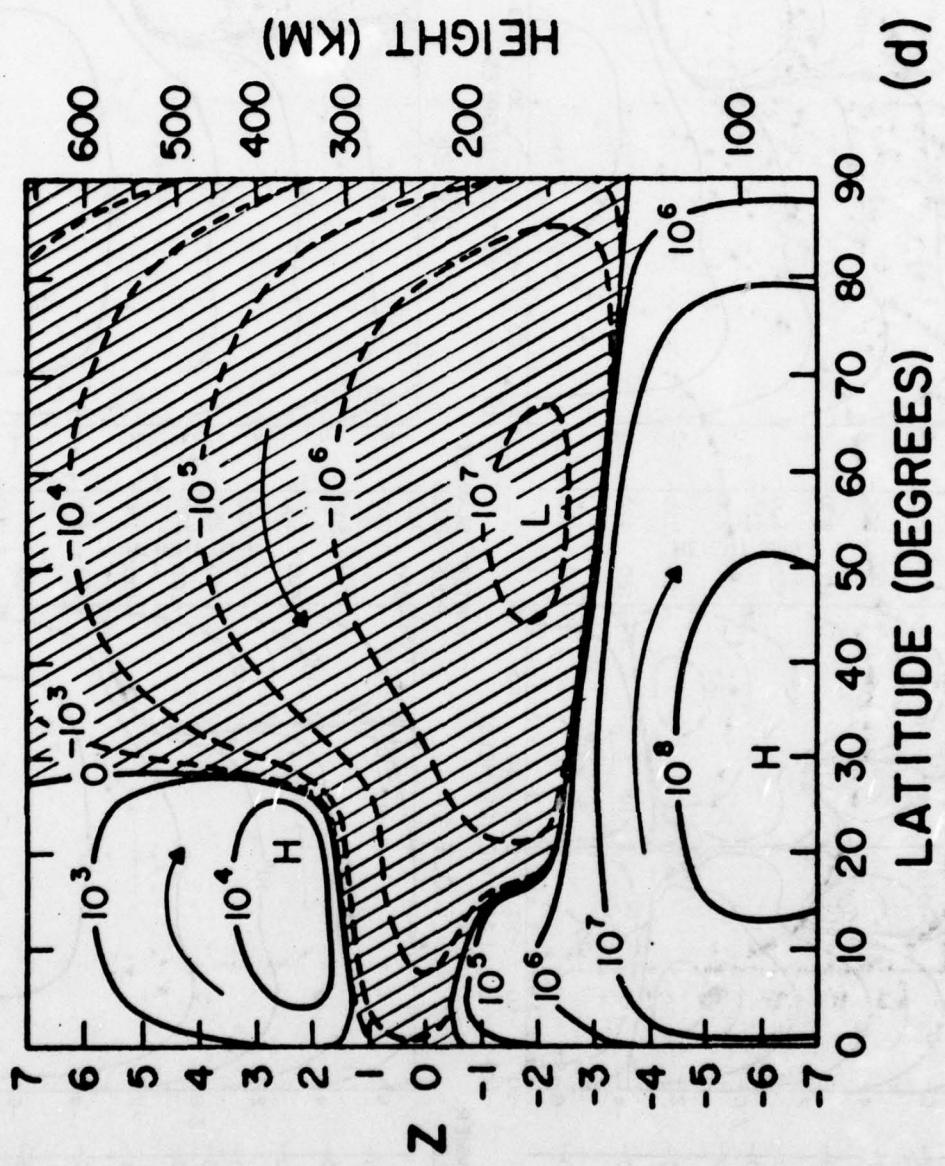
Figure 2.3 Same as Figure 2.2 except with Joule heating included.
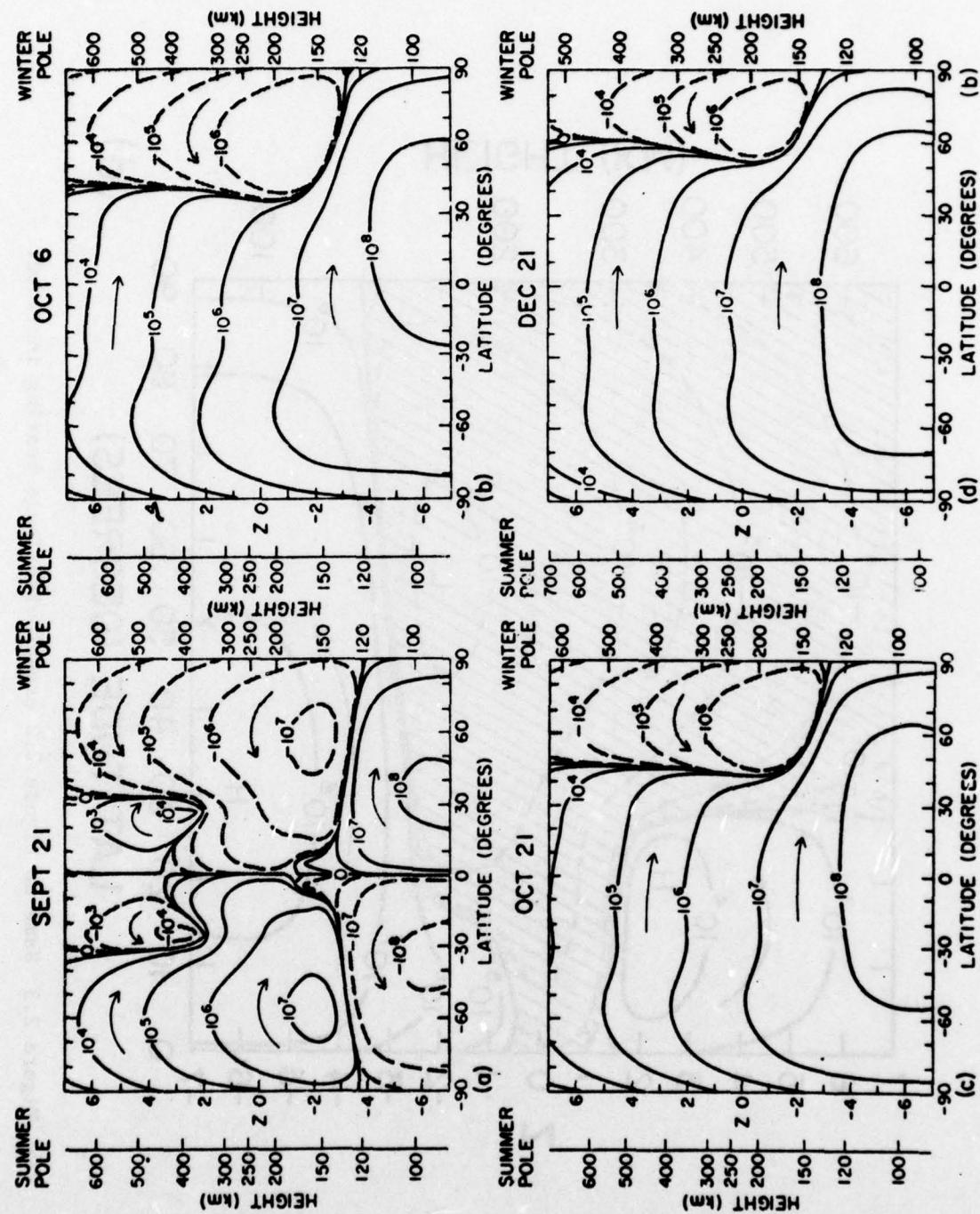
Figure 2.4 Depiction of transition from equinox to solstice circulation. (Roble et al, 1977).

30

Roble et al (1977) also examined the solar cycle effects on the circulation by varying the heating to simulate changes in the levels of solar and geomagnetic activity. At solar minimum conditions, with reduced EUV heating and reduced Joule heating, the model calculation for solstice showed the winds to be only slightly weaker than for solar maximum. The most significant difference at solar minimum was in the effect of the high latitude heating. The high latitude heat source in the winter hemisphere was too small to drive a reverse cell, so the global circulation becomes one large Hadley cell (Figure 2.5).

The nature of this thermospheric circulation has ramifications on the global composition at ionospheric heights. Since the density of the various constituents at any height is temperature dependent, the combination of higher temperatures (and hence densities) in the summer hemisphere and a net flow into the winter hemisphere results in the transport of the lighter constituents (primarily O and He) from the summer to the winter hemisphere. H. G. Mayr has termed this process "wind diffusion." Figure 2.6, taken from a review of thermospheric dynamics by Mayr et al (1978), gives a schematic picture of this process for the minor constituent helium. At F-region heights O and He densities are larger than N_2. Once the O and He are transported to the winter hemisphere, they will diffuse downward in order to reach diffusive equilibrium in the presence of the colder winter temperatures. The return flow from the winter to the summer hemisphere is in the lower thermosphere. Since O and He have larger scale heights, their transport in the F-region is not offset by an equal return flux in the E-region, and this difference can

31
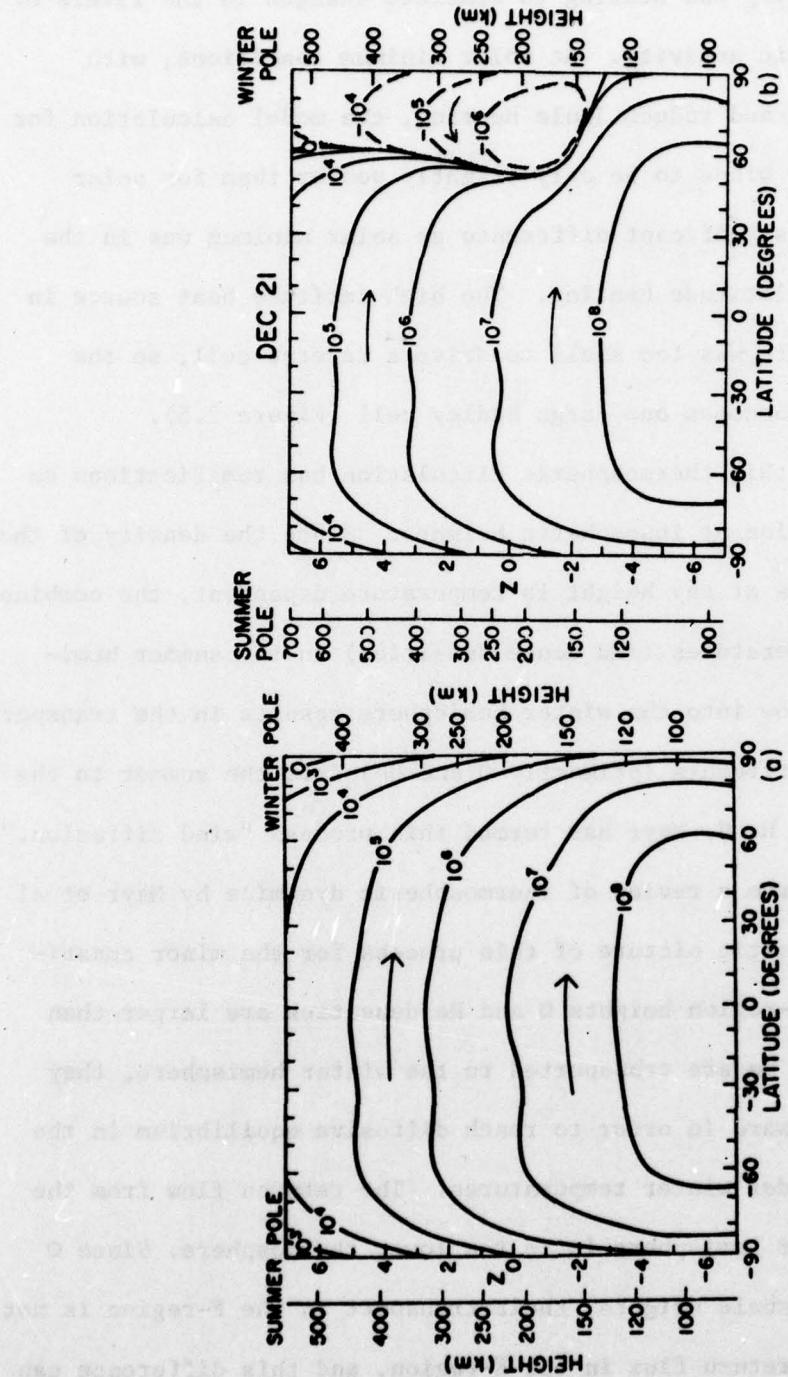
Figure 2.5 Comparison of the zonally averaged meridional mass flow at solstice for (a) solar minimum and (b) solar maximum conditions. (Roble et al, 1977).

WIND INDUCED DIFFUSION
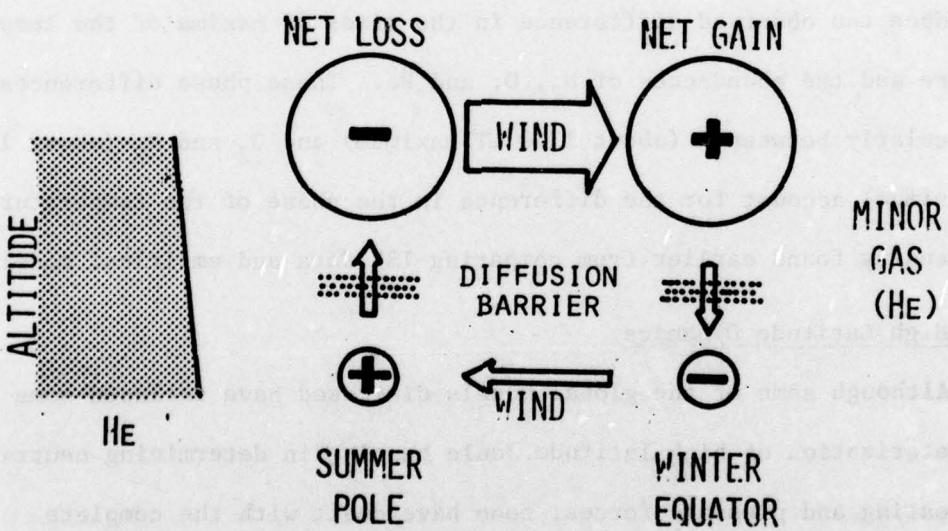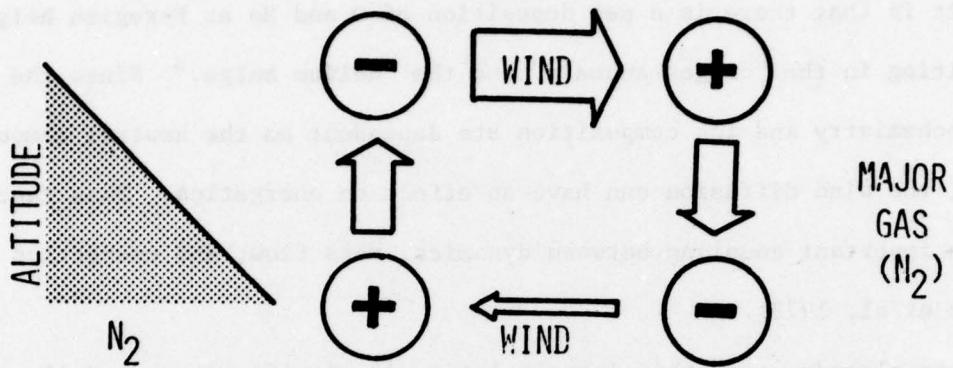
Figure 2.6   Schematic diagram depicting how wind induced diffusion results in a net transport of a minor constituent from the summer to the winter hemisphere. (From Mayr et al, 1978)

can be maintained because O and He will have to diffuse through the
heavier constituents (N_2), a process which is impeded by collisions. The
result is that there is a net deposition of O and He at F-region heights,
resulting in the "oxygen anomaly" and the "helium bulge." Since the
photochemistry and ion composition are dependent on the neutral composi-
tion, the wind diffusion can have an effect on energetics. Thus there
is an important coupling between dynamics, mass flow, and energetics
(Mayr et al, 1978).

As already noted this inter-relation is significant on a daily
basis as well. Using their own thermospheric model (Harris and Mayr,
1975), Mayr and Harris (1977) have examined the diurnal compositon
varations, including the effects of wind diffusion. They were able to
reproduce the observed diffference in the times of maxima of the temp-
erature and the abundances of N_2, O, and He. These phase differences,
particularly between O (about 1300 LT maximum) and O_2 and N_2 (about 1500
LT maximum) account for the difference in the phase of the temperature
and density found earlier from comparing ISR data and empirical models.

2.2 High Latitude Dynamics

Although some of the global models discussed have included some
parameterization of high latitude Joule heating in determining neutral
gas heating and pressure forces, none have dealt with the complete
dynamics and energetics in an explicit manner. In particular, the models
have ignored the effect of electric fields on the ion velocity. Assuming

34

that the ions are bound to the magnetic field lines is equivalent to saying that the ion velocity is zero in the local frame of reference, i.e. the field lines rotate with the earth. Electric fields ($\underline{E}$) which are perpendicular to the magnetic field ($\underline{B}$) produce an ion drift velocity which is perpendicular to both $\underline{E}$ and $\underline{B}$ ($E \times B$ drift). Since the ion drag term in the momentum equation and the Joule heating term in the thermodynamic equation depend on the difference between the neutral and ion velocities, a non-zero ion velocity will effect both these terms. At low and mid-latitudes, E-fields are primarily of dynamo origin on the dayside. The origin of the nightime fields is more complicated and as yet unclear, but the magnitude of the fields during most of the day is relatively small and the effect of the induced ion drift velocities is generally negligible. At high latitudes, the drift velocities are significant because of the large E-fields. During geomagnetic disturbances the drift velocities can be as large as 2000 m/sec, or more than twice the speed of sound for the neutral gas. A complete analysis of the high latitude dynamics must include the drift velocities in both the energy and momentum equations.

In the auroral regions and the polar cap, the magnetic field lines no longer corotate with the earth. Through the interaction of the earth's magnetic field and the interplanetary magnetic field (IMF) of solar origin, the high latitude field lines are convected anti-sunward across the polar cap by the solar wind and then return sunward in the auroral regions. Or equivalently, the convective electric fields created by the interaction of the earth's field and the IMF, plus the field

35

created by the corotation of the lower latitude field lines inside the magnetosphere, produces convective ion drift velocities. This magneto-spheric convection pattern consists of two vortices (Figure 2.7). In the dawn and dusk sectors the convective flow is against the normal day-to-night neutral wind circulation.

Straus and Schulz (1975) and Maeda (1976,1977) have developed three dimensional models of the high latitude region. Maeda solved the coupled ion and neutral momentum equations considering only ion drag momentum transfer in the neutral momentum equation. He found that the ion drift velocities were actually large enough in the dawn and dusk sectors to reverse the neutral wind flow at F-region altitudes. In fact, the neutral winds were essentially the same as the ion drift velocities, with a slight deflection due to the coriolis force, and a smaller magnitude, particularly at night when the ion densities are smaller.

The spectral model of Straus and Schulz (1975) not only included the effects of ion drag, but also the heating due to both solar EUV absorption and Joule heating, to obtain a self-consistent solution of the neutral gas momentum and energy equations. Their model also found that the convective ion drag force at auroral latitudes could reverse the normally eastward neutral winds in the dusk sector when the E-field was large enough ($E \geq 75$ mV/m). In the dawn sector, the ion density is decreased and so the ion drag has a smaller effect. Since the convective flow is essentially zonal at auroral latitudes, the effect of the ion drag is to decrease the meridional component of the wind. The model also produced large upward vertical velocities in the region of maximum

36

Joule heating, indicative of expansion of the thermosphere and adiabatic cooling. The increased equatorial winds and adiabatic warming due to subsidence at lower latitudes results in transport of the heat to lower latitudes and a global temperature increase (Straus, 1978). The response of this model to the effects of magnetospheric convection was less dramatic than models which only include one aspect of the problem, such as Maeda (1976, 1977), or Richmond and Matsushita (1975), who just looked at the effect of Joule heating. In his review of high latitude dynamics, Straus (1978) emphasizes that the complete dynamics, energetics and mass flow must be considered, since the total interaction will result in a redistribution of the steady-state pressure field and the computed winds. A clear understanding has not been developed of this complex problem. The fact that the auroral region dynamics is dependent on both local and universal time, further complicates the analysis.

2.3 Observations of the Thermosphere

Much of the earliest ideas concerning thermospheric dynamics were inferred from observations of the ionosphere. The diurnal variation in h_mF2 can be partially explained by the day-to-night global wind pattern, (E-fields also play a role in the lifting and depressing of the ionosphere.) The oxygen anomaly was first recognized from a variation in the peak density, N_mF2, with season, and the enhancement of oxygen in the winter hemisphere was proposed as an explanation, suggesting that there was a seasonal variation in the thermospheric circulation.

Even today there are only a few methods for measuring thermospheric winds. Barium or strontium cloud releases provide a means of observing

37
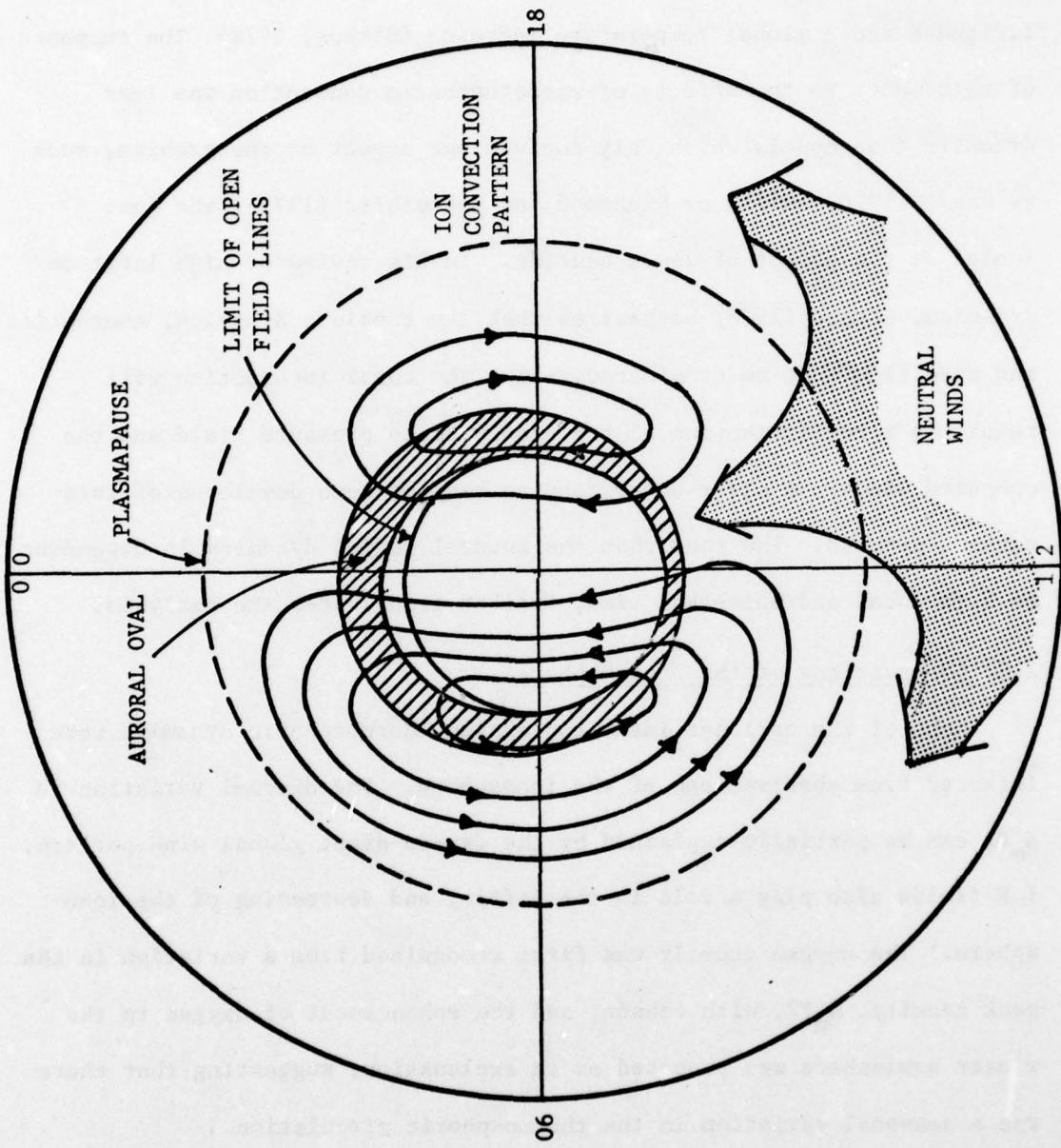
Figure 2.7 Qualitative view of the global winds, including the effects of electric fields, proposed by Fedder and Banks (1972).

38

both the neutral and ion velocities, but these experiments are limited to the dawn and dusk sectors or the high latitude regions of the summer hemisphere (Merriwether et al, 1973; Kelley et al, 1977). Nighttime measurements of the temperature and velocity can be derived from the Doppler broadening and shifting of the 6300Å atomic oxygen airglow using Fabry-Perot interferometers (Hays and Roble, 1971; Nagy et al, 1974). The maximum intensity for this line occurs at about 250 km. The component of the neutral wind along the magnetic meridian can be deduced from incoherent scatter radar (ISR) measurements (Vasseur, 1969; Evans, 1971,1972b). The neutral temperature can also be derived from the ISR measurements of ion and electron temperature. When these derived winds and temperatures are applied to a semi-empirical model, the meridional and zonal winds for the particular observing location can be calculated (Salah and Holt, 1974; Roble et al, 1974). Recently there have been a few satellite experiments to measure the winds directly, but the accuracy of these measurements is still uncertain (Spencer, private communication).

The results of these measurements have generally confirmed the model winds. In fact some of the models have been tuned to reproduce the observations, e.g. Dickenson et al (1975). The seasonal wind regimes have been seen in airglow measurements by Hernandez and Roble (1976) and in winds derived from ISR by Antonaides (1976), Roble et al (1977), and Emery (1977). Figure 2.8 compares the meridional wind measured at Millstone Hill for a winter and summer day. At midlatitudes in winter, the meridional winds are southward only for a few hours between 2200

39
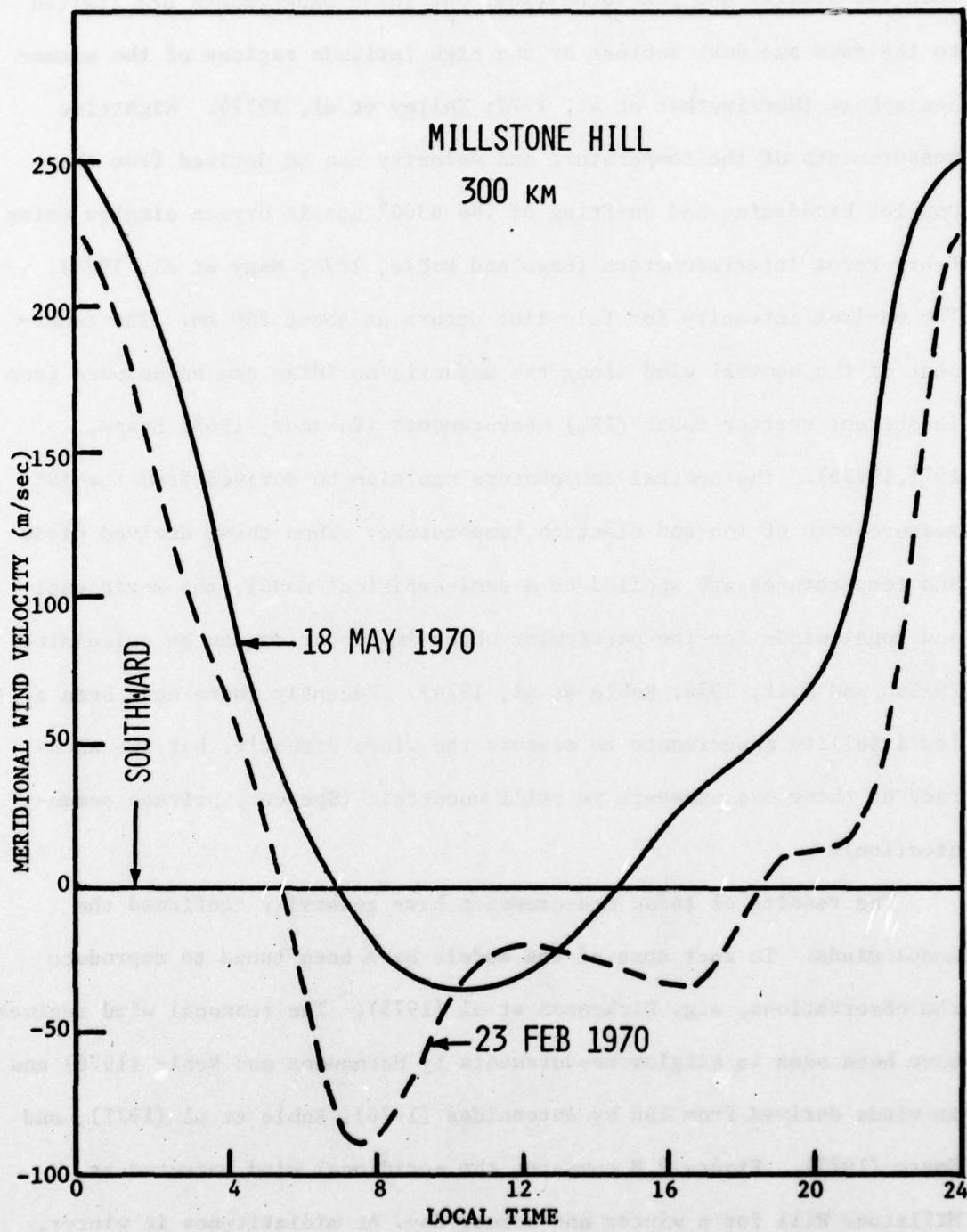
Figure 2.8 Comparison of the meridional component of the thermospheric wind observed over Millstone Hill on a summer and winter day in 1970.

hours   and sunrise, whereas the summer winds are predominantly south-
ward for most of the day except for a few hours near noon. This gives
rise to a diurnally averaged meridional flow which is nearly zero or
slightly poleward in winter and equatorward in summer. The diurnally
averaged zonal winds are normally westward in summer and eastward in
winter. The seasonal variation in the meridional winds is also seen in
the summer-winter difference in the diurnal h_mF2 and N_mF2 patterns. To
date, the largest data sample of thermospheric wind measurements has
been compiled by Emery (1977) from observations made at the Millstone
Hill ISR. The analysis included 39 days of data taken over a two year
period 1970-1971 near solar cycle maximum. The results clearly showed
the seasonal variation in the diurnally averaged winds. There was also
evidence of the modulating effect of geomagnetic activity. Hernandez
and Roble (1977) have presented a year of nighttime observations of
winds and temperatures made during solar minimum. Using a model for
daytime winds and adding the observed nighttime winds to obtain a diur-
nally averaged value, their results support the conclusions of the model
of Roble et al (1977) that the solstice circulation at solar minimum is
a large Hadley cell with no reverse cell in the high latitude winter
hemisphere.

Satellite composition measurements have confirmed the existence of
the oxygen anomaly and helium bulge. Figure 2.9 shows the measurements
made by OGO-6 (Hedin et al, 1972). The helium densities are obviously
out of phase with O, N_2, and temperature. The winter oxygen densities
are larger than would be expected from diffusive equilibrium considera-

41
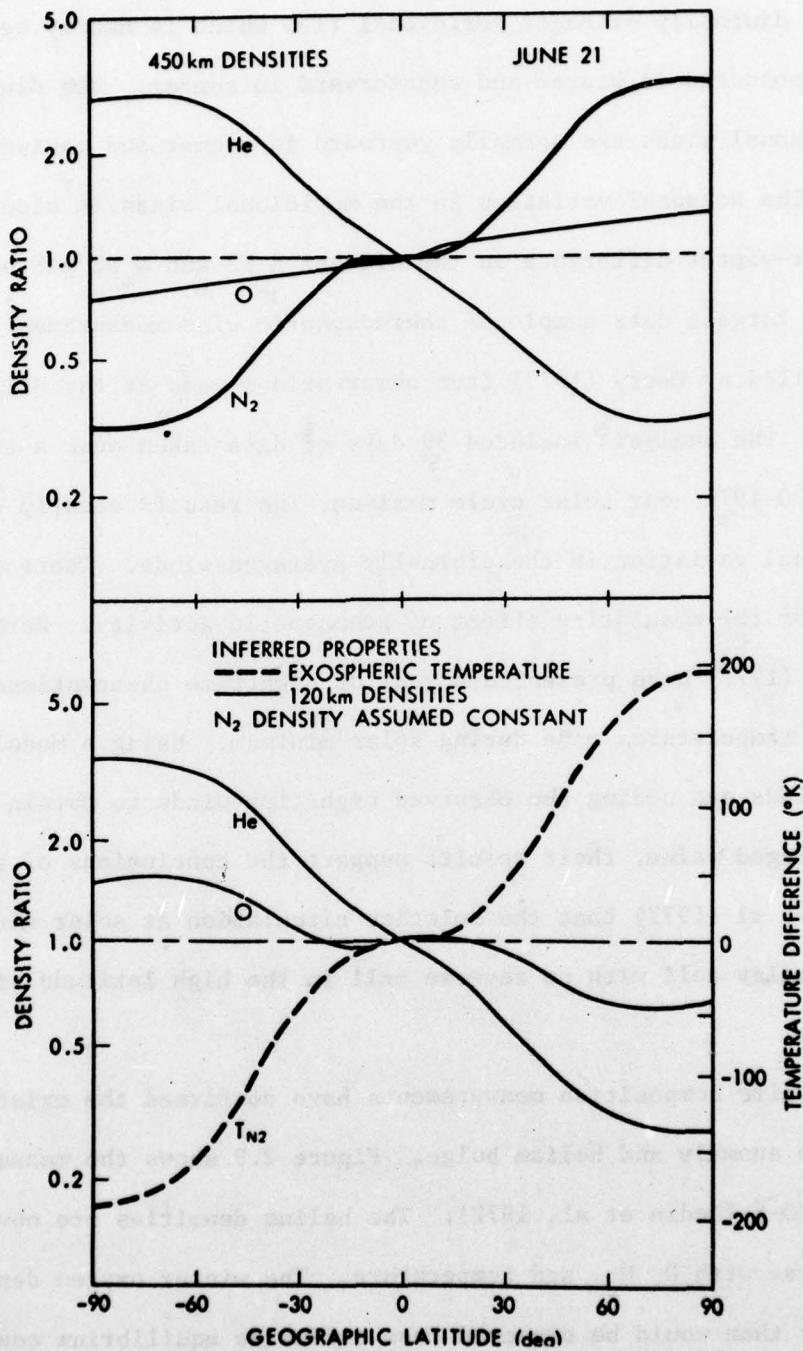
Figure 2.9 OGO-6 neutral density measurements – top – observed abundances relative to mean – bottom – abundances allowing for variation in T_∞.

tions using the measured temperature. Nisbet and Glenar (1977) used OGO-6 measurements of O and N_2 plus rocket release measurements at high latitudes to compute the divergence from the polar cap. They found a net divergence of O, indicative of mass flow and energy transport from the auroral regions, with the most pronounced effect in the post-midnight sector.

2.4 Geomagnetic Disturbances

2.4.1 Changes in the Ionosphere and Neutral Composition

During geomagnetic disturbances great amounts of energy are deposited in the thermosphere at high latitudes in the form of both Joule heating and particle precipitation. The particle precipitation not only adds energy through collisional heating of the ambient gases, but also increases the ion density through ionization. The increased ion densities, primarily on the nightside, combined with the increased convective electric fields, mean the Joule heating is greatly enhanced. These heat sources can locally exceed the EUV and UV heating which normally drives the circulation. Since the EUV heating varies only slowly with latitude, this high latitude energy deposition, which is confined to a relatively narrow latitudinal belt, can have effects on the circulation which can be quite large.

The earliest ideas on geomagnetic storm effects on the global circulation were derived from departures of the ionospheric h_mF2 and N_mF2 from their normal diurnal patterns. Increased high latitude heating will cause the meridional winds to become stronger equatorward and will

43

drive the ions up the field lines. Spurling and Jones (1976) have argued that most of the stormtime lifting of the F-region is due to winds. This lifting will be most pronounced during the nighttime, when the winds are already equatorward. Using ionosonde observations, Novikov (1976) has found the lifting to be largest in the post-midnight sector.

Although the thermospheric circulation probably plays the dominant role in determining the global nature of the ionospheric storm, electric field and plasmaspheric effects are still important. The large increases of h_mF2 and N_mF2 in the dusk sector on disturbed days are probably due to these effects (Evans, 1970). Analysis of whistlers by Park (1970, 1976,1977) and Park and Meng (1971) also suggest a plasmaspheric coupling. East-west electric fields they observed in the plasmasphere correlate with stormtime motions of h_mF2. At night, a global lifting of the h_mF2 and a decrease in N_mF2 in the 12 hour period after a substorm onset has been observed by Kane (1973); and Van Zandt et al (1971) observed a lifting in the post-midnight sector (normally a period of downward motion of the ionosphere during disturbed periods because of westward electric fields) coincident with the maximum in the H-component of the magnetic field after substorm onset. Both of these effects may be due to electric fields, perhaps of magnetospheric origin, penetrating into the plasmasphere down to low latitudes. Unfortunately, mid-latitude electric fields are generally below the threshold levels of present satellite instrumentation ($\approx$10 mv/m), even during disturbances, and other measurements, such as ISR and barium releases, are limited, so a precise understanding of the electric field and the resulting dynamical behavior of the ionosphere and thermosphere has yet to be obtained.

The ionospheric storm response to an auroral disturbance typically has two phases (Rishbeth and Garriot, 1969), which are primarily seen at mid-latitudes. In the positive phase there is a lifting of the h_mF2 and a daytime increase in N_mF2 and total electron content (TEC). This phase is more pronounced in the winter hemisphere. The negative phase of the ionospheric storm is a marked depression in N_mF2 (or f_oF2) and TEC values on the day following the storm onset and lasting 1-3 days (Figure 2.10). This effect is most evident in the summer hemisphere. It is generally agreed that changes in the circulation and in the composition are primarily responsible for the negative phase (Rishbeth, 1975). In the summer hemisphere, the increase in the auroral heating reinforces the equatorward winds, giving rise to increased transport of O to produce a net decrease in the O/N_2 ratio and a lower ion density. This factor more than compensates for the lifting of the ions by the equatorward winds to high altitudes where the recombination rate is low, so the seasonal and geomagnetic storm transport of O reinforce each other. In the winter hemisphere, the ion density is already large due to the winter oxygen anomaly, and auroral heating is either less intense or confined to a smaller area, so that global changes are less pronounced (Prolss, 1977).

Models of the thermospheric response to increases in auroral heating have been developed by Mayr and Volland (1973) and Mayr and Hedin (1977) and have produced composition changes which are compatible with those inferred from the ionospheric behavior. In addition, there have been several published reports of in situ observations of composition changes associated with geomagnetic disturbances (Jacchia et al, 1977; Marcos et

45
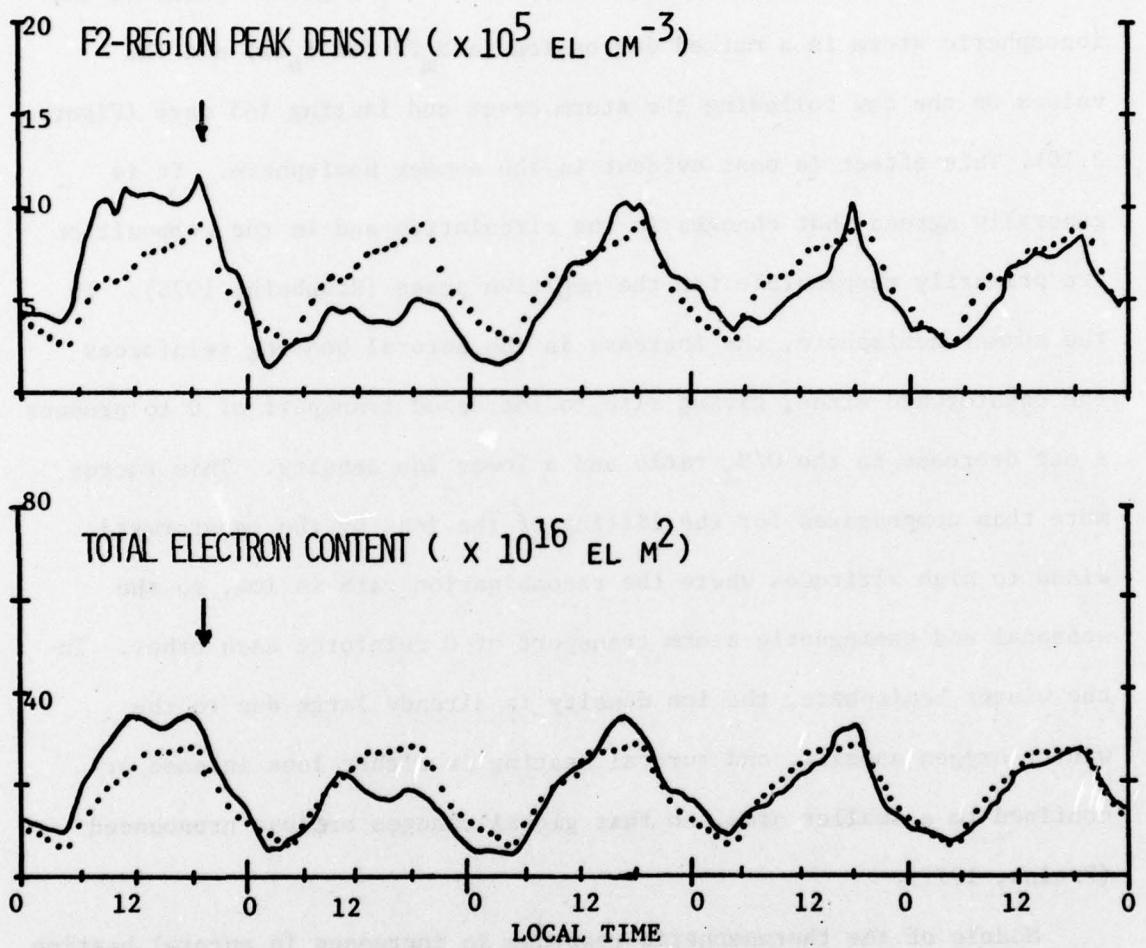
Figure 2.10 Effects of the positive and negative phases of an ionospheric storm reflected in the Wallops Island f$_o$F2 and the Hamilton, MA, total electron content. There is a large increase in both values above the monthly average (dots) on the day the storm begins, while the values are considerably depressed on the day after the storm onset.

46

al, 1977; Trinks et al, 1977; Nisbet et al, 1977; Chandra and Spencer, 1976; Trinks et al, 1976; and Raitt et al; 1975). These observations generally show increased N_2 densities, coincident with the local time sectors of maximum Joule heating, depletion of O and He at the poles and a decrease, or at least no change, in O and He densities at mid-latitudes. The net effect is a decrease in the O/N_2 ratio at mid-latitudes and an increase in O and He at equatorial latitudes.

The present discussion has dealt with the global scale ionospheric storm. Isolated auroral substorms often have only geographically local-ized effects. Park and Meng (1976) have examined four isolated sub-storms and found that only the longitudinal belt which was in the noon sector during the substorm showed ionospheric substorm effects. They suggest that the heating near the cusp region may provide the important dynamic forcing during the substorms, even though the more obvious substorm effects are seen in the nighttime auroral region. There do appear to be "storm centers" and "magic hours" which show larger effects than the global response and are dependent on geographic location and onset time of the storm (Rishbeth, 1975).

Chandra and Spencer (1976), Prolss (1977), and Prolss and von Zahn (1977) have compared both ionospheric measurements of h_mF2 and N_mF2 and satellite composition data: They found the disturbance boundary extends to lower latitudes in the summer hemisphere while the effects are con-fined to high latitudes in the winter hemisphere (Figure 2.11). The disturbance in the winter hemisphere has a sharp boundary, even though the variation in the O/N_2 ratio can be quite large. The disturbance

47
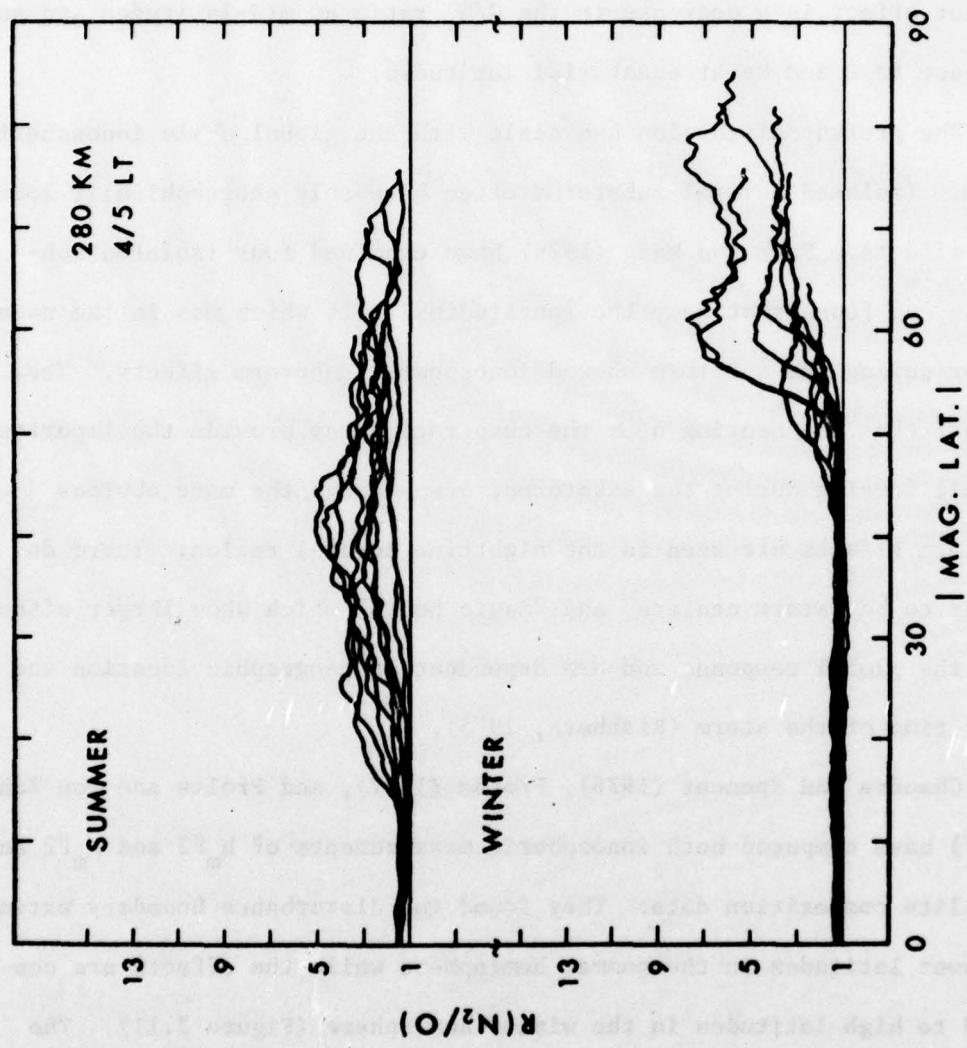
Figure 2.11 Geomagnetic disturbance effects on observed N_2/O ratio for summer and winter hemispheres. (Prolss and von Zahn, 1977).

boundary in the summer hemisphere has a gradual slope. These observations are consistent with the positive-negative phases of the ionospheric storm and are quite compatible with the summer-winter circulation pattern which is observed and predicted by the models (Figure 2.5).

2.4.2 Changes in the Neutral Circulation

The most striking observation of stormtime neutral winds is a surge in the equatorward wind near local midnight. A few observations of this phenomena have been reported by a number of investigators using different techniques: Barium/Strontium releases near 67° N (~ 225 km) for two active days (Kelley et al, 1977); FabryPerot interferometer measurements of $6300\overset{\circ}{A}$ airglow (~ 250 km) at Fritz Peak for four disturbed days (Hernandez and Roble, 1976); and also reported by Hays and Roble (1973) and W. A. Biondi (private communication); using the Chatanika ISR Bates (1977) and Bates and Roberts (1977) observed a southward midnight surge coincident with the passage of the Harang discontinuity overhead, the strength of the surge dependent on K_p.

Another significant stormtime effect is an observed westward and southward wind in the dusk sector reported by Hernandez and Roble (1976b). This coincides with the large westward ion drifts observed by Evans (1972), with the ion drag apparently reversing the normally eastward winds, and is most likely an electric field effect.

There are no published observations of dayside neutral winds during disturbed periods and the effect the disturbance might have is unclear.

49

2.5   Gravity Waves

The primary focus of this research is the effects of changes in solar and geomagnetic activity on the global scale thermospheric circulation. However, another important aspect of the effects geomagnetic activity has on the thermosphere is the large scale gravity waves which are launched from the auroral zone by substorms (Francis, 1975). The effects of these waves on the mid-latitude ionosphere as they travel equatorward have been observed for many years and are known as traveling ionospheric disturbances (TIDs). Francis (1975) has presented a review of gravity wave theories and observations. No attempt will be made to analyze in detail the gravity wave effects, although the evidence of their effects on the derived neutral winds and temperatures will be presented and compared to other changes in the large scale circulation.

Large scale TIDs typically have horizontal speeds of 400 to 1000 m/sec, periods of 30 minutes to 3 hours, and wavelengths of 1000 km. Rather than a wave train, it appears that the TID is a single wave pulse. Theoretical models used by Testud et al (1975) and Richmond and Matsushita (1975) which include dissipative effects, produce results compatible with ISR observations, both of which support the single pulse theory. Richmond (1978) has found that either thermal forcing (Joule heating) or momentum forcing (Lorentz force) can provide sufficient energy to produce the wave, although Joule heating is probably more important for larger events. There is ample evidence (e.g. Testud et al, 1975; Roble et al, 1978) which relates each TID to a particular substorm onset, implying that the apparent wave trains with periods of

50

1 - 3 hours observed by early investigators are merely series of single pulses initiated by individual substorms, which typically recur at 1 - 3 hour intervals during very active periods.

The signature of the TID in ionosonde and TEC measurements is a wavelike lifting and falling of h_mF2 and an increase in f_oF2 and TEC. ISR observations also detect an increase in ion temperature and the upward ion drifts coincident with the lifting of the h_mF2. This latter effect is related to the equatorward pulse in the winds which drives the ions up the field lines.

The exact source of the waves is unclear. Davis and DaRosa (1969) extrapolated the path of TIDs measured at mid-latitudes and found the direction and speed of the waves consistent with a source at 1900 geomagnetic time and a 78° N latitude. Testud et al (1975) found that gravity wave effects they observed during the day were probably from a source on the day side, most likely the cusp region. They concluded that gravity waves are generated in the same auroral sector in which the TID is observed.

3. OBSERVATIONAL TECHNIQUES

3.1 Incoherent Scatter Radar Experiment

A detailed discussion of the theory of Thomson, or incoherent, scatter radar (ISR) and its application to the study of the earth's ionosphere can be found in reviews by Evans (1969,1974). This section will give a brief description of the basic theory and the basic data which can be obtained.

J. J. Thomson, the "discoverer" of the electron, observed that electrons can scatter X-rays. In general, the theory of electron scattering applies to all electromagnetic radiation. The radar cross-section of a free electron is given by

$$\sigma_e = 4\pi \ r_e^2 \sin^2 \Psi \qquad (3.1)$$

where r_e is the classical electron radius and Ψ is the angle between the direction of the incident electric field and the direction to the observer. For backscatter, $\Psi = \pi/2$. In the ionosphere, the random thermal motion of the electrons will result in the scattered signals having phases which vary with time and are not related to each other, suggesting the name incoherent.

If the electrons alone are considered, the spectrum of the scattered signals should have a Gaussian distribution with a half-power width which depends on the Doppler shift of an electron with the mean thermal speed of the observed electrons,

$$\Delta f_e = (8kT_e/m_e)^{1/2}/ \lambda \quad \text{Hz} \qquad (3.2)$$

where k is Boltzman's constant, T_e is the electron temperature, m_e is the mass of an electron, and λ is the wavelength of the incident radiation.

Using a high-powered UHF radar, Bowles (1958) found that the observed Doppler broadening was much less than predicted using just the electron temperature. He suggested that the effect of the ions must be taken into consideration.

As shown by Fejer (1960), the ions are capable of creating electron density fluctuations which have a larger scale than the electron Debye length, or shielding distance, D_e, given by

$$D_e = (\varepsilon_o kT_e/4\pi \quad Ne^2)^{1/2} \quad \text{meters} \qquad (3.3)$$

where ε_o is the permitivity of free space, N is the electron density, and e is the charge of an electron. For incident radiation with a wavelength greater than the Debye length, the interaction of the ions with the electrons in the form of ion-acoustic waves will modify the nature of the scattered signal. The electron Debye length in the ionosphere ranges from less than 1 cm in the E-region to about 4 cm at 1000 km. The wavelength of the probing signal at the Millstone Hill ISR is 68 cm. At such long wavelengths, $\lambda >> D_e$, so the echo from the pure electron scattering is a relatively weak, narrow line (plasma line) displaced from the radar center frequency by $\pm f_N$, where f_N is the plasma frequency

53

$$f_N = (Ne^2/m_e\epsilon_o)^{1/2}/2\pi \quad \text{Hz} \tag{3.4}$$

Most of the scattered signal power is in the ionic component which has a Doppler broadened spectrum given by

$$\Delta f = \pm\Delta f_i(T_e/T_i)^{1/2} \quad \text{Hz} \tag{3.5}$$

where

$$\Delta f_i = (8kT_i/m_i)^{1/2}/\lambda \quad \text{Hz} \tag{3.6}$$

with T_i and m_i the ion temperature and mass, respectively. In effect, the scattering is from particles with the temperature and scattering cross section of the electrons but the mass of the ions. The power spectrum of the scattered signal is bimodal (Figure 3.1), with two maxima, or wings, produced by the waves approaching and receding from the receiver. The actual shape of the spectrum will depend on the ratio of T_e/T_i. Figure 3.2 shows an example of how the spectrum varies with T_e/T_i. (The ratio D_e/λ also effects the shape of the spectrum and must be kept separate from the T_e/T_i ratio effect.)

Above about 200 km the dominant ion is O^+. Below 200 km, the presence of molecular ions, NO^+ and O_2^+, complicates the data reduction, since m_i now becomes unknown. For the data used in this research, the measurements were all above 200 km and this was not a problem.

Besides Doppler broadening, the spectrum will also be Doppler shifted due to any bulk motion of the ions. For a mean ion drift, $\bar{v}_i$,

54
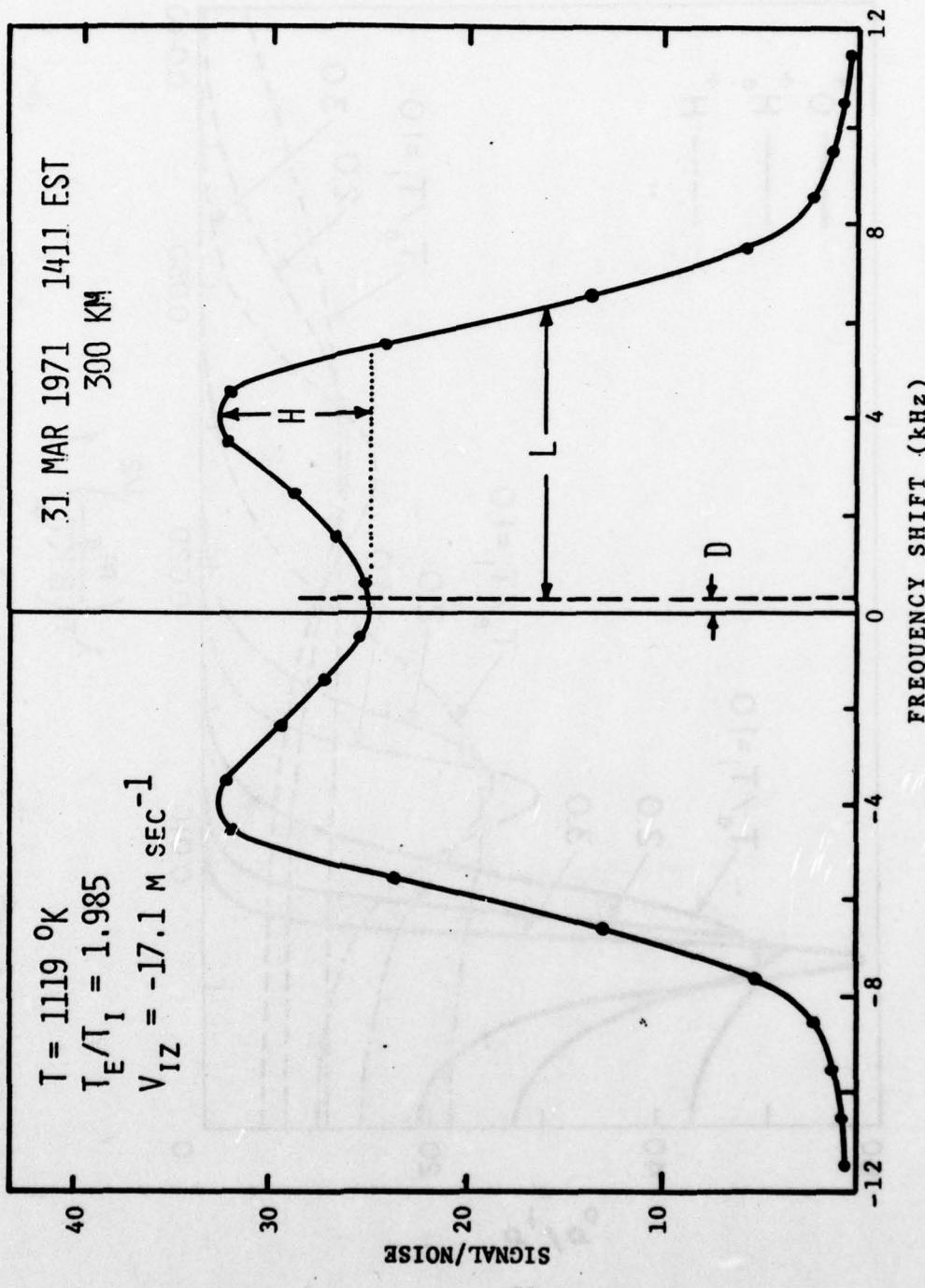
Figure 3.1 Example of incoherent scatter spectrum measured by UHF radar at Millstone Hill. (From Salah, 1972).

55
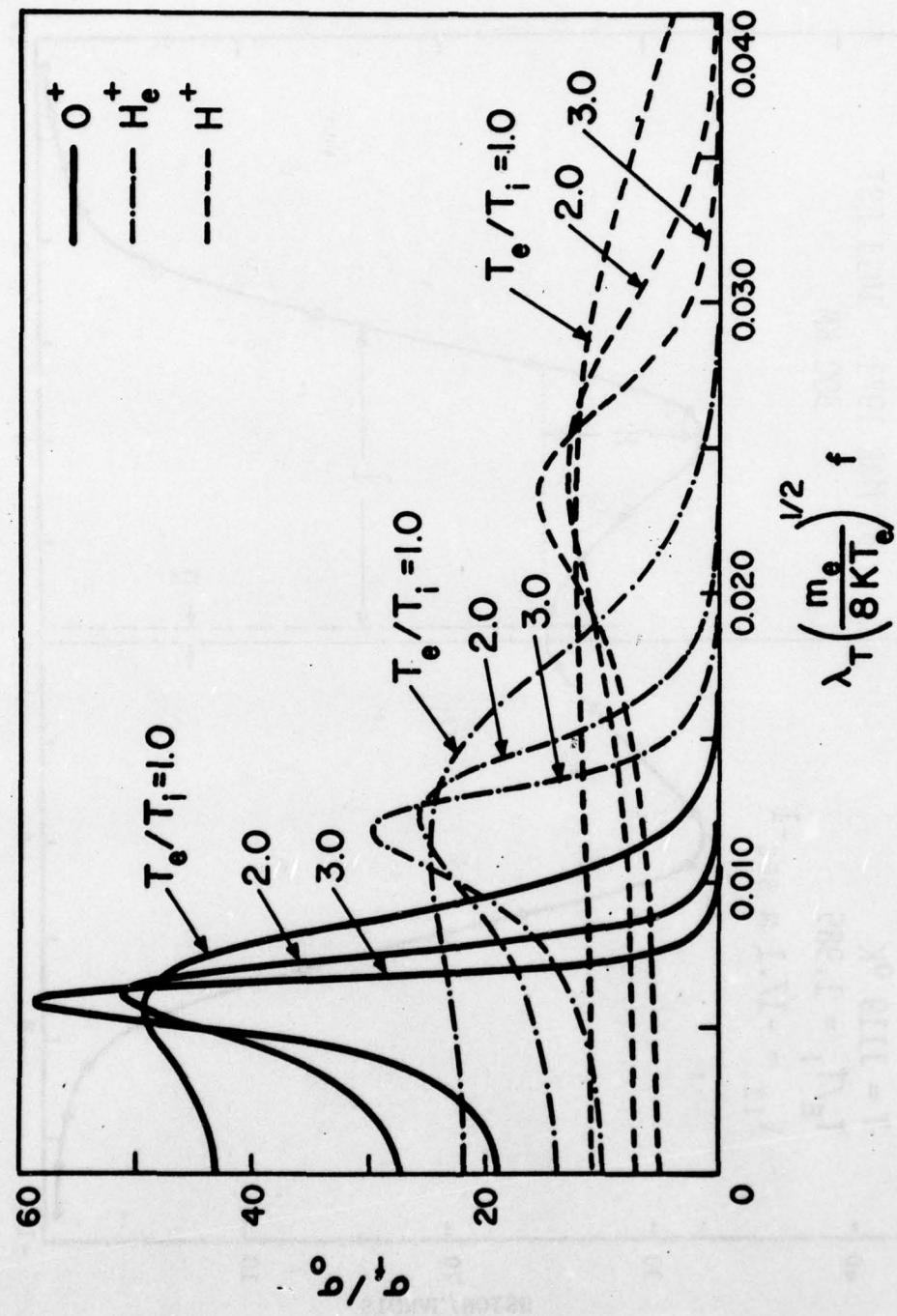
Figure 3.2 Theoretical power spectra for different values of T_e/T_i and for different ions.

the frequency shift is given by

$$\Delta f_d = 2\bar{v}_i \cdot \hat{k}/\lambda \quad \text{Hz} \tag{3.7}$$

where $\hat{k}$ is the unit vector along the direction of the incident radiation.

The total power, P_s, of the scattered signal at some height, h, seen at the receiver is related to the electron density by

$$P_s = \text{constant} \cdot N\sigma/h^2 \tag{3.8}$$

where the constant depends on the characteristics of the radar and σ is the total cross-section attributable to the ionic component

$$\sigma = \frac{\sigma_e}{(1 + \alpha^2)(1 + T_e/T_i + \alpha^2)} \tag{3.9}$$

in which
$$\alpha = 4\pi D_e/\lambda \tag{3.10}$$

The basic data which can be deduced using the ISR technique are thus profiles in height of electron density, electron and ion temperature and ion drift.

3.2 Millstone Hill ISR Measurements

3.2.1 "One-Pulse" Experiments

The pulse-length of the transmitted signal, the sampling time of the received signal, and the number of pulses transmitted can all be varied depending on the parameters and altitudes which are being examined. The data used in this research were taken using the various "one-pulse"

57

modes, in which a single pulse is transmitted, and the received signal is gated in order to obtain profiles of each parameter versus height. The "A" mode uses a 0.1 msec pulse, giving a height resolution of 15 km. This mode covers an altitude range from 150 to 900 km and is primarily used to obtain profiles of N. The "B" mode uses a 0.5 msec pulse giving a height resolution of 75 km. The B mode altitude range is 225 to 675 km. The "C" mode uses a 1.0 msec pulse providing a height resolution of 150 km and covering an altitude range of 450 to 1125 km. The B and C modes are primarily used for obtaining profiles of T_e, T_i, and, since the antenna is pointed vertically, the vertical ion drift, V_{iz}. A typical "observation" consists of a sequence of modes, ABC, with each mode lasting 8 minutes. In order to improve the statistical reliability of the high altitude drift measurements, an ABCC sequence has sometimes been run, with the A and B modes lasting only 4 minutes. The time resolution of each of these sequences is about 30 minutes. Table 3.1 gives a summary of the characteristics of each mode.

Table 3.1

Characteristics of the Data Modes of the Millstone Hill UHF Single-Pulse Experiment

	MODE		
	A	B	C
Pulse length (msec)	0.1	0.5	1.0
Height resolution (km)	15	75	150
Sample spacing (km)	7.5	75	75
Altitude coverage (km)	150-900	225-675	450-1125
Output	N	T_e,T_i,V_{iz}	T_e,T_i,V_{iz}

58

Rather than trying to determine the absolute sensitivity of the radar receiver, the A mode is used just to obtain the vertical profile of the relative power·received, from which a density profile can be computed. A nearby ionosonde is used to obtain the critical plasma frequency ($f_oF2 = f_{Nmax}$) of the ionoosphere. Using equation 3.3, N_mF2 can be computed and this value is used to normalize the density profile. (Since the ratio T_e/T_i appears in σ, the derivation of N directly from the A mode alone could not be done unambiguously even if the absolute sensitivity of the radar were known.)

For the B and C modes the received signal is applied to a system of filter banks matched to the transmitted signal to obtain a measure of the received power versus frequency. A curve is fitted to the measured values to obtain the spectrum. The various characteristics of the spectrum, shown in Figure 3.1, which are used to deduce T_e, T_i, and V_{iz} are the half-power width, L, the ratio of the power in the wings to the power in the center frequency, H, and the Doppler shift, D, where

$$L = 0.71 \ \Delta f \qquad (3.11)$$

$$D = \ \Delta f_d = 2V_{iz}/\lambda \qquad (3.12)$$

The shape of the spectrum depends on the ratio T_e/T_i, so that H and L can be used to obtain this ratio. In practice, D is two orders of magnitude smaller than L, so precise measurements of the spectrum are required to obtain reliable values of V_{iz}.

Prior to January 1976, all one-pulse measurements use the matched filter banks to determine the shape of the spectrum. Any equipment problem involving the matching of the filters to the transmitted signal

59

could result in an error. Both Salah (1972) and Emery (1977) found a systematic difference between the temperature measured by the B and C modes in the altitude range in which they overlap. Apparently, the mismatching problem caused the difference, with the B mode having the greatest error. Emery (1977) developed an empirical correction scheme using data from 1970 through 1972. This correction has been applied to all the one-pulse B mode temperature data taken through 10 January 1976. After this date, a new data-taking procedure eliminated the problem.

3.2.2 Auto-correlation Technique

In order for the Millstone Hill Radar Facility to fulfill its role in the data taking phase of the International Magnetospheric Study, an effort was made to enhance the capability of the radar. One part of this improvement program was the design and construction of a hardware correlator signal processor that would greatly upgrade the data-gathering capabilities of the radar

As mentioned above, the use of a bank of matched filters to measure the power spectra has inherent equipment problems which may effect the derived data. One alternative method described by Farley (1969) is to construct the auto-correlation function (ACF) of the power spectrum using a hybrid one-bit x multibit product of the digitized received signal measured at several equispaced lag times within the period of the one transmitted pulse. The output from the correlator contains the real and imaginary parts of the correlation function for each lag time. These are stored for later analysis by the on-line computer. Figure 3.3 gives an example of the real and imaginary parts of the correlation

60

functions measured at one altitude. The basic shape of the power spec-
trum determines the real part of the ACF, while the imaginary part
reflects any   Doppler shift of the received signal caused by
the ion drift. By fitting a theoretical ACF to the experimental values
and doing a reverse Fourier transform, the power spectrum can be obtained
and the values of N, T_e, T_i, and V_{iz} can be deduced.

As in the pre-1976 experiments, a series of different modes is used
for each "observation." Table 3.2 gives a summary of the characteris-
tics of each mode. The E mode essentially replaces the A mode for
making high resolution profiles of reflected power versus height. The L
mode is added to the B and C modes for ACF measurements. The locally
measured $f_o F2$ is used to normalize the power profiles to obtain the
density profiles.

Table 3.2

Characteristics of the Data Modes of the Millstone
Hill UHF Single-Pulse Auto-Correlation Experiment

Mode	Pulse Length (msec)	Height Resolution (km)	Sample Spacing (km)	Altitude Coverage (km)	Spacing of Points (msec)	Output
L	0.2	22.5	22.5	179–584	0.01	N,T_e,T_i,V_{iz}
B	0.5	75	75	219–1044	0.01	N,T_e,T_i,V_{iz}
C	1.0	150	75	331–1531	0.01	N,T_e,T_i,V_{iz}
E	0.1	15	6,9,15	91–551	----	N

3.2.3 Data Reduction

After the ionospheric values have been deduced from the measured

61
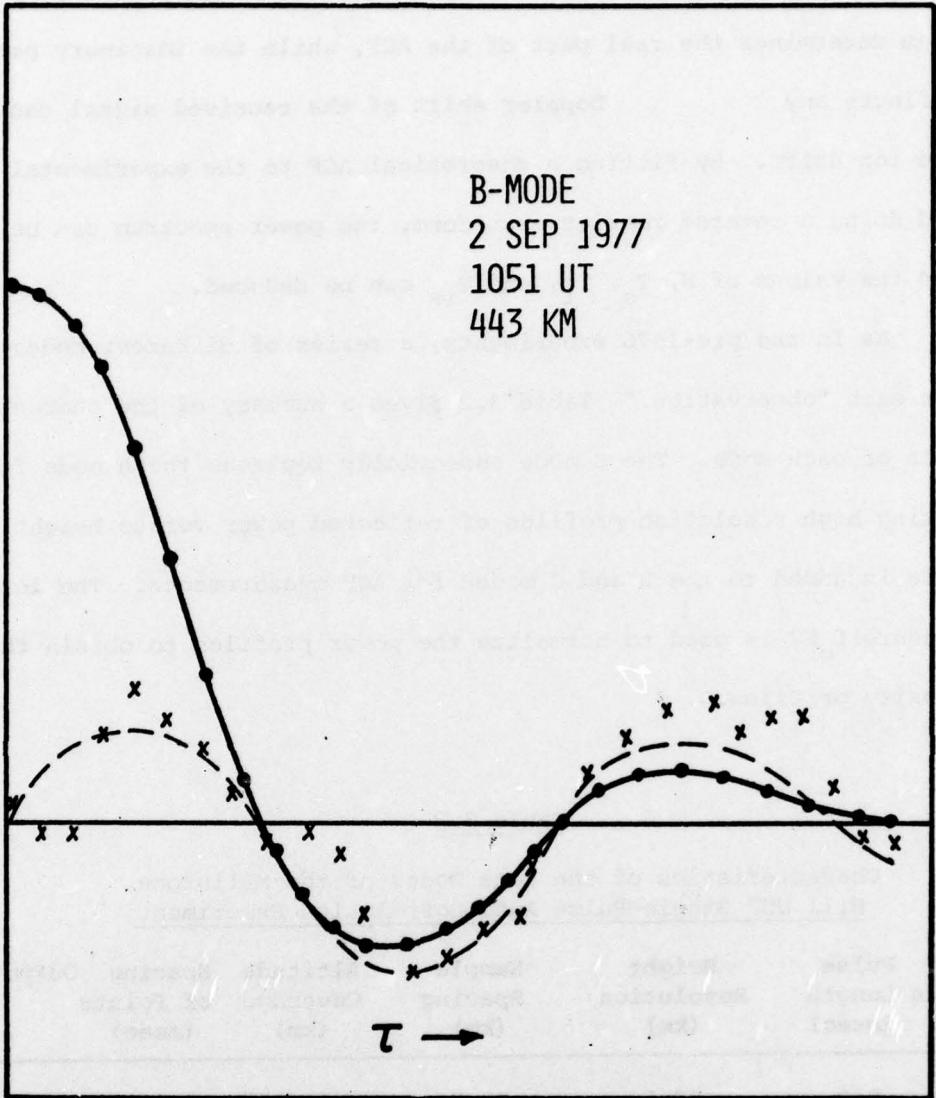
Figure 3.3 An example of the computed real (dots) and imaginary (crosses) correlation functions plotted against the lag-time, τ. The solid and dashed lines are the autocorrelation functions which have been fitted to the data.

spectra, which is done using computer analysis programs, the data must be edited by hand to remove extraneous measurements caused by interference or equipment problems. The data are then smoothed with respect to height and time by a program developed at Millstone by J. M. Holt (Evans and Holt, 1976). The program finds the best fit of a two-dimensional polynomial series to the data points in a least-squares sense. The order of the polynomial depends on the number of observations in time and height. Once the polynomial coefficients are known, any of the observed parameters and its derivatives can be obtained for any time and height within the total observing period (normally 24 to 36 hours). Figure 3.4 is a sample computer plot of the density contours which were derived from the polynomial fit.

3.3 Electric Field Measurements in the F Region

Electric fields in the ionosphere will induce E x B drifts perpendicular to the magnetic field lines. Since the magnetic field has a declination of 72° at Millstone, one contributor to the ion drifts measured by the vertical pointing radar will be electric fields. Attempts have been made to employ the fully steerable L-band radar at Millstone to make ion drift measurements at an elevation of 45° in the magnetic north and magnetic west directions. When combined with the vertical measurements, the magnetic east-west and north-south components of the electric field can be derived. Since each of the three measured components are in three physically different volumes of the ionosphere, the latitudinal and longitudinal differences in the volumes must be taken into account. For the northward measurement, it is assumed that

63
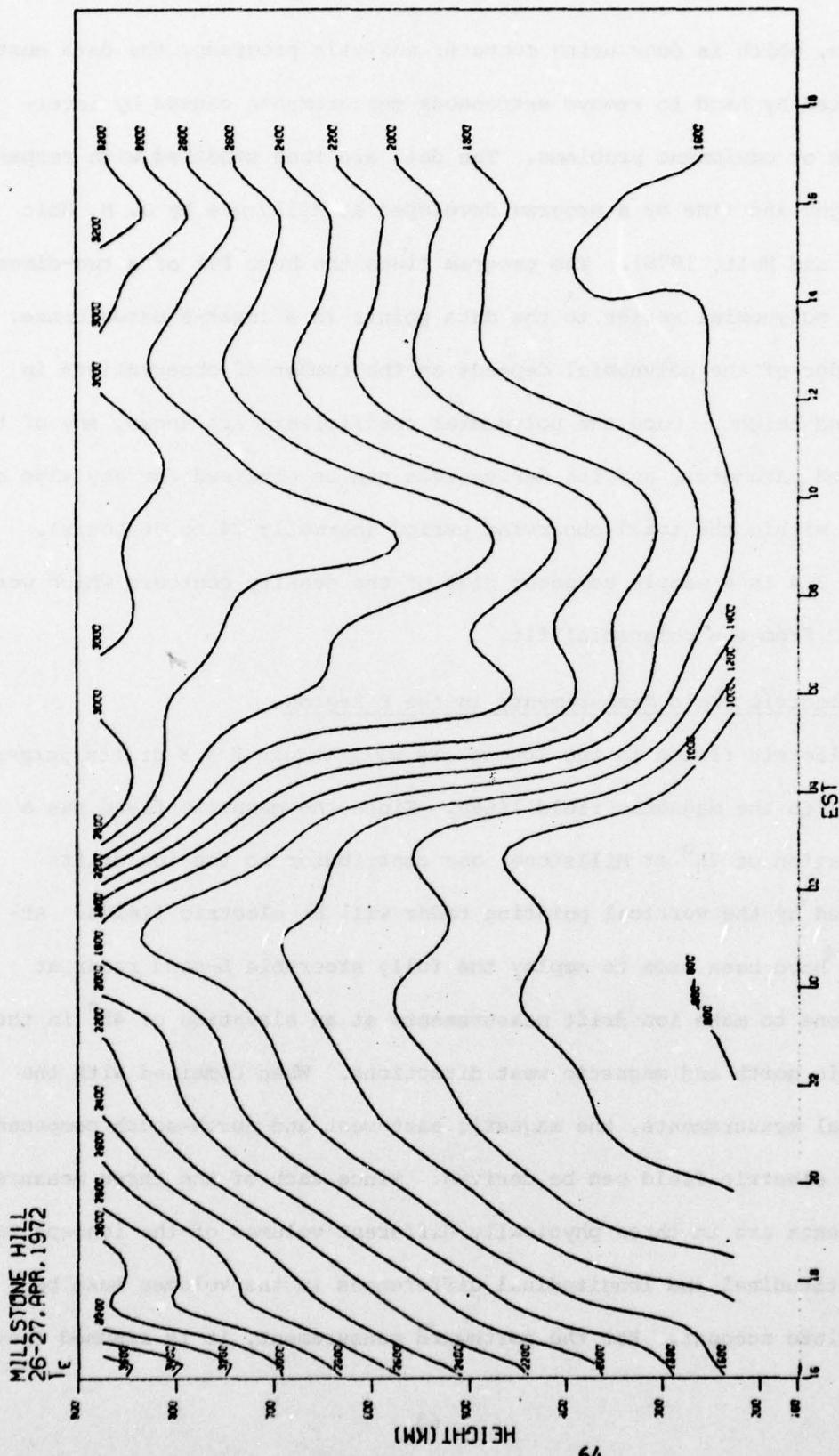
Figure 3.4 Example of the computer plotted contour profiles of ionospheric data constructed from a polynomial fit to the data.

there is no latitudinal variation in the electric field between Mill-
stone (L = 3.2) and the measured volume (L = 3.7). Longitudinal dif-
ferences are assumed to be due to local time effects and are allowed for
by making a correction in the observing time.

The L-band radar has a much lower sensitivity than the UHF radar.
During local nightime when the ion densiity is low, the signal-to-noise
ratio is usually small so that nighttime drift measurements are usually
unreliable.

4. DERIVATION OF NEUTRAL PARAMETERS

Even though the F-region ion-neutral collision frequency is low enough that the ions can be assumed to be bound to the magnetic field lines, the coupling between the ions and neutrals is still strong enough that certain neutral properties can be deduced from the observed plasma characteristics. This chapter will discuss the theory of how these neutral paramenters are derived and how they are applied to a semi-empirical model to compute neutral winds. This discussion will present the application of this theory as developed and applied by Emery (1977). Improvements to these procedures will be presented in following chapters

4.1 Neutral Temperature

4.1.1 Vertical Structure

Taking into consideration the thermal economy of the lower thermosphere, including downward thermal conduction and solar EUV heating, Bates (1959) proposed a simple analytic model for the thermospheric neutral temperature structure,

$$T_n(z) = T_\infty - (T_\infty - T_{120})\exp(-s(z - 120)) \tag{4.1}$$

where $T_n(z)$ is the neutral temperature in $^\circ K$ at some height, z, in km, T_∞ is the exospheric temperature, T_{120} is the temperature at 120 km, and s is a shape parameter. Equation 4.1 reflects the dominance of thermal conduction in redistributing heat at high altitudes and causing the temperature of the atmosphere to become isothermal. While direct confirmation has been limited, this temperature profile has been generally accepted (Banks and Kockarts, 1973) and is applied in all the data analysis in this research.

66

4.1.2 Heat Balance Equation

Above 300 km the neutral gas has become so tenuous that heating due to solar EUV absorption becomes small. As the collision frequencies decrease with height, the coupling between the neutral, ion, and electron gases weakens and each gas develops its own vertical temperature profile governed increasingly by vertical conduction (or in the case of ionized constituents, by conduction along the magnetic field line). The ambient electron gas is heated by low energy photoelectrons (<2 ev) and heat conducted from the plasmasphere, so the temperature of the electrons is raised above that of the ions. The electrons interact with the ions through coulomb collisions, heating the ions and raising the ion gas temperature above the neutral temperature. The ions in turn are cooled by collisions with the neutral gas.

The derivation of the neutral temperature is based on balancing the heat given by the electrons to the ions to the heat given by the ions to the neutrals. Assuming a single ion species, the equation for the ion heating rate is

$$\frac{dT_i}{dt} + \frac{2}{3}T_i \nabla \cdot \overline{v}_i - \left(\frac{3}{2} n(0^+)k \right)^{-1} \nabla \cdot K_i \nabla T_i = \left(\frac{3}{2} n(0^+) \, k \right)^{-1}(P_i - L_i) \qquad (4.2)$$

where K_i is the ion thermal conductivity, and P_i and L_i are the ion energy production and loss rates, respectively. Scale analysis of the equation (Salah, 1972; Alcayde and Bauer, 1977) shows that the terms on the left-hand side of the equation are about two orders of magnitude smaller than the right-hand side in the region between 300 and 500 km. This leads to the rather simplistic first order balance

$$L_i = P_i \qquad (4.3)$$

67

The primary energy loss mechanisms are through elastic collisions with neutral molecules (N_2, O_2) and resonant charge exchange ($O^+ - O$). These loss rates have been determined by Banks (1966b) and are given by

$$L_i = 10^{-14} n(O^+)(.21 n(O)(T_i + T_n) + 6.6 n(N_2) +$$

$$5.8 n(O_2))(T_i - T_n) \quad eV/cm^3 sec \quad (4.4)$$

Interaction of O^+ with lighter atoms and heat transport via lighter ions has not been considered. The electrons interact more readily with H^+ and He^+ ions causing them to achieve higher temperatures than O^+. However, Banks (1967) has found this heat loss mechanism to be negligble. The effect of neglecting cooling due to resonant ion-neutral charge exchange between H and He is unclear. Alcayde and Bauer (1977) use the balance given in equation 4.3 to compute both T_∞ and $n(O)$. Using solar minimum conditions, when the concentration of H atoms at mid-thermospheric altitudes can reach a few per cent, they have made sample calculations which indicate that neglecting H and He might have a significant effect in computing $n(O)$. The effect on the calculated T_o, is not reported, although errors as large as 20% in $n(O)$ apparently only effect the derived temperature by a few per cent (Emery, 1977). In work reported here, the presence of H and He should be considered for the few days analyzed near solar minimum; even then the H densities would only be significant at night. Since the proper abundances of the lighter elements is not known reliably, and their presence effects only a small portion of the data, they have not been considered in this analysis.

The primary heat source for the O^+ ions is elastic collisions with the hotter electron gas. Collisions with energetic photoelectrons and

68

energy from exothermic chemical reactions are negligible sources. Another heat source is frictional heating due to the relative bulk motions of the ions and neutrals. Electric fields provide one source of such motions. At high latitudes, the large electric fields which drive the ion convective pattern produce large Joule heating rates which not only heat the ions, but are an important source of heat for the neutral atmosphere. Such large fields are not normally seen at mid-latitudes. The neutral wind flow through the ions is also a source of frictional heating. To date, there has been no attempt to include frictional heating routinely in calculating T_∞ from experimental observations. Plasmaspheric heat fluxes during geomagnetically disturbed periods may also be an important heat source, but owing to the great disparity between the ion and electron thermal conductivities, it is believed that the ions are not significantly heated directly by this source.

The heating rate of the ions by the ambient electrons is given by Banks (1966a) as

$$P_1 = 4.82 \times 10^{-7} \, N \, n(O^+) \, (T_e - T_i)/T_e^{3/2} \quad eV/cm^3 sec \quad (4.5)$$

When the expressions for P_i and L_i are substituted into equation 4.3, the result is an equation with two unknowns, T_∞ and $n(O)$. In the altitude region between 300 km and 500 km, $n(N_2)$ and $n(O_2)$ are an order of magnitude or more smaller than $n(O)$, so their variation with height and time is negligible. It can be assume that $n(O^+) = N$, where N, T_e, and T_i are known from observations. Data for T_e and T_i are available at the nominal heights of 300, 375, 450, and 525 km.

One technique for solving for T_∞ and $n(O)$ proposed by Bauer et al

69

(1970) is to use a regression analysis to find values of T_∞ and $n(O)$ which best satisfy the balance equation at the observed heights. This procedure utilizes the analytical expression for neutral temperature given in terms of T_∞ in equation 4.1 and assumes $n(O)$ is in diffusive equilibrium, i.e. a function of temperature. An alternative method is to obtain the value of $n(O)$ at each height from an empirical model and just solve for T_∞.

The method of solving for the two unknowns simultaneously does not usually give satisfactory results (Salah and Evans, 1973; Bauer and Alcayde, 1977; Emery, 1977). The ion temperature approaches the neutral temperature at night; the difference $(T_i - T_n)$ in equation 4.3 then becomes small and complicates the regression analysis. The derived nighttime densities are often unrealistic, making all such results suspect. Because of this problem, and also in order to maintain consistency with the analysis of Salah (1972) and Emery (1977), the derivation of T_∞ in this research used neutral densities obtained from the MSIS model, and only T_∞ was computed. Emery found that a 20% error in $n(O)$ only introduced a 2.5% variation in the derived T_∞. The experimental uncertainty in the derived value is also estimated to be 2.5%.

To be consistent with the previous work, this analysis assumes that $T_{120} = 355^\circ K$ and $s = 0.02 km^{-1}$. Salah (1972) found that variations in T_{120} of $\pm 100^\circ K$ and s of $\pm .005 km^{-1}$ only affected the derived temperature by 12%. The values of N, T_e, and T_i were obtained from the polynomial fits described in Chapter 3.

4.2 Neutral Winds

There are three effects which can cause ion motion. The resultant

70

ion velocity, $\overline{V}_i$, can be expressed as the sum of the components of these three effects.

$$\overline{V}_i = \overline{V}_{D//} + \overline{V}_{n//} + \overline{V}_{E\perp} \tag{4.6}$$

$V_{D//}$ is the ambipolar diffusion velocity and is parallel to the magnetic field line. $V_{n//}$ is attributable to the horizontal component of the neutral wind in the plane of the magnetic meridian which at F-region heights drives the ions up or down the field lines. $V_{E\perp}$ is the $\overline{E} \times \overline{B}$ electric field drift and is perpendicular to the magnetic field line. Figure 4.1 gives a schematic depiction of how the various components combine to give the resultant ion velocity.

Following the convention of Salah and Holt (1974), $\overline{V}_{n//}$ is defined as positive upwards. The magnitude of $\overline{V}_{n//}$ is given by

$$V_{n//} = - \overline{V}_n \cdot \overline{B}/B = - u \sin D \cos I - v \cos D \cos I + w \sin I$$

$$\simeq - (u \sin D + v \cos D) \cos I = - V_{Hn} \cos I \tag{4.7}$$

where $\overline{V}_n$ is the neutral wind with the zonal (u), meridional (v), and vertical (w) components positive in the eastwards, northwards, and upwards directions, respectively. V_{Hn} is the horizontal component of the neutral wind along the magnetic meridian. The values D and I are the magnetic declination and inclination, which for Millstone Hill are -14° and 72°, respectively.

Equation 4.7 is an approximation based upon the assumption that the vertical velocity w << u,v. Dickinson and Geisler (1968) have shown that this is generally true at mid-thermospheric heights.

When the geometry for the Millstone Hill Observatory is taken into

71
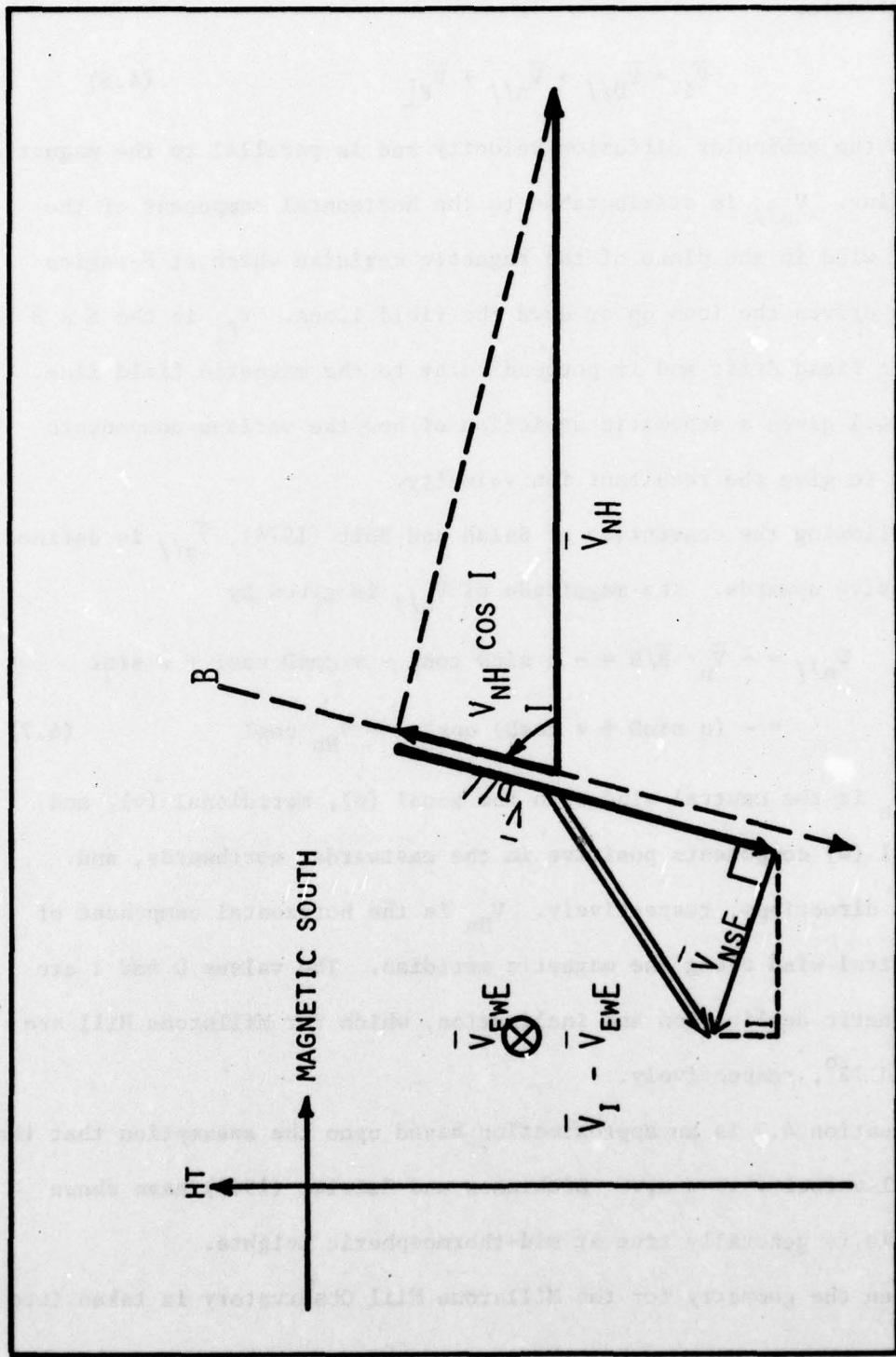
Figure 4.1 Schematic of the components of the ion drift in the plane of the magnetic meridian. (From Emery, 1977).

account, including the fact that the radar is actually looking 2° south of vertical, the horizontal wind can be approximated as

$$V_{Hn} = \frac{V_{D//}}{\cos I} - (V_{iz} - V_{nsE}(\cos I \cos 2^o - \sin I \cos D \sin 2^o) +$$

$$V_{ewE} \sin D \sin 2^o)/\cos I(\sin I \cos 2^o + \cos I \cos D \sin 2^o) \quad (4.8)$$

where V_{nsE} and V_{ewE} are the magnitudes of the velocities given by

$$\overline{V}_{E\perp} = \frac{\overline{E} \times \overline{B}}{B^2} = \overline{V}_{ewE} + \overline{V}_{nsE} \quad (4.9)$$

The vertical ion drift, V_{iz}, is observed, so that a measure of the neutral wind can be deduced if the ambipolar diffusion velocity and the $\overline{E} \times \overline{B}$ drifts are known.

4.2.1 Ambipolar Diffusion Velocity

The ambipolar diffusion velocity of the plasma arises in response to gravity and vertical gradients in the plasma density and temperature. Neglecting viscosity and non-linear terms and assuming no currents, Schunk and Walker (1970) have derived the diffusion velocity from the equations of motion for the ion and electron gases. The diffusion velocity along the field line is given by

$$V_{D//} = - D_a \sin I \left[\frac{\partial \ln N}{\partial z} + \frac{\partial \ln T_p}{\partial z} + .38 \frac{\partial \ln(T_i + T_n)}{\partial z} + \frac{m_i g}{k T_p} \right] \quad (4.10)$$

where T_p is the plasma temperature, $(T_e + T_i)$, and D_a is the ambipolar diffusion coefficient (Stubbe, 1968)

$$D_a = \frac{k(T_e + T_i)}{\sum\limits_n \nu_{in} \mu_{in}} \quad (4.11)$$

73

where $\mu_{in} = m_i m_n/(m_i + m_n)$ is the reduced mass of the ions and neutrals and ν_{in} is the ion-neutral collision frequency. In computing D_a, neutral densities were taken from the MSIS model (Hedin et al, 1977a,b). Values of N, T_e, and T_i and their gradients were taken from the polynomial fits to the data (Evans and Holt, 1976). The collision frequencies were taken from Banks (1966b).

Salah and Holt (1974) estimated the accuracy of $V_{D//}$ to be 1-3 m/sec. This is well within the experimental uncertainty of V_{iz}, which is about 5-10 m/sec (Evans et al, 1970). However, this estimate does not include any error due to the uncertainty in the neutral densities used to compute D_a, where the uncertainty in n(O) is the primary contributor. Unlike the derivation of T_∞, where large uncertainties in n(O) have only a small effect, any uncertainty in n(O) will be applied directly to the uncertainty in $V_{D//}$. The division by cos I in the computation of V_{Hn} (equation 4.8) will further amplify this uncertainty. The procedure used in obtaining the neutral density, particularly n(O), can significantly affect the results. This problem will be discussed in the next chapter.

4.2.2 Electric Fields

The contribution of electric field drifts to equation 4.8 is the greatest source of uncertainty in the determination of neutral winds from the data available from Millstone Hill. Measurements of mid-latitude electric fields in the F-region show great day-to-day variability and are seen to change with increased geomagnetic activity (Wand, 1978; Blanc et al, 1977; Kirchhoff and Carpenter, 1976). Emery (1977) used a

74

model electric field of Kirchhoff and Carpenter (1975) constructed from
measurements made at Millstone Hill to test the effect of including
electric fields and found the largest effect was at night with a decrease
in V_{Hn} of 20-50 m/sec. The nighttime measurements of the electric field
have the greatest experimental uncertainty and are the part of the daily
pattern most affected by geomagnetic disturbances. Because of all these
uncertainties, to date, the E x B drifts have been generally neglected
in models (e.g. Dickinson et al, 1975) and in data analysis (Emery,
1978; Salah and Holt, 1974; Salah, 1972).

4.3 Thermospheric Neutral Winds - The Emery-Millstone Hill Model

The single horizontal component of the neutral wind deduced directly
from the experimental observations has been used by several investigators
to confirm the basic results of the semi-empirical neutral atmosphere
models and to see if there are features of the winds, which the models
do not predict (Salah and Holt, 1974; Amayenc and Vasseur, 1972; Evans,
1971; Vasseur, 1969). Methods developed by Roble et al (1974) and
Antonaidas (1976) permit the exploitation of the incoherent scatter data
for the calculation of both the zonal and meridional winds. The neutral
winds reported here were computed using a model developed by Emery
(1977) based on these methods.

The Emery-Millstone Hill (EMH) method entails establishing a local
three-dimensional model of the neutral thermosphere and solving the
horizontal equations of motion to determine the zonal and meridional
winds. The primary inputs used to define the thermospheric model are
the exospheric temperature and the neutral wind, V_{Hn}, derived from the

75

observed ionospheric measurements. The method requires that the momentum equations be integrated between 120 and 600 km over a 24 hour period. It is assumed that the observatory is rotating under a fixed thermospheric pattern, so that the derivatives in local time and longitude are interchangeable.

4.3.1 The Momentum Equations

The horizontal equations of motion can be written as (assuming $w \ll u,v$)

$$\frac{\partial u}{\partial t} + u\frac{\partial u}{\partial x} + v\frac{\partial u}{\partial y} - \frac{uv \tan\phi}{r} = -\frac{1}{\rho}\frac{\partial p}{\partial x} + fv + F_x \qquad (4.12)$$

$$\frac{\partial v}{\partial t} + u\frac{\partial v}{\partial x} + v\frac{\partial v}{\partial y} + \frac{u^2\tan\phi}{r} = -\frac{1}{\rho}\frac{\partial p}{\partial y} - fu + F_y \qquad (4.13)$$

where x, y, and z are positive in the eastward, northward, and upward directions, $f = 2\Omega\sin\phi$ is the Coriolis parameter, Ω is the Earth's angular rotation velocity, r is the distance from the center of the Earth, p and ρ are the pressure and density, respectively, and F_x and F_y are the frictional forces. The curvature terms, which are normally not included in tropospheric analysis, cannot be neglected because of the large velocities (300-400m/sec) which occur in the thermosphere. The frictional forces which are important in the F-region are molecular viscosity and ion drag. These forces can be expressed as

$$F_x = \frac{1}{\rho}\left(\mu\nabla^2 u + 2\frac{\partial\mu}{\partial x}\frac{\partial u}{\partial x} + \frac{\partial\mu}{\partial y}\left(\frac{\partial u}{\partial y} + \frac{\partial v}{\partial x}\right) + \frac{\partial\mu}{\partial z}\frac{\partial u}{\partial z}\right) + \lambda(u_i - u) \qquad (4.14)$$

$$F_y = \frac{1}{\rho}\left(\mu\nabla^2 v + 2\frac{\partial\mu}{\partial y}\frac{\partial v}{\partial y} + \frac{\partial\mu}{\partial x}\left(\frac{\partial v}{\partial x} + \frac{\partial u}{\partial y}\right) + \frac{\partial\mu}{\partial z}\frac{\partial v}{\partial z}\right) + \lambda(v_i - v) \qquad (4.15)$$

$$\lambda = N\mu_{in}\nu_{in}/\rho \qquad (4.16)$$

$$\mu = A\,T^{0.69} \qquad (4.17)$$

76

where A is the molecular viscosity constant for the particular composition and density, and u_i and v_i are the ion velocities in the x and y directions, given by

$$u_i = V_{Hn}\sinD \cos^2 I - V_{D//}\sinI \cosI + U_{iE} \qquad (4.18)$$

$$v_i = V_{Hn}\cosD \cos^2 I - V_{D//}\cosD \cosI + V_{iE} \qquad (4.19)$$

with U_{iE} and V_{iE} the electric field drifts in the x and y directions. After scale analysis, the equations which were solved by Emery are

$$0 = -\frac{\partial u}{\partial t} + \frac{uv \tan\phi}{r} \frac{1}{\rho}\frac{\partial p}{\partial x} + fv + \frac{1}{\rho}\left(\mu\frac{\partial^2 u}{\partial z^2} + \frac{\partial\mu\partial u}{\partial z\partial z}\right) + \lambda(u_i - u) \qquad (4.20)$$

$$0 = -\frac{\partial v}{\partial t} - \frac{u^2 \tan\phi}{r} - \frac{1}{\rho}\frac{\partial p}{\partial y} - fu + \frac{1}{\rho}\left(\mu\frac{\partial^2 v}{\partial z^2} + \frac{\partial\mu\partial v}{\partial z\partial z}\right) + \lambda(v_i - v) \qquad (4.21)$$

Emery found that only the terms involving vertical gradients of μ, u, and v were important in the viscous force. The non-linear advection terms have also been neglected. The meridional gradient in velocity could only be included using a series of questionable assumptions about the latitudinal gradients in other parameters and then doing a three dimensional integration. The zonal gradient in velocity can be included explicitly using the assumption that longitudinal and local time derivatives are interchangeable. However, inclusion of these terms caused instability problems in the numerical integration scheme, and they were not included. The full non-linear semi-empirical model of Blum and Harris (1975a,b) suggested that including the non-linear terms would not have produced significantly different winds from those calculated using linear models. The non-linear model only showed a reduction in computed winds of a few per cent. Attempts by Emery (1977) to include some non-linear terms were not successful, but the various tests she undertook

77

suggest that the uncertainty due to their neglect is less than 20%.

4.3.2 The Analysis Procedure

The schema used to integrate the momentum equations involves using the observed neutral horizontal wind component, V_{Hn}, given in equation 4.7, and the derived T_∞ to create a system of three equations and three unknowns. The change in temperature with local time is equated to the zonal derivative, which is used to compute the zonal pressure gradient. The three equations are then equations 4.7, 4.20, and 4.21, and the three unknowns are u, v, and $\partial p/\partial y$, the meridional pressure gradient.

Since the model was developed to examine the diurnal variation of the winds, T_∞, V_{Hn}, and the derived meridional pressure gradient are fit to a third order sinusoidal polynomial in time so these parameters will be continuous over the 24 hour integration period. As the experimental values do not repeat exactly after 24 hours, some blending of the end points was sometimes needed before computing the fit.

The finite difference integration procedure used the Crank-Nicholson method assuming that $u = v = 0$ initially at all altitudes. The boundary conditions required $u_{120} = 0$ and $\partial u/\partial z \rightarrow 0$ at 600 km. At each time step, i, the zonal pressure gradient is used to solve equation 4.20 at all heights for $\partial u/\partial t$, so the value of u_{i+1} is known. Then equation 4.7 can be used to find v_{i+1}. This last computation is done using V_{Hn} calculated at 300 km and $u_{i+1}(300 \text{ km})$. Equation 4.21 can now be solved to determine the meridional pressure gradient at 300 km. Using equation 4.1 and assuming diffusive equilibrium, an "effective" meridional temperature gradient can be determined for the other altitudes, and with

78

this, the pressure gradients. From these pressure gradients, equation 4.21 can be solved at all altitudes. This procedure is iterated until the v_{i+1} computed using equation 4.7 and the $v_{i+1}(300$ km$)$ found when solving for all altitudes differ by less than 1 m/sec. In practice, this is only one or two iterations.

After integrating over 24 hours, the derived meridional pressure gradient at 300 km is fit to a third order harmonic. The equations are then intergrated for a second 24 hours using the harmonic fit for the derivatives and the u_{24} and v_{24} as initial conditions.

The model was also run for each day using the observed N to compute the ion drag force, but with pressure gradients that were taken from the MSIS model. Figures 4.2 and 4.3 give a schematic representation of the overall analysis procedure briefly outlined here.

4.3.3 Computation of Neutral Densities

As in the previous calculations of T_∞ and $V_{D//}$, the neutral densities were taken from the MSIS model. One of the main objectives of Emery's analysis was to determine if there are seasonal differences in the mean diurnal winds, which would be responsible for seasonal variations of the composition of the thermosphere detected by satellite borne mass spectrometers. Earlier, various ionospheric workers had concluded that such variations must exist, and using incoherent scatter measurements made at Millstone Hill, Cox and Evans (1970) determined the seasonal O/N_2 ratio variation at 198 km. In an effort to use ISR data to the fullest extent possible, Emery appealed to these results to introduce seasonal variations in the annual mean MSIS oxygen density,
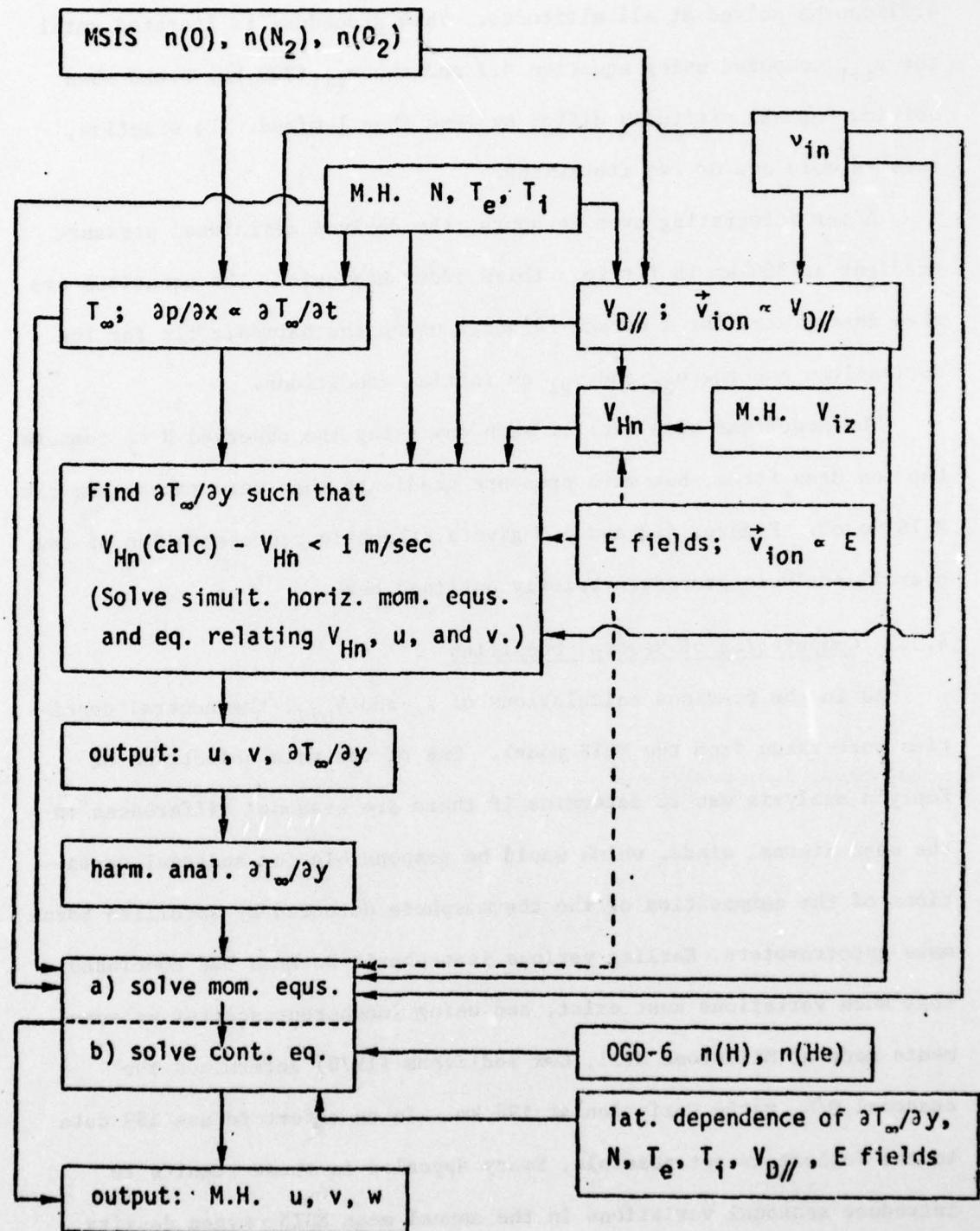
Figure 4.2 Flow diagram of EMH model processing procedures using Millstone data.
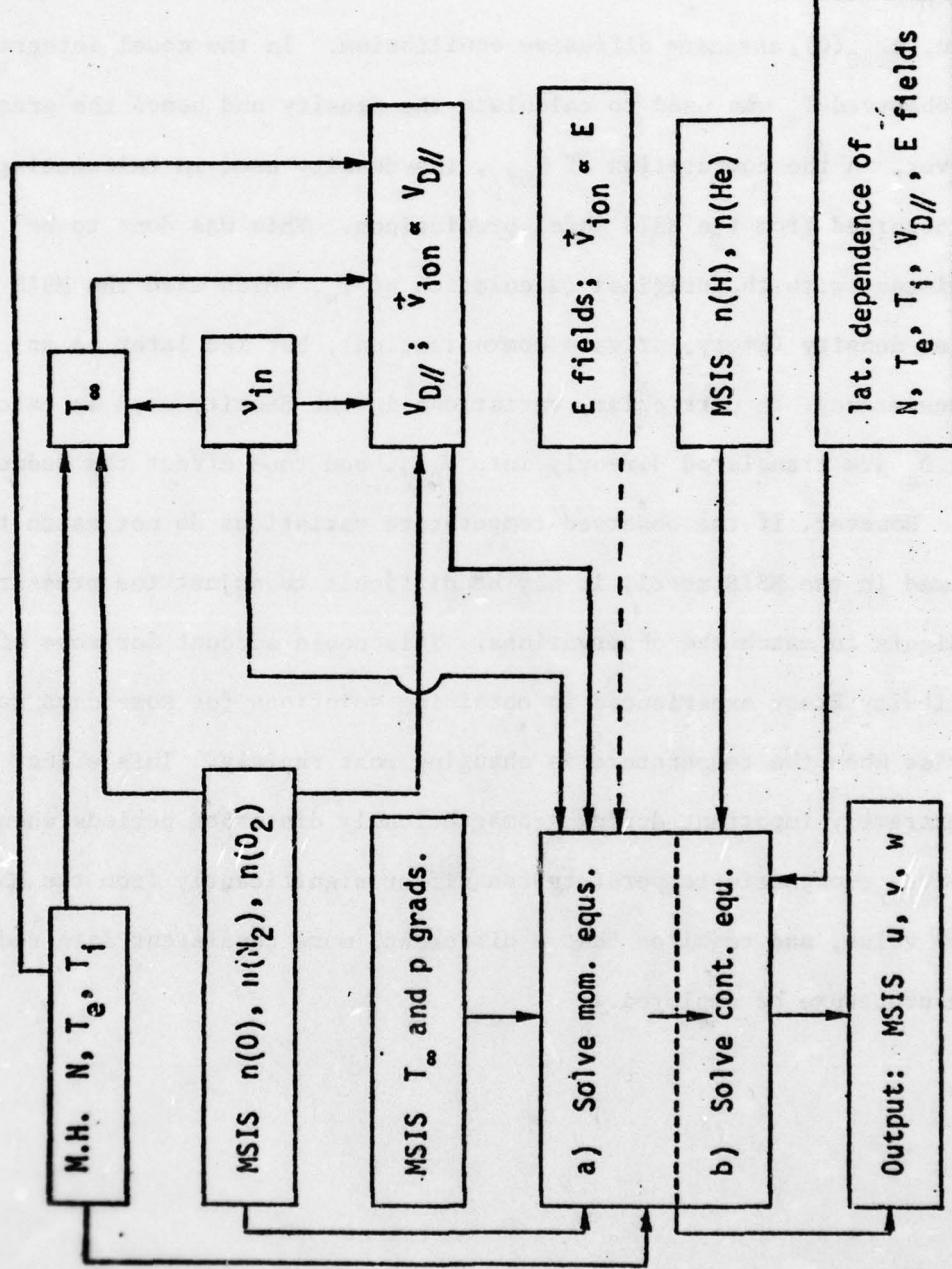
Figure 4.3 . Same as Figure 4.2 except for using MSIS model data.

keeping $n(N_2)$ constant, in order to duplicate the O/N_2 variations of Cox and Evans (1970). This was done by changing the MSIS oxygen density at 198 km by an appropriate factor and then deriving the boundary value, $n_{120}(0)$, assuming diffusive equilibrium. In the model integration, the observed T_∞ was used to calculate the density and hence the pressure. However, in the computation of $V_{D//}$, the density used in calculating D_a was obtained from the MSIS model predictions. This was done to be consistent with the original calculation of T_∞, which used the MSIS oxygen density (Emery, private communication), but led later to an inconsistency. In particular, variations in the density used in calculating D_a are translated directly into $V_{D//}$, and thus affect the deduced V_{Hn}. However, if the observed temperature variations do not match those assumed in the MSIS model, it may be difficult to adjust the pressure gradients to match the observations. This could account for some of the difficulty Emery experienced in obtaining solutions for some days near sunrise when the temperature is changing most rapidly. This effect can be extremely important during geomagnetically disturbed periods when the observed exospheric temperature can differ significantly from the MSIS model value, and requires that a different, more consistent data reduction procedure be employed.

82

5. NEW DATA ANALYSIS PROCEDURES

After the analysis of several geomagnetically disturbed days, it became clear that the derived exospheric temperatures and neutral winds differed significantly from the diurnal patterns for quiet days. Figure 5.1(a) compares T_∞ derived from incoherent scatter results for a disturbed day, 23-24 March 1972, and anticipated from the MSIS model for this particular day. The derived temperature is higher for all times, with a large nighttime enhancement being the most striking difference. Figure 5.1(b) compares the derived neutral wind, V_{Hn}, for this same disturbed day and for another vernal equinox day which was geomagnetically quiet. The disturbed day has generally a more equatorward flow, as would be expected as a consequence of high latitude heating. However, there is a large equatorward surge near local midnight which suggests that more than just auroral heating may be involved. Of the approximately 25 days examined in this work for which there was some enhancement in geomagnetic activity, the midnight surge is found to be the most consistent feature. The enhanced temperature is also often observed, but it is not always as pronounced. The magnitude of these two effects was dependent on the level of geomagnetic activity.

These two disturbance related effects have an impact on the way in which the data is analyzed. The combination of the nighttime temperature enhancement coincident with the strong winds suggested that the simple balance of equation 4.3 used to derive T_∞ is not a valid assumption. Since the EMH model provides the neutral wind components, the frictional heating due to the neutral wind blowing through the ions can be calculated explicitly and included in the balance.

83
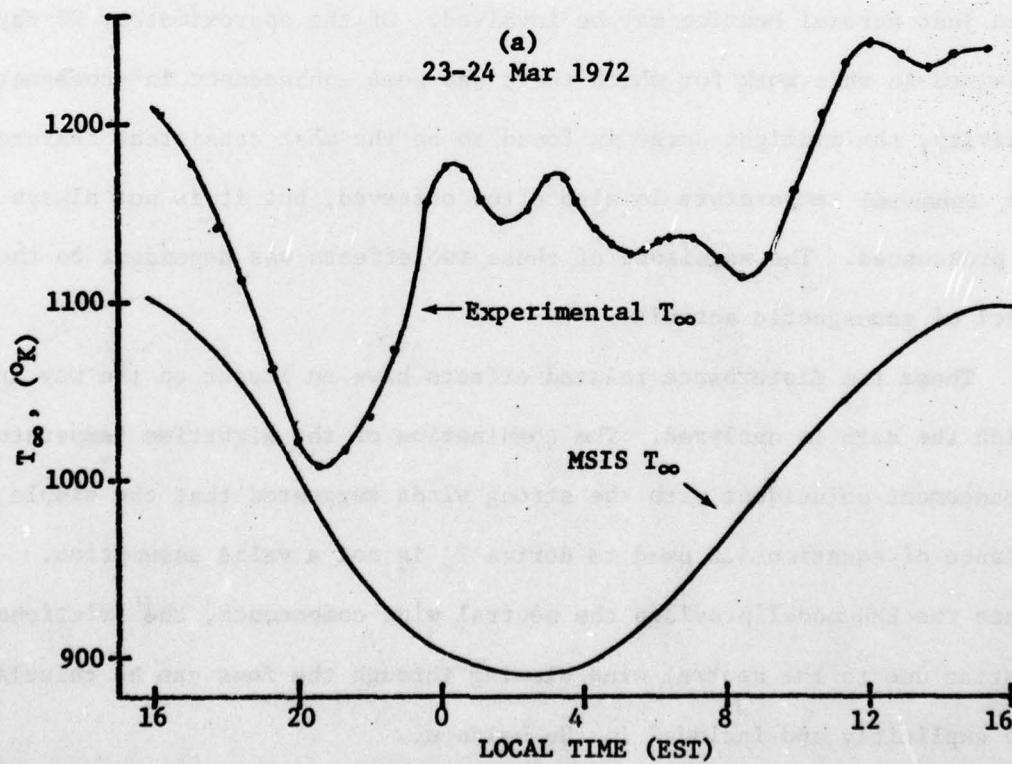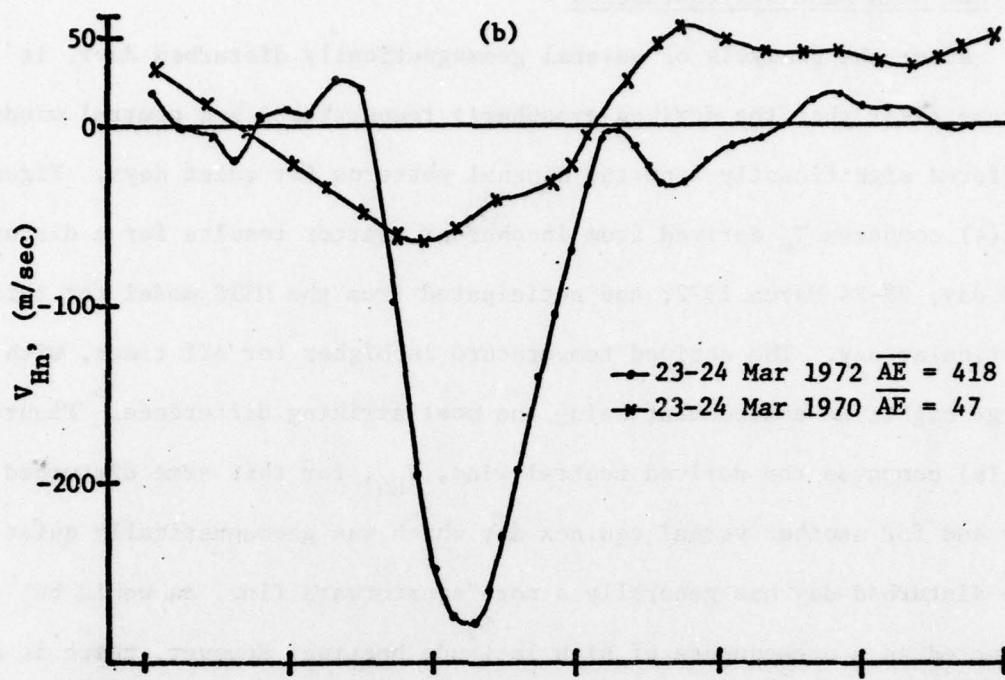
Figure 5.1 Comparison of (a) experimental and MSIS model T_∞ for disturbed day and (b) V_{Hn} for quiet and disturbed equinox days.

84

As described in Section 4.3.3, the MSIS model T_∞ is used to determine the neutral densities which go into computing $V_{D//}$. The marked departure of the nighttime temperature from the MSIS model value implies that the densities so obtained are in error, making the derived neutral wind also inaccurate.

Another source of uncertainty during disturbed periods is the effects of the large electric fields that may then be present at the latitude of Millstone. Indeed, it was initially thought that the midnight surge in the derived neutral wind might be a result of neglecting the E-field in computing V_{Hn}. A separate electric field observing program employing the method outlined in Chapter 3 has been conducted at Millstone Hill and has provided a large enough experimental data base to permit a test of the effects of electric fields on the results. Included in the data set were enough disturbed-day observations to create a separate average 'disturbed period' model field. In addition, there were two days of observations in which sufficient reliable measurements were made for a full 24 hours to determine separately the neutral winds and the electric fields without any assumptions; one day was very quiet and the other relatively disturbed. Using the models derived for quiet and disturbed days the electric field can be included explicitly in the calculations for all the other days also.

The first two sections of this chapter describe the new analysis procedures used to determine T_∞ and V_{Hn} and show some sample results. The last section discusses the electric field results which are used. The results from these new procedures are presented in Chapter 7.

85

5.1 Frictional Heating in the Ion Heat Balance Equation

The use of the simple heat balance given by equation 4.3 to derive T_∞ is a standard method used to analyze incoherent scatter data (Nisbet, 1967; Bauer et al, 1970; Salah, 1972). Stubbe and Chandra (1971) performed some sample calculations to explore the effect of frictional heating by the neutral winds using the one-dimensional model of Stubbe (1970). Using neutral winds derived from the Jacchia (1965) static diffusion model, they found that the larger nighttime winds would effect the derived neutral temperature. In trying to determine why the simultaneous calculation of $n(0)$ and T_∞ gave questionable results for $n(0)$ near dawn and dusk, Alcayde and Bauer (1977) showed that neutral winds on the order of 300 m/sec would cause frictional ion heating, P_{in}, of the same order of magnitude as the electron heating, P_{ie}, in the altitude region 300 to 400 km. At high latitudes, Joule heating is an important heat source for the ions. Using ion velocities measured by the Chatanika ISR and taking $V_n = 0$, Watkins and Banks (1972) found the Joule heating term important in computing T_∞. To test this effect at mid-latitudes, the winds computed by the EMH model were fed back into the balance equation to determine the effect on the derived T_∞.

The frictional heating rate for a single ion, $n(0^+)$, is given by

$$P_{in} = n(0^+) \frac{\mu_{in}^2}{m_i} \nu_{in} (\bar{V}_i - \bar{V}_n) \qquad (5.1)$$

The collision frequency is taken from Banks and Kockarts (1973). The collision frequencies of the ions with N_2 and O_2 are an order of magnitude smaller than with O, and were not included in the calculation. Substituting the expression for ν_{in} into equation 5.1 yields

86

$$P_{in} = 9.98 \times 10^{-21} N \, n(0)(T_i + T_n)(10.6 - .67 \log(T_i + T_n))^2 \, x$$

$$(\overline{V}_i - \overline{V}_n)^2 \quad eV/cm^3 sec \tag{5.2}$$

where $\overline{V}_i$ and $\overline{V}_n$ are in m/sec. It is assumed that the ion velocity components given by equations 4.18 and 4.19 can be approximated by just the electric field drifts. Because of the sinD and cosD factors, the $V_{D//}$ and V_{Hn} components are small relative to $\overline{V}_{iE}$. The electric field drifts are normally small during quiet times, so it can be assumed $u_{iE} = v_{iE} = 0$ relative to $\overline{V}_n$. However, since the components can be large during disturbed periods, it is appropriate that they be included. As noted above, except for the two days when coincident electric field measurements were available, the models discussed in Section 5.3 are used to find u_{iE} and v_{iE}.

Any change in the derived T_∞ values will result in a change in the zonal temperature gradient, and thus the winds computed by the EMH model. A more subtle impact on the model winds arises from a change in the neutral density, which is computed using T_∞. To determine the final temperature values, the new values were applied to the model to derive new pressure gradients and compute new winds (and hence frictional heating). These winds, in turn, were reapplied to the temperature calculation, etc. This iterative procedure normally took two or three steps before a convergence to the final value was achieved.

Figure 5.2 compares the initial temperature pattern for the disturbed day 23-24 March 1972 and the final values that allow for frictional heating. Although the nighttime temperature enhancement is reduced, it is still quite significant. The temperatures at other times were reduced

87
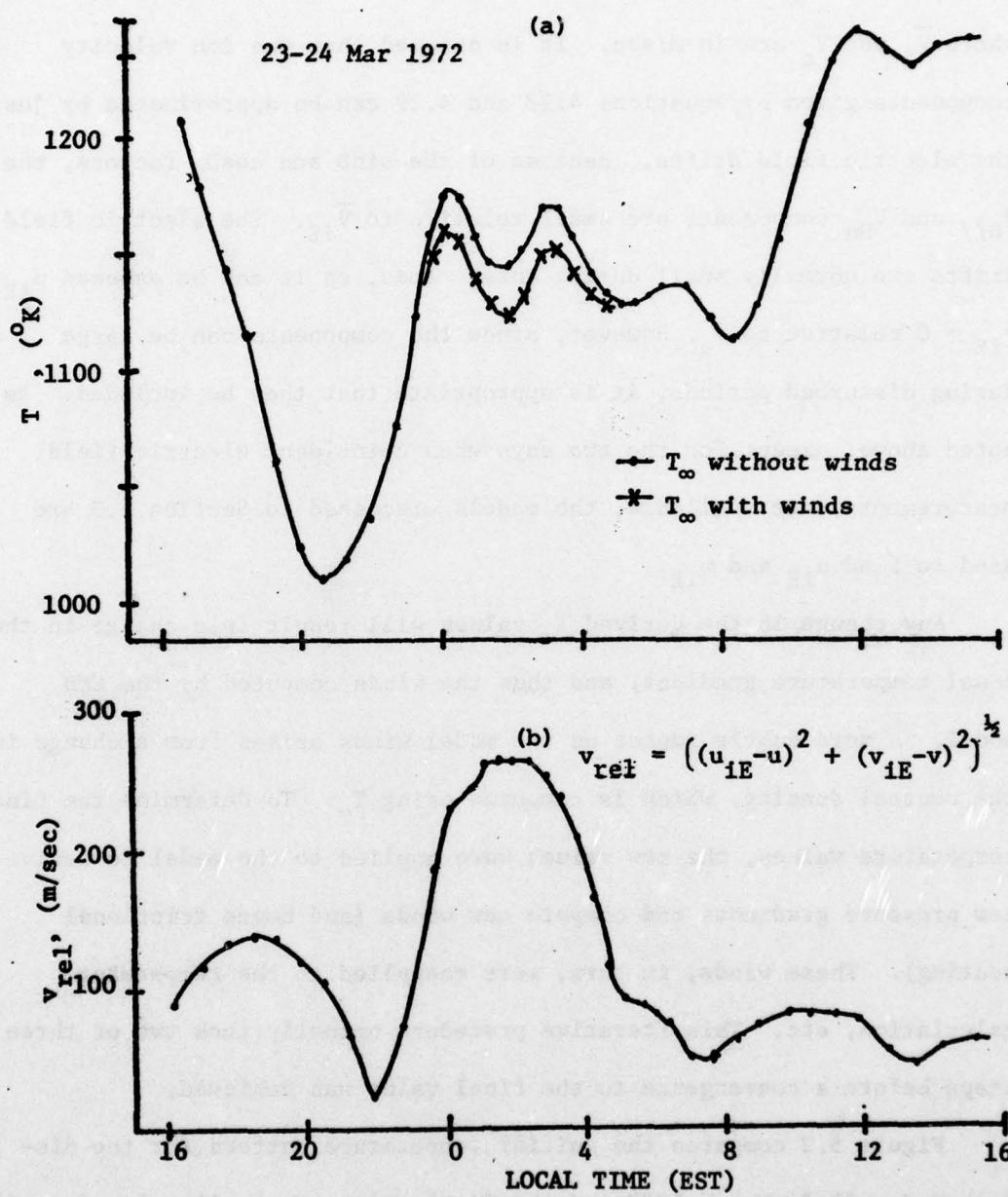
Figure 5.2 (a) Difference in the derived T_∞ when neutral wind heating is included. (b) The relative ion-neutral velocity which goes into the neutral heating term.

88

by only 2-4 $^{\circ}$K. Plotted with the temperatures in Figure 5.2 is the magnitude of the vector difference between the ion drifts and the neutral winds, i.e. the relative wind used in computing the friction term. As expected, as the relative wind increases, the derived T_{∞} decreases. This is because the ion thermal balance equation has become

$$L_i(T_i - T_n) = P_{ie}(T_e - T_i) + P_{in}(\bar{v}^2) \qquad (5.3)$$

where the terms in parentheses are the primary terms on which the computed balance depends. The addition of frictional heating increases in the right-hand side of equation 5.3 and requires a higher temperature difference between the ions and neutrals. Since T_i is fixed by the data, the increased difference results in a reduced T_n.

Figure 5.3 compares the zonal gradient of T_{∞} for the curves in Figure 5.2. Also plotted is the temperature gradient from the MSIS model. Since the nightime temperature is smaller for the corrected T_{∞} curve, the perturbation in the nighttime zonal gradient has been reduced. This will have an effect on the computed winds.

Figures 5.4 show the (a) meridional and (b) zonal winds derived using the original and final temperature profiles. The observed wind, V_{Hn}, was derived using T_{∞} to compute the densities. Electric field induced ion drifts computed using the 'disturbed' model field were also included in the computation of V_{Hn} and the ion drag term in the EMH model. The reduced T_{∞} and computed densities near midnight come into play in the pressure and ion drag terms of the model to reduce the calculated winds. Since the pressure (temperature) gradient for this

89
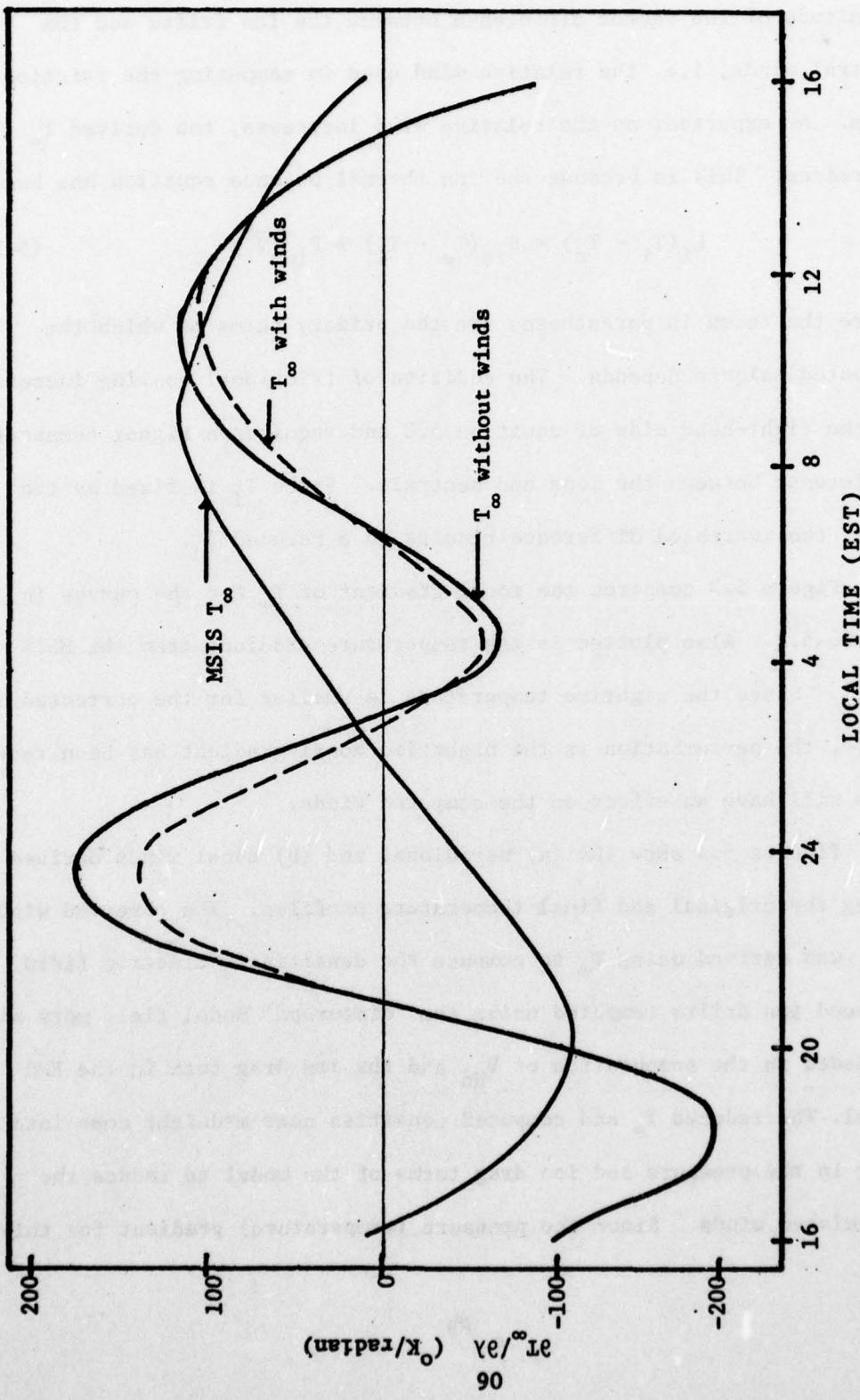
Figure 5.3 Horizontal temperature gradient for the exospheric temperature derived with (dashed) and without (solid) neutral wind heating included in the ion balance.
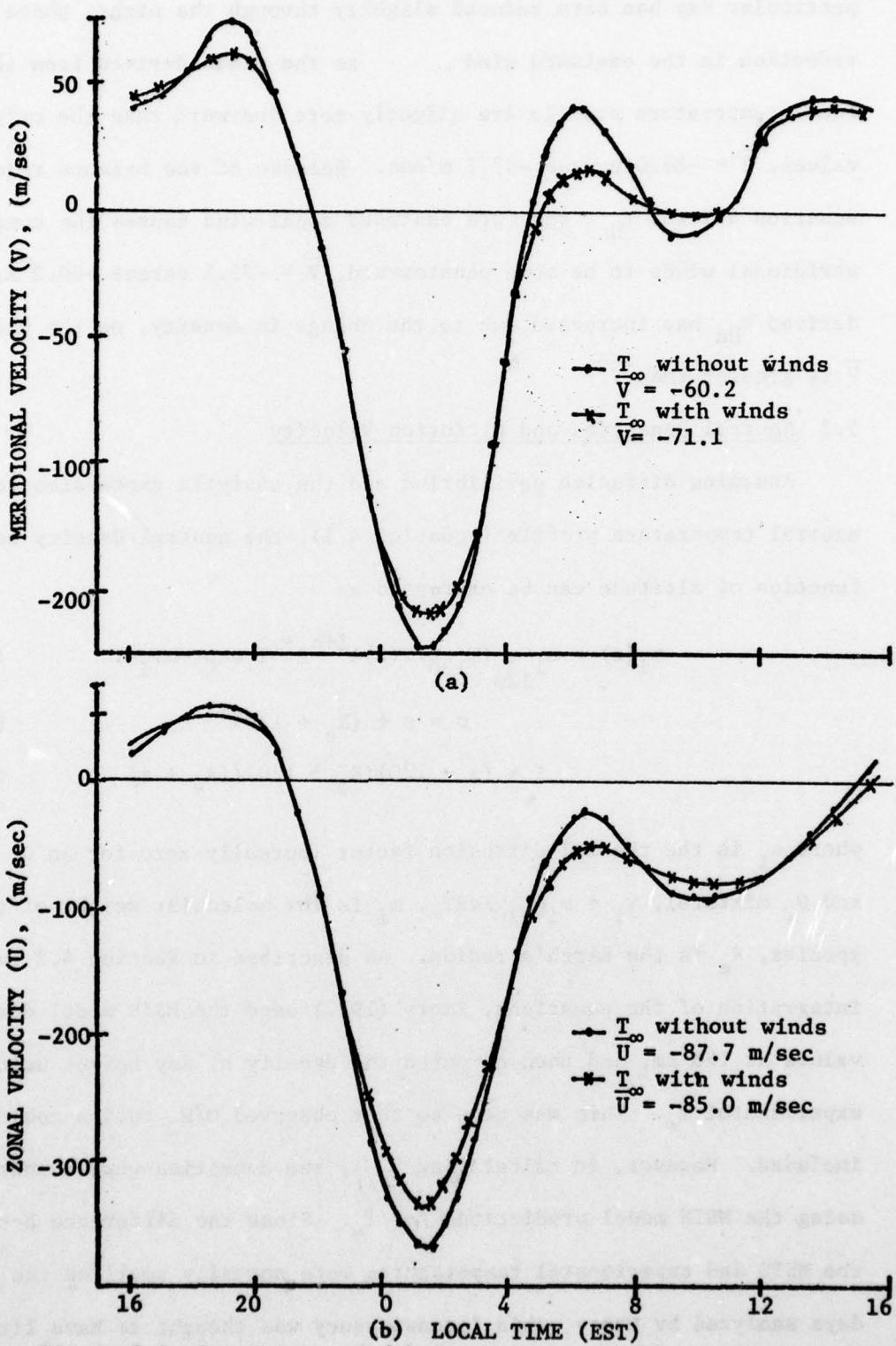
Figure 5.4 Comparison of (a) meridional and (b) zonal winds from the EMH model using the T_∞ derived with and without neutral heating.

91

particular day has been reduced slightly through the night, there is a reduction in the eastward wind, so the winds derived from the final temperature profile are slightly more westward than the original values, $\overline{U} = -86.0$ versus -87.7 m/sec. Because of the balance required by equation 4.7 for V_{Hn}, the more eastward zonal wind causes the computed meridional winds to be more equatorward, $\overline{V} = -71.1$ versus -60.2 m/sec. The derived V_{Hn} has increased due to the change in density, so the change in $\overline{V}$ is greater than $\overline{V}$.

5.2 Neutral Densities and Diffusion Velocity

Assuming diffusive equilibrium and the analytic expression for the neutral temperature profile (equation 4.1), the neutral density as a function of altitude can be expressed as

$$n_i(z) = n_{i_{120}} (T_{120}/T(z))^{1+\alpha_i+\gamma_i} \exp(-\sigma\gamma_i\xi) \qquad (5.4)$$

$$\sigma = s + (R_e + 120)^{-1} \qquad (5.5)$$

$$\xi = (z - 120)(R_e + 120)/(R_e + z) \qquad (5.6)$$

where α_i is the thermal diffusion factor (normally zero for an O, N_2, and O_2 mixture), $\gamma_i = m_i g_{120}/\sigma R T_\infty$, m_i is the molecular weight of the species, R_e is the Earth's radius. As described in Section 4.3 in the integration of the equations, Emery (1977) used the MSIS model density values at 120 km, and then computed the density at any height using the experimental T_∞. This was done so that observed O/N_2 ratios could be included. However, in calculating $V_{D//}$, the densities were computed using the MSIS model predictions for T_∞. Since the difference between the MSIS and experimental temperatures were normally small on the quiet days analyzed by Emery, this inconsistency was thought to have little

92

effect. However, the significant departure of T_{∞} from the MSIS model on disturbed days requires that a different approach be adopted.

Although the changes in the vertical gradients of the ionospheric paramenters in equation 4.8 during disturbed periods will be reflected in the calculated values of $V_{D//}$, the neutral density values chosen can have a large effect. From equation 4.11, the ambipolar diffusion coefficient is given by

$$D_a = \frac{k(T_e + T_i)}{\nu_{in}\mu_{in}} \tag{4.11}$$

where

$$\nu_{in} \propto n(O) \tag{5.8}$$

Thus $V_{D//}$ can be seen to be inversely proportional to the neutral density, which at 300 km is approximately just $n(O)$. For most cases, $V_{D//}$ and the observed V_{iz} at 300 km are both downward throughout the day. In computing V_{Hn}

$$V_{Hn} \simeq \frac{V_{D//}}{cosI} + \frac{V_{iz}}{cosIsinI} \tag{5.9}$$

a decrease in the absolute value of $V_{D//}$, i.e. an increase in $n(O)$, will mean an increase in V_{Hn} (a more poleward wind).

There is observational evidence that there is an increase in the neutral density in the midnight sector during geomagnetic disturbances (Trinks et al, 1976). Hedin et al (1977) examined AE-C measurements of $n(O)$ made at $42^{\circ}N$ and 160 km and found the densities to be about 20% higher than the MSIS model values during the night.

93

The dependence of the EMH model on densities derived from another model, MSIS, is, perhaps, one of the weaker points of this analysis. However, comparisons of MSIS model densities with recent experimental data has been fairly good (Sharp et al, 1978; Trinks et al, 1978; and von Zahn and Fricke, 1978).

Figure 5.5(a) compares the diffusion velocity calculated with the two different density estimates (i.e. equation 5.4 or the MSIS prediction). The diurnal pattern is the same for each, since this is specified by the diurnal variation in the vertical gradients, which is taken from the data for each method. The difference in magnitude during the night is just due to the difference in densityand depends on how closely the observed T_∞ follows the MSIS prediction.

Figure 5.5(b) compares the deduced neutral wind component, V_{Hn}. the divergence in the two values during the night is clear, with the difference at the maximum in the midnight surge of about 170 m/sec.

5.3 Electric Fields

The electric field enters into the analysis in three places. In the original model, the electric field must be considered in the computation of V_{Hn} and in the ion drag term in the integration of the momentum equations. With the inclusion of the frictional heating term in the ion heat balance equation, ion drift velocities must be included to compute the relative ion-to-neutral velocity.

For the specific geometry of Millstone Hill, the horizontal components of the electric field drifts are given by

$$U_{1E} = .97 \, V_{ewE} - .23 \, V_{nsE} \qquad (5.9)$$

$$V_{1E} = .92 \, V_{nsE} + .24 \, V_{ewE} \qquad (5.10)$$
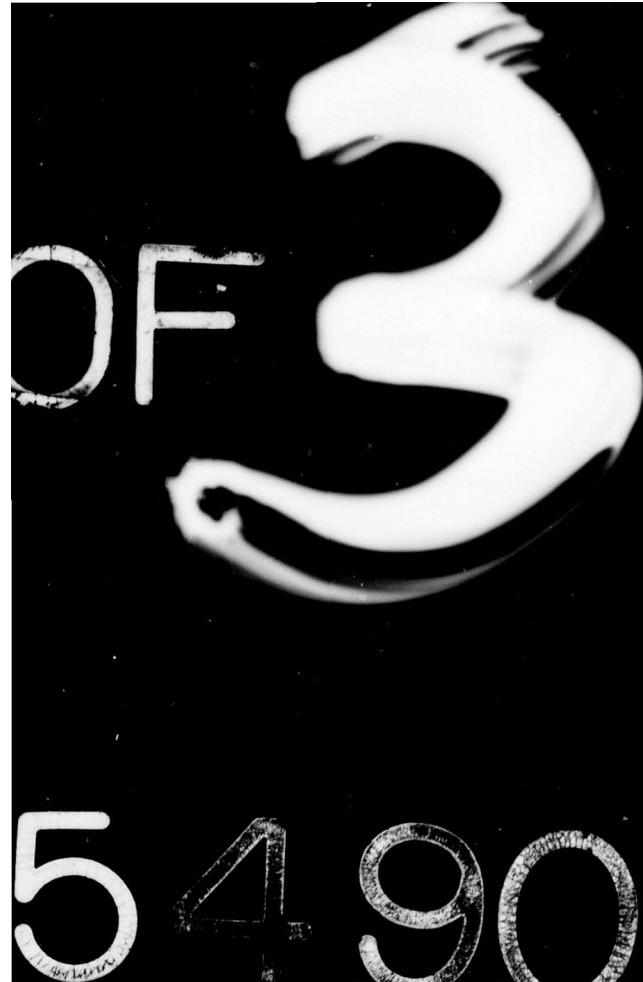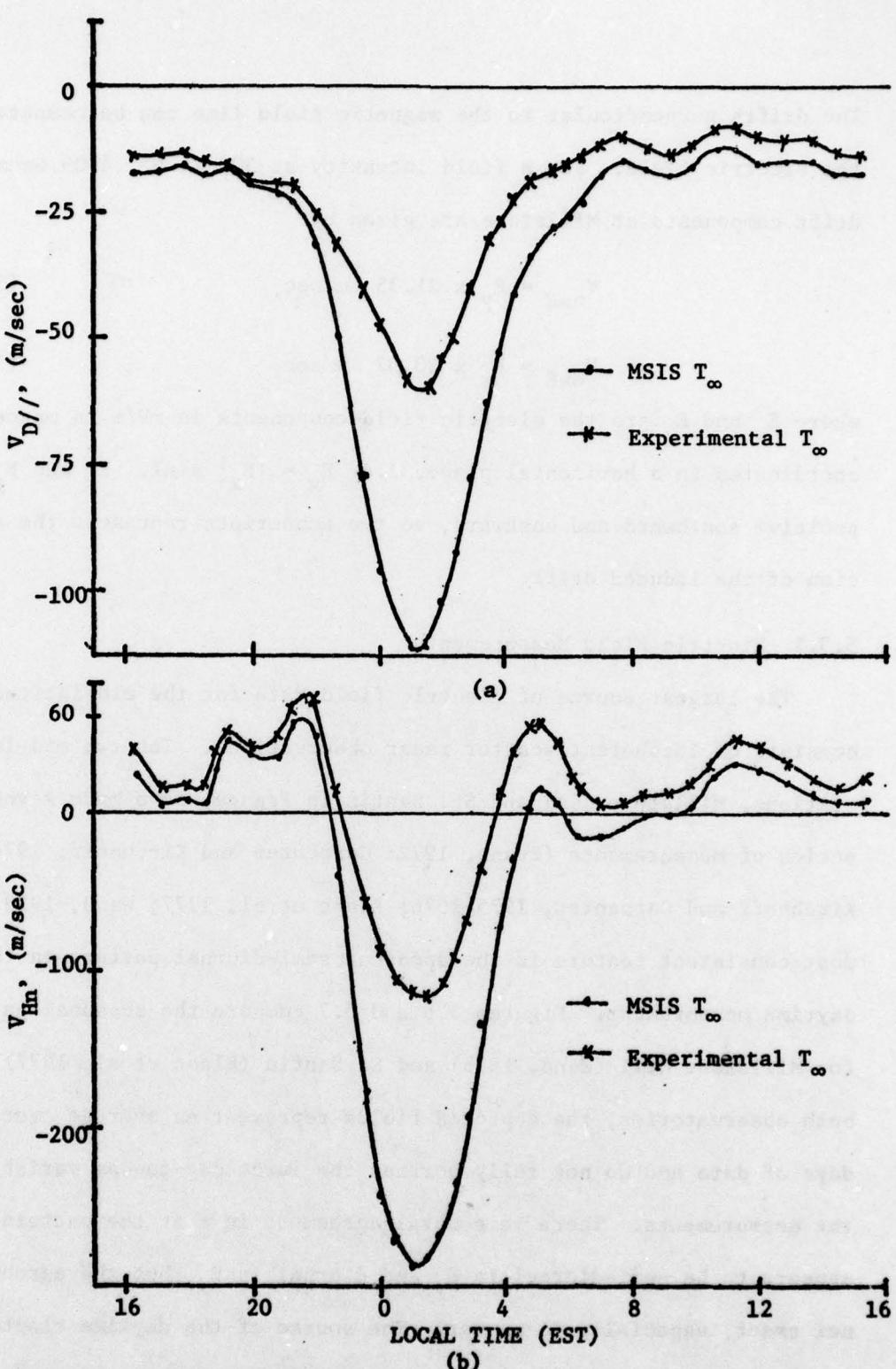
Figure 5.5 Difference in (a) $V_{D//}$ and (b) V_{Hn} when experimental and MSIS T_∞ are used to compute the densities.

95

The drifts perpendicular to the magnetic field line can be computed from the electric field. For a field intensity at 300 km of .4909 Gauss, the drift components at Millstone are given by

$$V_{nsE} = E_y \times 21.35 \quad m/sec \qquad (5.11)$$

$$V_{ewE} = E_x \times 20.37 \quad m/sec \qquad (5.12)$$

where E_x and E_y are the electric field components in mV/m in magnetic coordinates in a horizontal plane, i.e. $E_x = |\overline{E}_x|$ sinI. E_x and E_y are positive southward and eastward, so the subscripts represent the direction of the induced drift.

5.3.1 Electric Field Measurements

The largest source of electric field data for the mid-latitudes consists of incoherent scatter radar observations. The two mid-latitude stations, Millstone Hill and St. Santin in France, have made several series of measurements (Evans, 1972; Carpenter and Kirchhoff, 1974; Kirchhoff and Carpenter, 1975,1976; Blanc et al, 1977; Wand, 1978). The most consistent feature is the apparent semi-diurnal pattern in the E_y daytime measurement. Figures 5.6 and 5.7 compare the seasonal patterns for Millstone Hill (Wand, 1978) and St Santin (Blanc et al, 1977). For both observatories, the depicted fields represent an average over several days of data and do not fully portray the large day-to-day variation in the measurements. There is general agreement in that the pattern appears to be semi-diurnal in E_y and diurnal in E_x, but the agreement is not exact, especially in summer. The source of the daytime electric field in the F-region is thought to be a polarization field produced in the E-region by the dynamo effect of semi-diurnal tides. Richmond et al

96
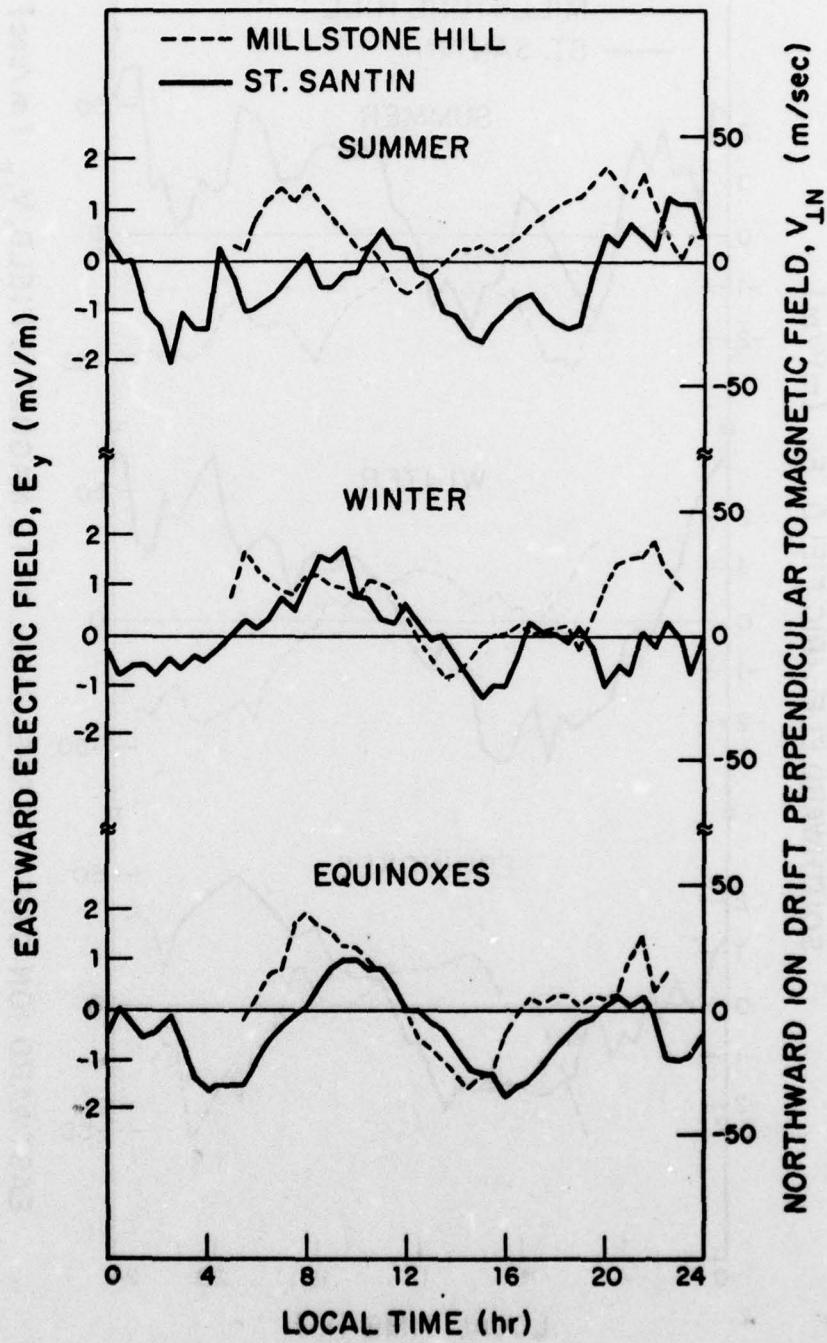
Figure 5.6 Comparison of average eastward electric field patterns observed at Millstone and St Santin.

97
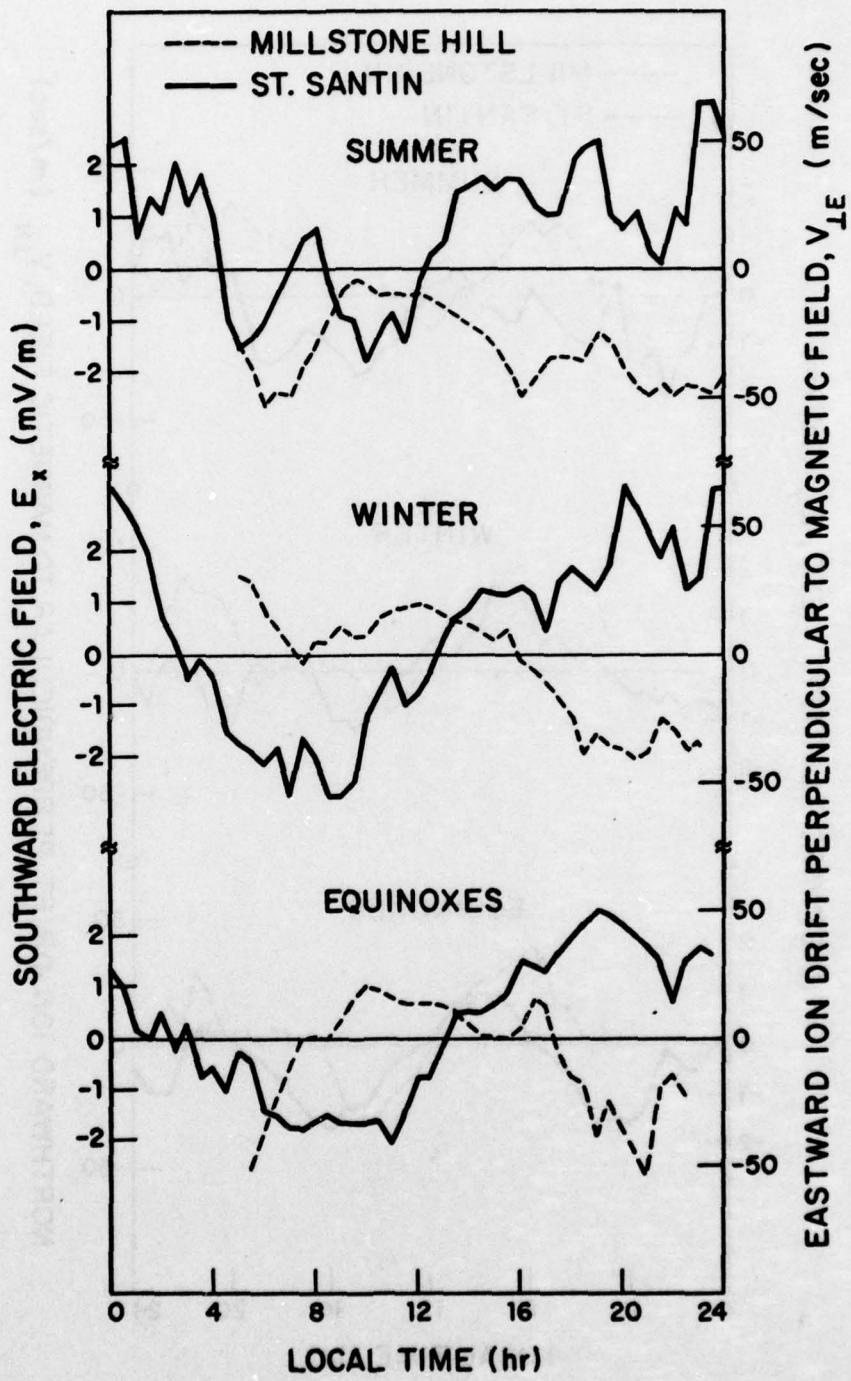
Figure 5.7 Same as Figure 5.6 except for southward electric field.

(1976) have been able to reproduce the diurnal S_q current pattern seen in magnetometer data using a model of the diurnal and semi-diurnal tidal modes, but they could not reproduce the observed electric field pattern. It appears that conjugate point effects play a role in determining the total electric field. For Millstone Hill the conjugate point is at 76^oS and would presumably have a quite different tidal pattern. The role of conjugate point fields could also explain the difference observed between Millstone Hill and St Santin.

The nightime field pattern has been less well determined. This is partly due to the smaller number of useful observations. The low electron densities prevailing at night have made reliable measurements difficult or impossible with the apparatus available. Comparison of some nighttime measurements made at the high latitude ISR at Chatanika with Millstone Hill data (Carpenter and Kirchhoff, 1975) shows a close agreement in the nighttime pattern, with the Millstone Hill fields about an order of magnitude smaller. This suggests that the nighttime fields are primarily of magnetospheric origin. Very recent measurements of the latitudinal variation of the electric field between L = 4 and L = 7 at Millstone Hill using the new steerable antenna tend to support this conclusion.

5.3.2 Application of Model Fields

Emery (1977) tested the effect of including electric field drifts in her calculations by including the average field model of Kirchhoff and Carpenter (1975) which was derived from Millstone Hill data. The data base included 12 days of observations made during geomagnetically quiet periods ($\Sigma K_p \leq +18$). The data were fit to a fifth order sinusoidal polynomial in local time. For the two days Emery analyzed, the

99
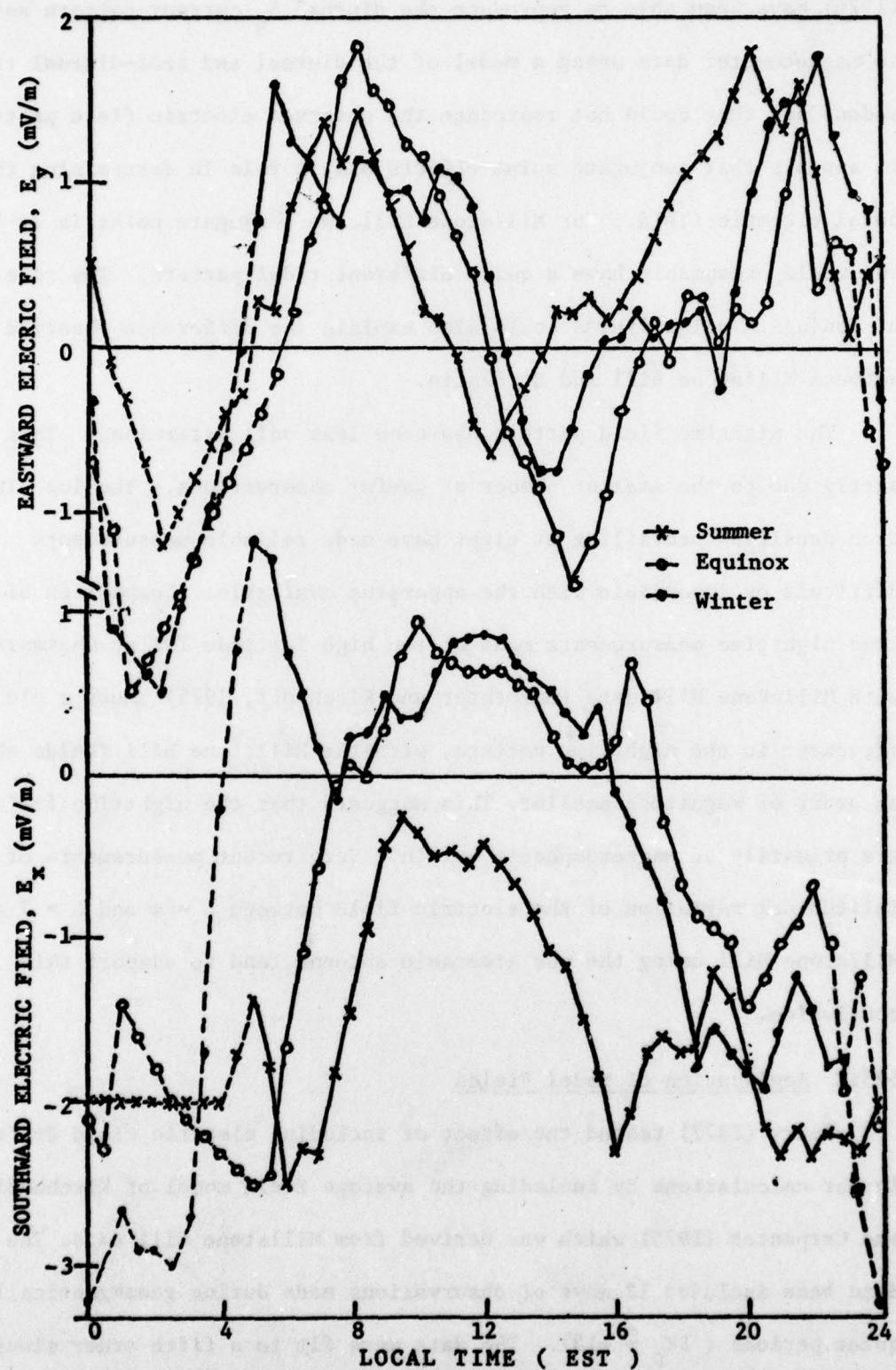
Figure 5.8 Averaged electric field values obtained by Wand (1978) at Millstone. The dashed curves represent nighttime values which are more uncertain than daytime values.

combination of the decreased V_{Hn} computed with the fields and the effect of the ion drifts on the ion drag term resulted in the diurnally averaged winds becoming about 11 m/sec more northward and 3 m/sec more eastward. To a first approximation it appeared that the winds calculated without including electric fields are indeed valid in the rest frame of the ions.

To test these conclusions, further calculations have been undertaken here. Using the seasonal averages of Wand (1978), shown in Figure 5.8, a series of days in each season in 1972 and 1973 were analyzed. (Wand's original averages did not include nighttime values because of the low number of samples.) A plausible nighttime field was constructed (shown as broken lines in Figure 5.8) from these few samples, using other models as a guide.

The winter and equinox electric fields introduced only a small effect on the quiet day winds calculated and changed the diurnally averaged winds by a few m/sec. For the summer days, the predominantly northward field (westward drift) caused the computed zonal wind to be about 15 m/sec more westward. Although the generally westward field was a consistent feature in the 9 summer days observed, the magnitude was quite variable. This large day-to-day variability in the field makes the inclusion of a model field of questionable value for improving the accuracy of the results on a given day.

However, it was felt that the inclusion of a model field in the analysis of disturbed days was important, since the fields can then be quite large. Wand (private communication, 1978) has collected data
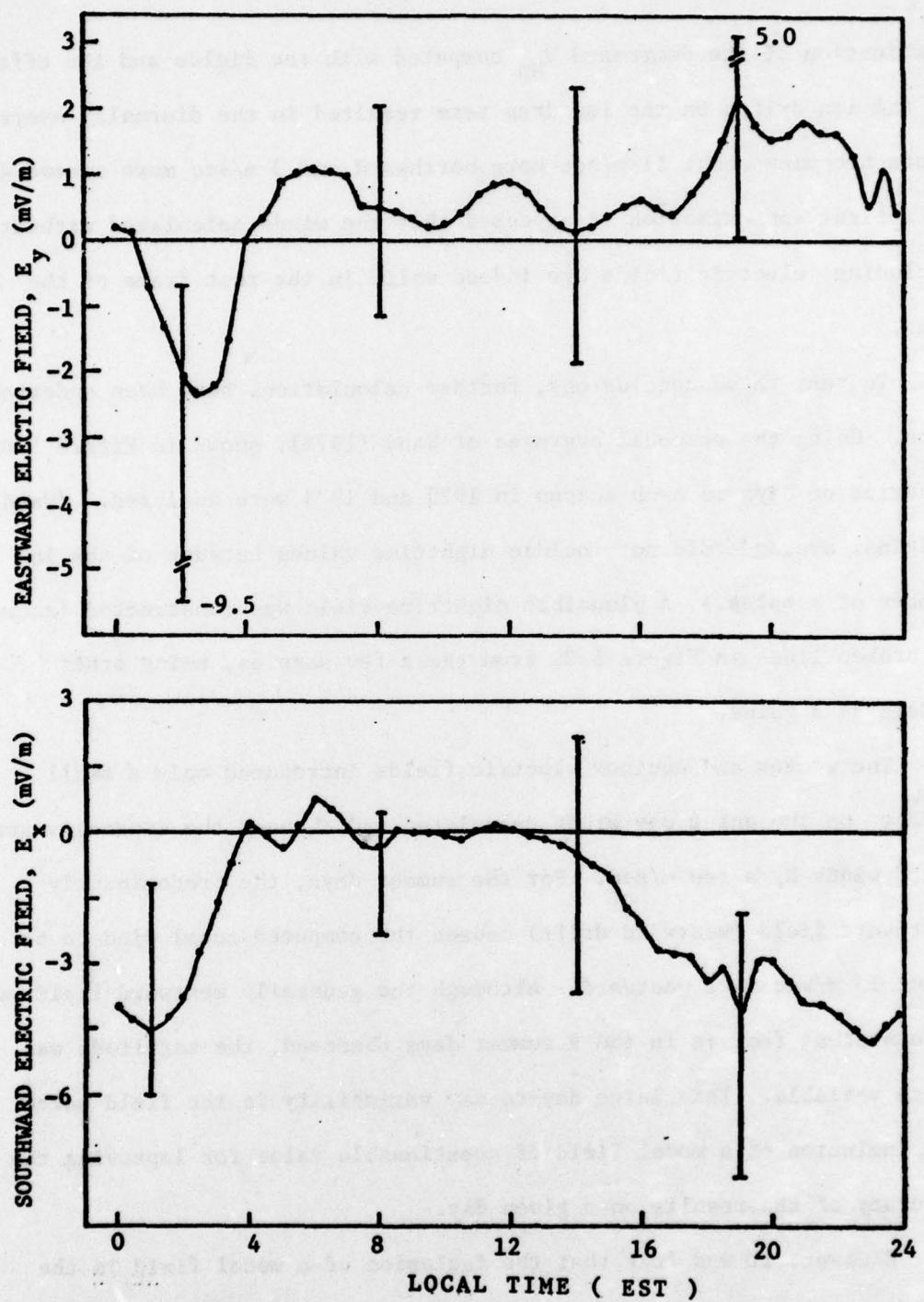
Figure 5.9 Electric field model for disturbed days obtained from average of disturbed days observed by Wand (1978).

102

during about about 15 days of observations during geomagnetically active
periods. For all but two days, there were some hours for which the data
were unreliable, mostly at night. The model field was constructed by
averaging the values for each half-hour observation. Figure 5.9 shows
the average disturbed model fields and indicates the spread in the
values. As on the quiet days, there were large variations from day to
day, although the semi-diurnal pattern in E_y is still present. The
disturbed period nighttime field is probably very sensitive to auroral
substorm activity, which has a time scale of 1 - 2 hours. Despite this,
the primary features of the disturbed field should be represented in the
average. As can be seen in Figure 5.9, these include the turning from
a strong eastward to a strong westward field about midnight, the appear-
ance of a strong northward field near dusk, and the persistance of a
strong northward field through the night. Actually, the pattern of
behavior for the disturbed model does not differ significantly from that
on quiet days, except in the dusk sector, and for a change in magnitude.

6. VARIATIONS IN THE DIURNALLY AVERAGED NEUTRAL WINDS

The initial impetus of this research was to examine the changes in the thermospheric circulation during geomagnetically disturbed periods, using the quiet period results of Emery (1977) as a reference. In order to study disturbed days which extend over a period of years when the level of solar activity was decreasing, it seemed necessary to determine what changes, if any, occurred in the quiettime circulation in order to have a valid reference point. The results of semiempirical models such as that of Dickinson et al (1975,1977) and Roble et al (1977) predict a gradual decrease in the asymmetry of the seasonal meridional wind pattern. This model is probably the most sophisticated thermospheric model (Evans, 1976), and the results are presented as zonally averaged values, which makes for easy comparison with the diurnally averaged values from the EMH model. As shown in Figure 6.1, there is also a reduction during solar minimum of the oxygen anomaly effects implied from ionospheric observations (Ratcliffe and Weekes, 1960). (Reference Section 2.4.1 for a discussion of the oxygen anomaly.) The analysis of all available "one-pulse" data, both disturbed and quiet, provided an additional dividend. First the model predictions of a solar cycle variation could be tested. Second, the model predicts a modulation of the winds with changes in the auroral heating (ref. Section 2.1). A statistical study of the winds as a function of some index that varies with high latitude heating could be undertaken to test this prediction.

6.1 Data Base

In addition to thirty seven days between December 1969 through

104
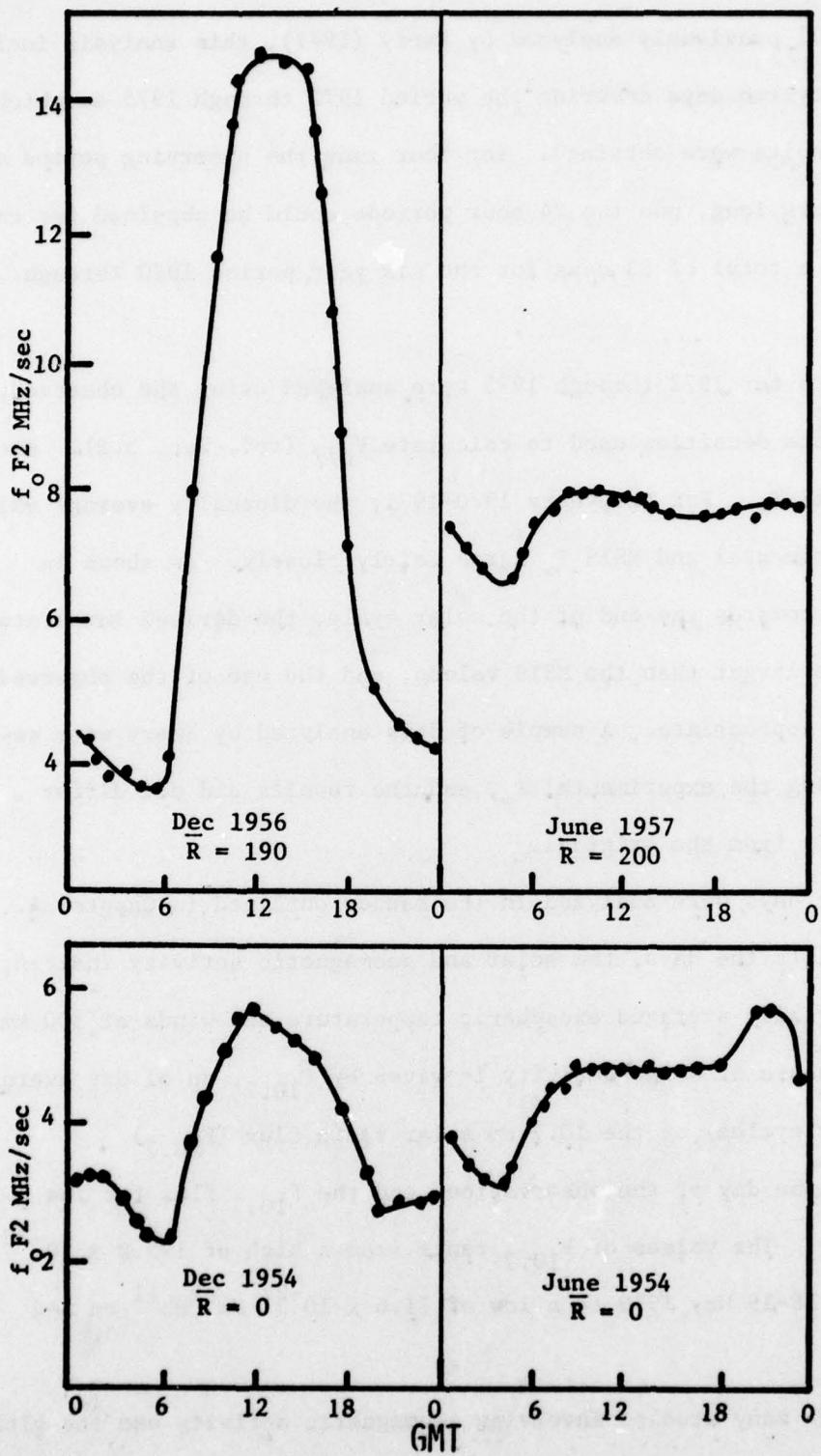
Figure 6.1   Reduction of the seasonal oxygen anomaly effect
as seen in f_oF2 with a decrease in sunspot number ($\bar{R}$).

December 1971 previously analyzed by Emery (1977), this analysis includes
another forty-two days covering the period 1972 through 1975 on which
reliable results were obtained. For four runs the observing period was
36 to 48 hours long, and two 24 hour periods could be obtained for each
run, giving a total of 83 days for the six year period 1970 through
1976.

The data for 1972 through 1975 were analyzed using the observed T_∞
to compute the densities used to calculate $V_{D//}$ (ref. Sec. 5.2). Emery
used the MSIS T_∞. For the years 1970–1971, the diurnally average values
of the experimental and MSIS T_∞ agree fairly closely. As shown in
Figure 6.2, towards the end of the solar cycle, the derived temperature
tended to be larger than the MSIS values, and the use of the observed T_∞
seemed more appropriate. A sample of days analyzed by Emery were re-
analyzed using the experimental T_∞, and the results did not differ
significantly from the original.

All the days were analyzed in the manner outlined in Chapter 4.
Table 6.1 lists the days, the solar and geomagnetic activity indices,
and the diurnally averaged exospheric temperature and winds at 300 km.

The measure of solar activity is given by $\overline{F}_{10.7}$, an 81 day average
(three solar cycles) of the 10.7 cm solar radio flux ($F_{10.7}$)
centered on the day of the observation, and the $F_{10.7}$ flux for the
previous day. The values of $F_{10.7}$ range from a high of 195.0×10^{-22}
$Wm^{-2}Hz^{-1}$ on 18–19 May 1970 to a low of 71.6×10^{-22} $Wm^{-2}Hz^{-1}$ on 3–4
Apr 1974.

Although many studies involving geomagnetic activity use the global
K_p or A_p indices, these indices are based on mid and high latitude mag-

106

Table 6.1 List of days analyzed, their solar and geomagnetic indices, diurnally averaged meridional and zonal winds, and diurnally averaged exospheric temperature.

Day	$\overline{F}_{10.7}$	$F_{10.7}$	$\overline{AE},\gamma$	$\overline{V}$,m/sec	$\overline{U}$,m/sec	$\overline{T}_\infty,^\circ K$
08–09 Dec 69	146.9	114.3	134	1.5	27.6	963
17–18 Feb 70	162.6	193.7	196	5.0	19.5	1094
23–24 Feb 70	163.8	183.8	149	18.9	24.8	1019
17–18 Mar 70	165.8	135.7	115	−31.5	−19.5	1105
23–24 Mar 70	166.5	163.1	47	5.6	4.7	1078
14–15 Apr 70	164.0	178.6	59	−28.6	−19.0	1086
12–13 May 70	166.2	179.6	237	−53.5	−79.2	1145
18–19 May 70	164.2	195.0	176	−51.5	−18.0	1201
10–11 Jun 70	163.0	140.4	178	−96.9	−60.9	1126
23–24 Jun 70	161.7	143.8	127	−41.7	−5.0	1100
07–08 Jul 70	154.6	171.3	319	−95.0	−67.6	1155
18–19 Jul 70	154.4	129.1	126	−58.2	−17.9	1094
17–18 Aug 70	144.8	153.9	409	−64.2	−17.9	1275
24–25 Aug 70	144.3	140.9	283	−64.5	−77.2	1144
31Aug–1Sep 70	144.9	153.5	324	−12.5	−9.3	1160
16–17 Sep 70	143.0	118.2	198	−24.2	−33.4	1041
28–29 Sep 70	146.2	144.6	56	28.4	28.5	1081
05–06 Oct 70	147.5	135.0	102	3.8	16.5	1035
13–14 Oct 70	151.0	132.5	172	7.0	10.5	1076
08–09 Nov 70	153.2	145.6	156	0.2	0.0	1104
21–22 Dec 70	154.9	147.5	132	18.3	35.2	1050
28–29 Dec 70	152.8	117.6	186	23.6	9.4	1028
11–12 Jan 71	147.5	149.3	60	34.0	37.7	1012

107

Day	$\overline{F}_{10.7}$	$F_{10.7}$	$\overline{AE}$	$\overline{V}$	$\overline{U}$	$\overline{T}_\infty$
20–21 Jan 71	145.3	168.3	243	30.2	50.4	1020
19–20 Feb 71	133.8	130.7	180	-4.9	-3.6	1040
08–09 Mar 71	124.3	104.2	147	-40.4	-26.4	964
30–31 Mar 71	118.0	101.2	398	-76.1	-76.6	1008
27–28 Apr 71	113.1	102.1	302	-99.9	-75.9	1024
27–28 May 71	112.0	102.4	88	-49.5	-23.8	916
18–19 Jun 71	112.7	94.4	82	-108.7	-66.2	938
14–16 Jul 71	113.5	114.7	244	-127.0	-95.6	1018
20–21 Jul 71	115.7	.26.8	463	-51.5	-4.4	992
28–29 Jul 71	115.9	117.5	84	-108.2	-87.5	1057
19–20 Aug 71	112.9	123.4	70	-23.2	2.3	984
07–08 Sep 71	108.9	106.7	313	-29.6	-37.8	994
10–11 Sep 71	108.6	95.0	162	9.1	-34.3	993
02–03 Nov 71	110.2	111.4	77	46.4	59.6	973
25–26 Jan 72	115.2	118.9	299	67.1	38.8	925
26–27 Jan 72	115.2	118.9	353	2.5	1.2	929
23–24 Feb 72	127.4	180.4	400	-16.3	-52.4	1031
09–10 Mar 72	126.3	132.5	108	32.5	23.2	975
23–24 Mar 72	127.1	126.4	418	-7.1	-85.9	1149
26–27 Apr 72	126.0	109.9	110	-34.5	8.9	969
09–10 May 72	119.6	133.3	357	-42.0	-50.5	1070
25–26 May 72	124.5	127.3	127	-190.0	-118.0	963
30–31 May 72	122.4	116.8	309	-108.4	-96.3	985
08–09 Jun 72	126.5	149.1	217	-77.1	-74.5	1076

Day	$\overline{F}_{10.7}$	$F_{10.7}$	$\overline{AE}$	$\overline{V}$	$\overline{U}$	$\overline{T}_\infty$
13–14 Jun 72	127.3	.38.9	173	−118.9	−49.6	1023
28–29 Jun 72	128.6	127.3	231	−87.5	−51.9	1079
30Jun–1Jul 72	128.6	127.3	95	−57.3	−26.1	994
26–27 Jul 72	132.2	120.6	248	−79.5	−65.6	1050
07–08 Aug 72	128.9	125.8	117	−24.3	−10.3	1064
06–07 Sep 72	127.3	119.2	107	−38.2	−24.5	1017
12–13 Sep 72	127.0	100.6	137	−20.7	−44.5	947
03–04 Oct 72	121.2	108.4	145	−1.9	−33.4	988
15–16 Nov 72	113.1	86.5	447	−13.1	24.6	901
06–07 Dec 72	109.1	77.8	94	29.7	40.8	915
02–03 Jan 73	98.4	105.1	31	38.6	38.8	840
16–17 Jan 73	100.3	93.8	122	53.0	70.5	896
13–14 Feb 73	99.1	104.7	78	6.9	9.0	854
24–25 Apr 73	101.4	109.0	309	38.3	0.6	1015
22–23 May 73	99.7	99.6	356	−66.3	−108.3	994
07–08 Aug 73	93.0	87.5	262	−39.6	−44.3	956
14–15 Aug 73	93.0	72.6	132	−40.2	−42.7	865
19–20 Sep 73	92.8	92.0	322	21.2	17.6	906
16–17 Oct 73	89.9	75.6	497	15.0	−49.2	895
13–14 Nov 73	82.8	73.8	175	41.9	15.1	911
14–15 Nov 73	82.3	73.8	145	32.7	36.6	885
12–13 Feb 74	79.9	77.5	326	83.3	52.7	896
13–14 Feb 74	79.9	77.5	333	58.5	33.3	860
03–04 Apr 74	86.9	71.6	634	−10.9	17.3	1048
16–17 Apr 74	85.9	115.0	119	2.7	−15.0	961

Day	$\overline{F}_{10.7}$	$F_{10.7}$	$\overline{AE}$	$\overline{V}$	$\overline{U}$	$\overline{T}_\infty$
02–03 Oct 74	91.4	93.4	348	20.7	−52.8	936
12–13 Mar 75	71.8	75.6	31+	90.2	27.1	936
13–14 Mar 75	71.8	75.6	31+	−6.2	53.5	928
27–28 Jun 75	74.4	81.5	9+	−37.4	−21.3	874
12–13 Jul 75	81.5	82.6	11	−66.9	−71.4	905
13–14 Jul 75	81.5	82.6	17+	−47.5	−44.5	897
25–27 Jul 75	81.5	80.0	27+	−57.2	−72.2	916
23–24 Aug 75	76.7	84.2	12	6.1	−26.6	847
17–19 Sep 75	88.8	76.2	21	−19.4	−54.1	872
01–02 Oct 75	75.6	79.9	5	25.8	17.8	861
12–14 Nov 75	76.4	78.1	12+	40.3	40.2	918

110
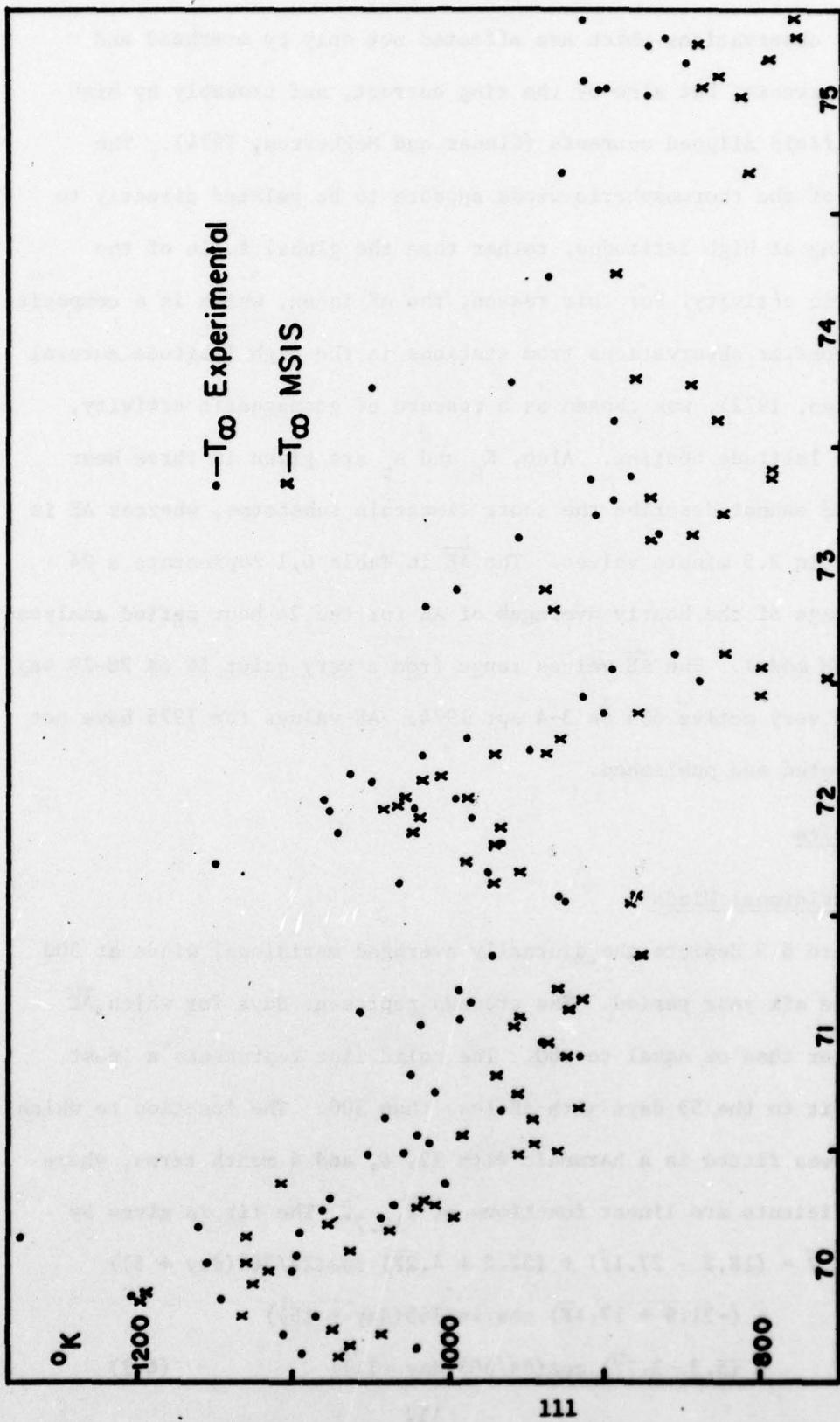
Figure 6.2 Comparison of diurnally averaged T_∞ from Millstone data and the MSIS model for the days analyzed in the present work.

netometer observations which are affected not only by overhead and auroral currents, but also by the ring current, and probably by high latitude field aligned currents (Clauer and McPherron, 1974). The response of the thermospheric winds appears to be related directly to the heating at high latitudes, rather than the global scale of the geomagnetic activity. For this reason, the AE index, which is a composit of magnetometer observations from stations in the high latitude auroral zone (Allen, 1972), was chosen as a measure of geomagnetic activity, i.e. high latitude heating. Also, K_p and A_p are given in three hour values and cannot describe the short timescale substorms, whereas AE is available in 2.5 minute values. The $\overline{AE}$ in Table 6.1 represents a 24 hour average of the hourly averages of AE for the 24 hour period analyzed by the EMH model. The $\overline{AE}$ values range from a very quiet 56 on 28-29 Sep 1970 to a very active 634 on 3-4 Apr 1974. AE values for 1975 have not been computed and published.

6.2 Results

6.2.1 Meridional Winds

Figure 6.3 depicts the diurnally averaged meridional winds at 300 km for the six year period. The crosses represent days for which $\overline{AE}$ was greater than or equal to 300. The solid line represents a least squares fit to the 53 days with $\overline{AE}$ less than 300. The function to which the data was fitted is a harmonic with 12, 6, and 4 month terms, where the coefficients are linear functions of $\overline{F}_{10.7}$. The fit is given by

$$\overline{V} = (18.2 - 27.1\overline{F}) + (52.2 + 4.2\overline{F}) \cos(2\pi/365(\text{day} + 5))$$
$$+ (-31.9 + 17.4\overline{F}) \cos(4\pi/365(\text{day} + 15))$$
$$+ (5.3 - 3.7\overline{F}) \cos(6\pi/365(\text{day} - 11)) \tag{6.1}$$

112
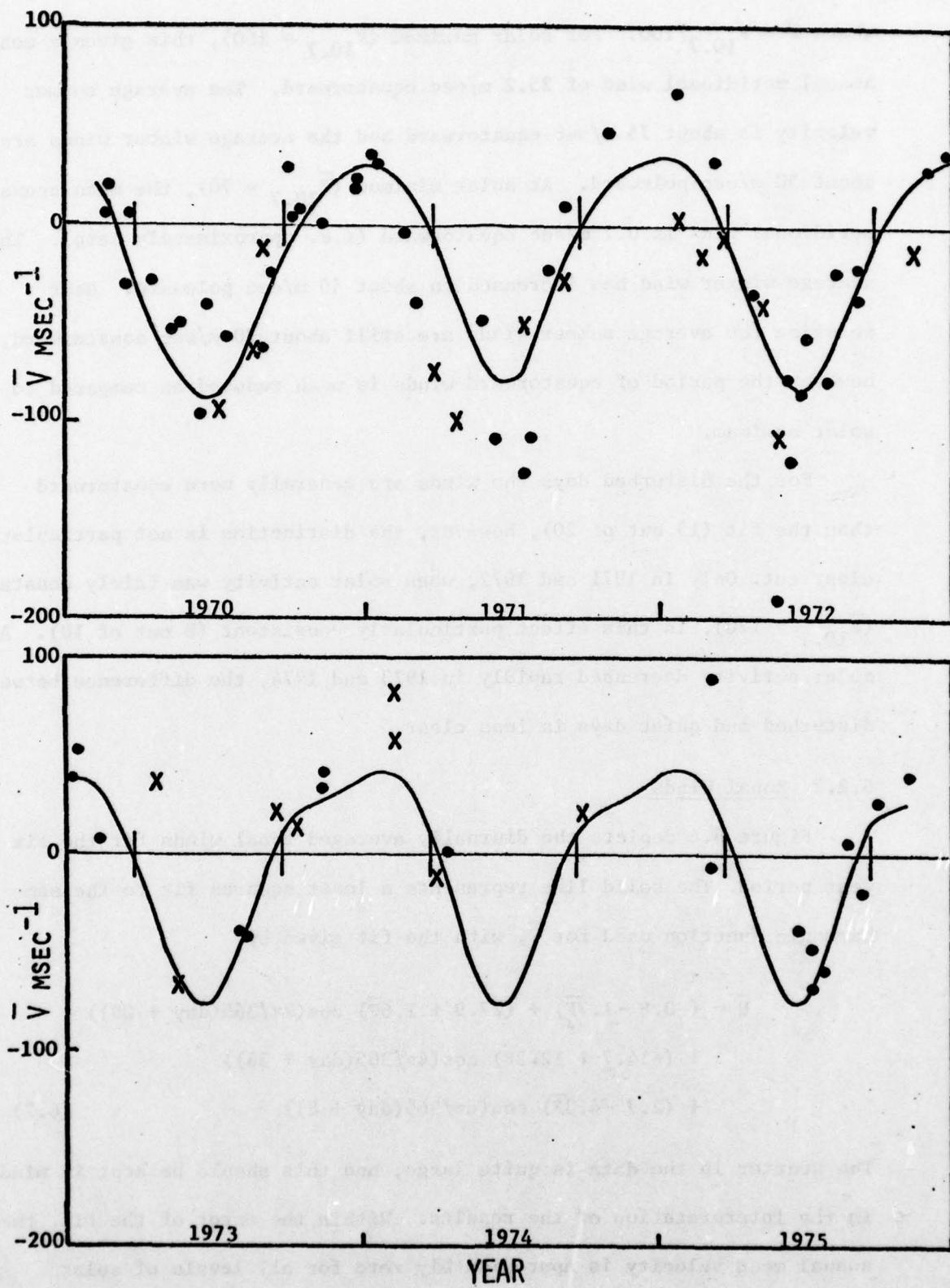
Figure 6.3 Diurnally averaged meridional velocity from the EMH model. The solid line represents a fit to the data described in the text.

113

where $\overline{F} = \overline{F}_{10.7}/100$. For solar maximum ($\overline{F}_{10.7} = 160$), this gives a mean annual meridional wind of 25.2 m/sec equatorward. The average summer velocity is about 75 m/sec equatorward and the average winter winds are about 30 m/sec poleward. At solar minimum ($\overline{F}_{10.7} = 70$), the mean annual meridional wind is 0.7 m/sec equatorward (i.e. approximately zero). The average winter wind has increased to about 40 m/sec poleward. Near solstice the average summer winds are still about 70 m/sec equatorward, however the period of equatorward winds is much reduced as compared to solar maximum.

For the disturbed days the winds are generally more equatorward than the fit (13 out of 20), however, the distinction is not particularly clear cut. Only in 1971 and 1972, when solar activity was fairly constant ($\overline{F}_{10.7} \simeq 120$), is this effect particularly consistent (8 out of 10). As solar activity decreased rapidly in 1973 and 1974, the difference between disturbed and quiet days is less clear.

6.2.2 Zonal Winds

Figure 6.4 depicts the diurnally averaged zonal winds for the six year period. The solid line represents a least squares fit to the same harmonic function used for $\overline{V}$, with the fit given by

$$\overline{U} = (-0.8 - 1.7\overline{F}) + (27.9 + 1.6\overline{F})\cos(2\pi/365(day + 29))$$
$$+ (-14.7 + 12.3\overline{F})\cos(4\pi/365(day + 36))$$
$$+ (2.7 - 4.3\overline{F})\cos(6\pi/365(day + 8)) \qquad (6.2)$$

The scatter in the data is quite large, and this should be kept in mind in the interpretation of the results. Within the error of the fit, the annual mean velocity is approximately zero for all levels of solar

114
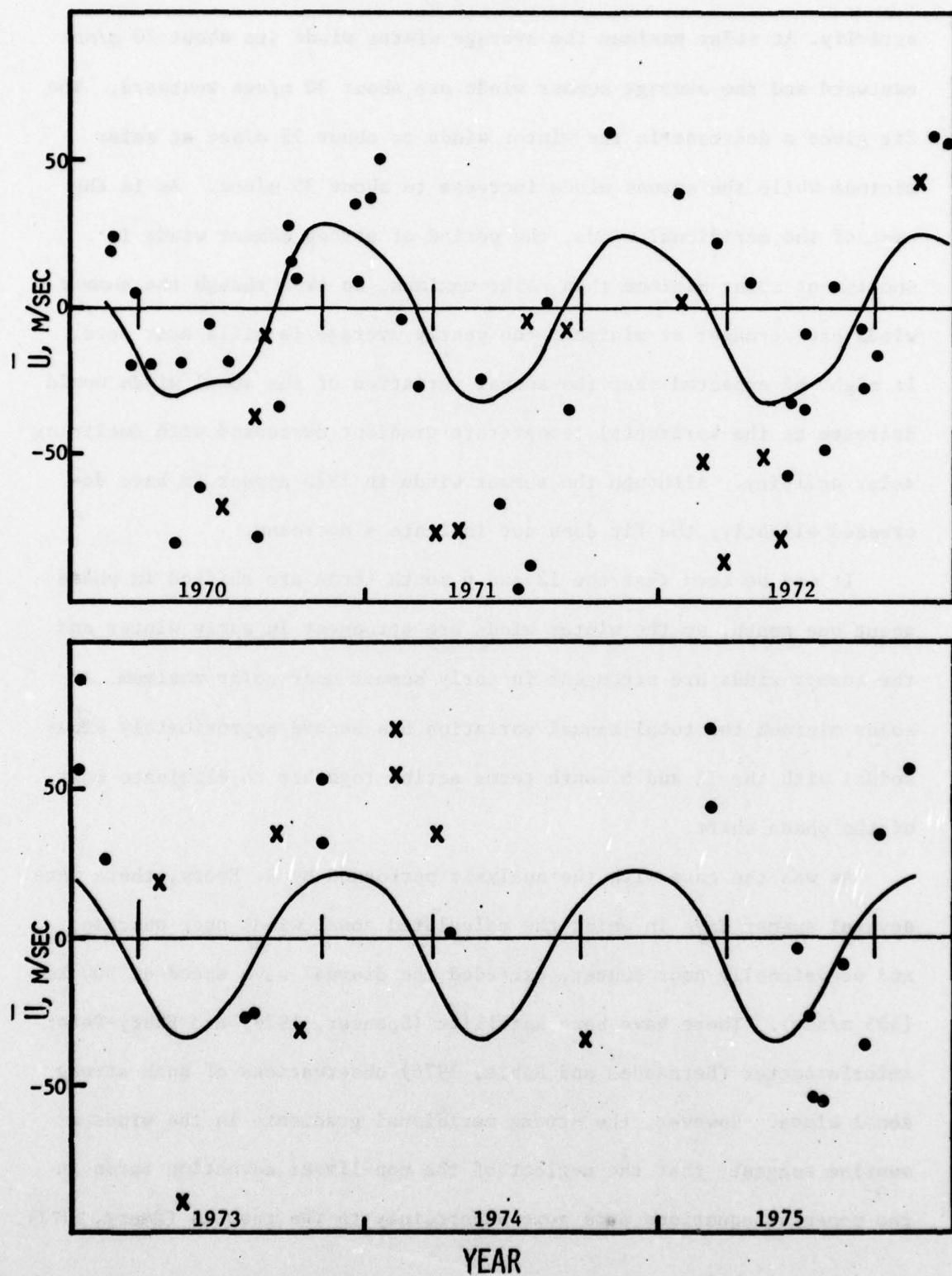
Figure 6.4   Same as Figure 6.3 except for diurnally averaged zonal velocities.

115

activity. At solar maximum the average winter winds are about 30 m/sec eastward and the average summer winds are about 30 m/sec westward. The fit gives a decrease in the winter winds to about 25 m/sec at solar minimum while the summer winds increase to about 35 m/sec. As in the case of the meridional winds, the period of strong summer winds is shorter at solar minimum than solar maximum, so even though the summer winds are stronger at minimum, the yearly average is still near zero. It might be expected that the annual variation of the zonal winds would decrease as the horizontal temerature gradient decreased with declining solar activity. Although the summer winds in 1975 appear to have decreased slightly, the fit does not indicate a decrease.

It may be seen that the 12 and 6 month terms are shifted in phase about one month, so the winter winds are strongest in early winter and the summer winds are strongest in early summer near solar maximum. At solar minimum the total annual variation has become approximately sinusoidal with the 12 and 6 month terms acting together to eliminate most of the phase shift.

As was the case with the analysis performed by B. Emery, there were several summer days in which the calculated zonal winds near sunrise, and occasionally near sunset, exceeded the diurnal wave speed at 300 km (355 m/sec). There have been satellite (Spencer, 1977) and Fabry-Perot interferometer (Hernandez and Roble, 1976) observations of such strong zonal winds. However, the strong meridional gradients in the winds at sunrise suggest that the neglect of the non-linear advection terms in the momentum equations adds some uncertainty to the results (Emery, 1977).

The disturbed days generally have a more westward average wind than the fit (14 out of 20). As with the meridional wind, this effect is most evident in 1971 and 1972, and is less consistent in later years.

6.2.3 High Latitude Heating Modulation

As mentioned in the previous sections, there appears to be a definite effect on both the meridional and zonal averaged winds during geomagnetically disturbed periods. Emery compared the difference between a simple harmonic fit and the diurnally averaged meridional wind with the magnetic index A_p and found an apparent, but not convincing, relation for $A_p < 10$ with the averaged winds becoming more equatorward as A_p increased. To further test this modulating effect, the difference between the averaged values and the harmonic fit for the six year period has been compared with $\overline{AE}$.

Figure 6.5 shows the scatter diagram for the meridional winds. The straight line is a least squares fit to the data which went into the harmonic fit (i.e. excluding the disturbed days). Although the straight line fit suggests an increased equatorward wind with increasing $\overline{AE}$, the correlation is not sifnificant. Within the 95% confidence limits, the complete data set really has no definite trend, so no clear conclusion can be made from this sample of winds. Figure 6 6 shows the comparison for the averaged zonal winds. Within the 95% confidence limits, no trend can be claimed. The 68% confidence limits do support a trend, with the winds becoming more westward as $\overline{AE}$ increases. However, the certainty of such a conclusion is not strong. If the disturbed days are included in the straight line fit, there is little difference in the result; however, it is clear that the disturbed days are not a direct extension of the quiettime results.

117
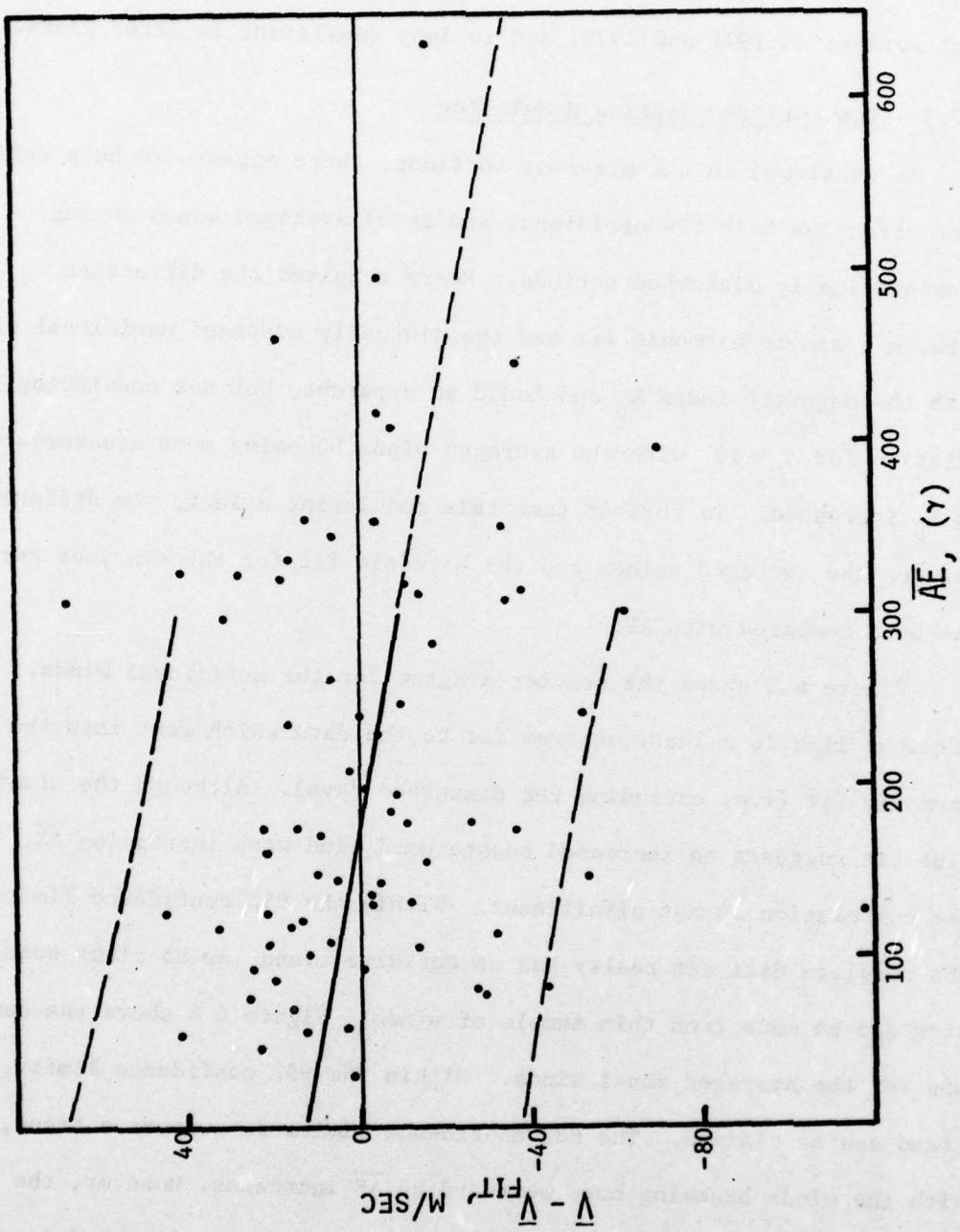
Figure 6.5 Difference between computed diurnally averaged meridional wind and the fitted value as a function of $\overline{AE}$. The dashed line is the 95% confidence level.

118
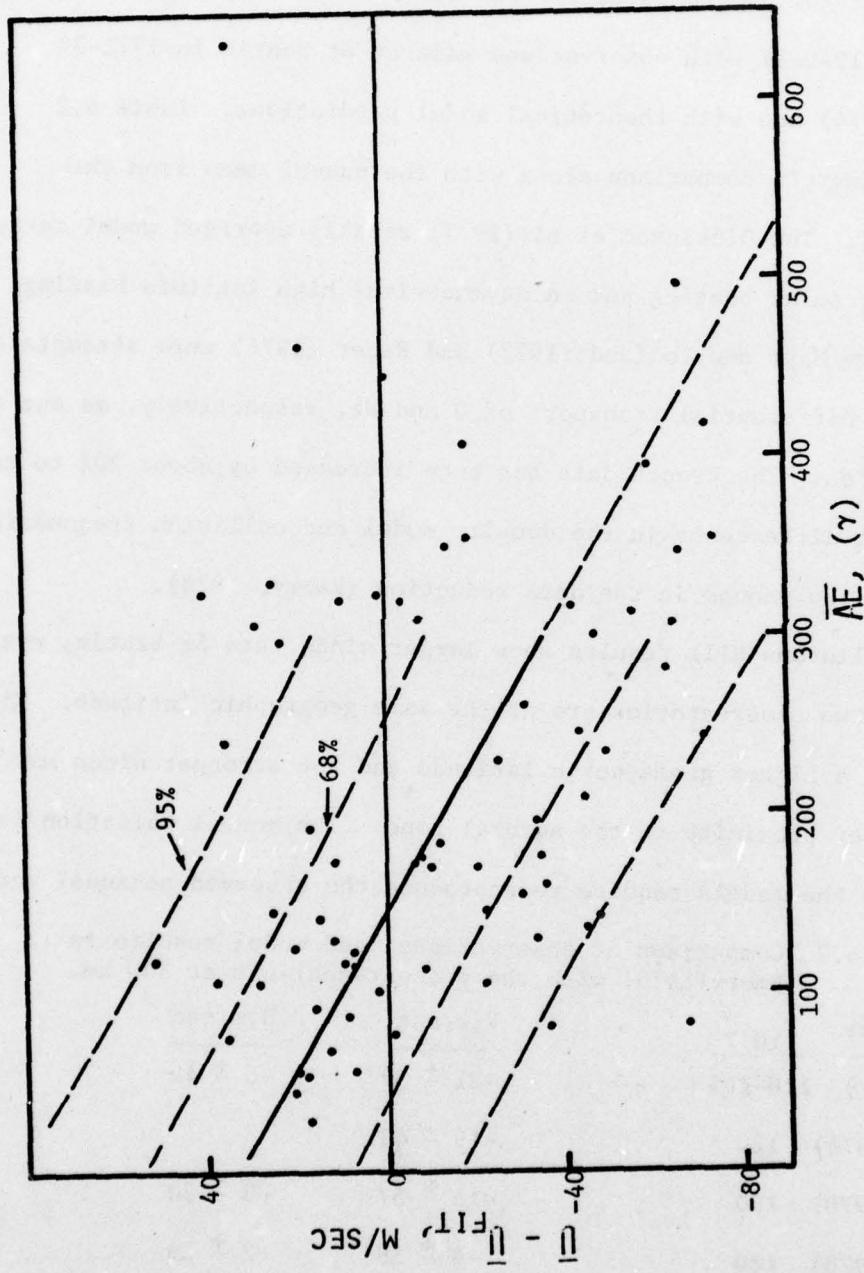
Figure 6.6 Same as Figure 6.5 except for diurnally averaged zonal winds. The dashed
lines represent the 95% and 68% confidence levels.

6.3 Comparison with Other Results

6.3.1 Observations

Emery (1978) has compared the results for the moderate solar activity period 1970-71 with observations made at St Santin in 1971-72 (Amayenc, 1974) and with theoretical model predictions. Table 6.2 summarizes Emery's comparison along with the annual mean from the present work. The Dickinson et al (1977) zonally averaged model takes into account solar heating and an asymmetrical high latitude heating. The models by Mayr and Volland (1972) and Reber (1976) were attempts to explain the differential transport of O and He, respectively, as due to wind diffusion. The French data has been increased by about 20% to take into account differences in the density model and collision frequencies used by the two groups in the data reduction (Emery, 1978).

The Millstone Hill results show larger winds than St Santin, even though the two observatories are at the same geographic latitude. Millstone is at a higher geomagnetic latitude and the stronger winds may be due to the closer proximity to the auroral zone. The annual variation is larger than values the models require to reproduce the observed seasonal variations.

Table 6.2 Comparison of observational and model results in Emery(1978) with the present analysis at 300 km.

Observations	$F_{10.7}$	V,m/sec	U,m/sec
Emery (1977)	110-165	-21 ± 52	-5 ± 42
Amayenc (1974)	120	-19 ± 42	
Babcock (1978)	120	-15 ± 57	-3 ± 30
Babcock (1978)	120	-6 ± 56	-2 ± 29
Theory			
Mayr and Volland (1972)		0 ± 15.5	0 ± 4.5
Reber (1976)		7 ± 34	
Dickinson et al (1977)		-35 ± 65	0 ± 42

120

The important conclusion of these initial results is to support the model prediction of Dickinson et al, and other models, that the high latitude heat source is an important factor in determing the dynamics of the global thermospheric circulation. The models cannot reproduce the global wind or temperature patterns without the high latitude heating. The net equatorward flow seen at both Millstone and St Santin supports the presence of a reverse circulation cell in the high latitude winter as predicted by Dickinson et al (Figure 5.2). Figure 6.7 shows Emery's averaged meridional winds and the harmonic fit. The winds clearly follow the "summer/winter" pattern seen in the behavior of the iono-sphere over Millstone Hill (Evans, 1973), with an abrupt change occur-ring around equinox. For this period of moderate solar activity, Emery found the averaged equinox winds to be equatorward, again consistent with the prediction of Dickinson et al.

Using 6300$\overset{o}{A}$ airglow observations, Hernandez and Roble (1977) have made a series of wind and temperature measurements of the nighttime thermosphere near solar minimum from April 1975 through March 1976. Using a semi-empirical model which computes winds using MSIS pressure gradients, they found fair agreement between the model and the observed winds. However, they did find that the measured nighttime temperatures were about 100–150°K greater than the model for summer and equinox, and 50–75°K greater in winter. Table 6.3 compares the diurnally averaged values from their model calculations at 250 km with the values taken from the fit of the present analysis for $\overline{F}_{10.7}$ = 80. The diurnally averaged values from the EMH model are approximately 10% less at 250 km

121
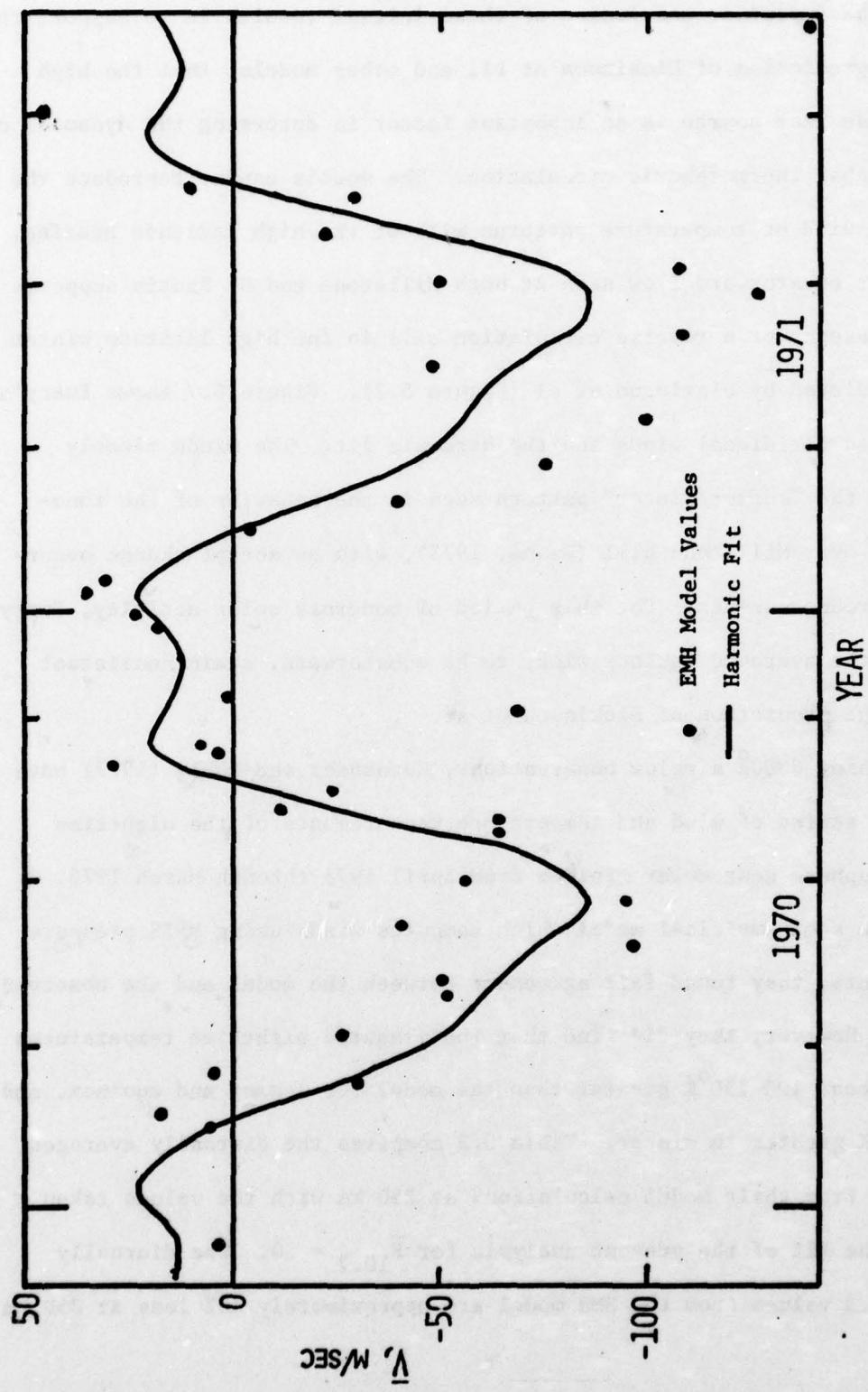
Figure 6.7 Harmonic fit to diurnally averaged meridional winds computed by Emery (1977).

than 300 km, and this adjustment has been made to the values in the table. For the six months in 1975 for which there were measurements at Millstone, the neutral temperature at 250 km was derived from the diurnally averaged value of T_∞ at Millstone using Equation 4.1. Also shown are the diurnally averaged values of temperature from the MSIS model for the particular days analyzed. Direct comparison with the results of Hernandez and Roble temperatures is not valid since they are averages of several days, but their results do support our observations that the MSIS temperatures are lower than observed.

Table 6.3 Comparison of results from Hernandez and Roble (1977) with the present analysis at 250 km when $\overline{F}_{10.7} = 80$.

	$\overline{U}$,m/sec		$\overline{V}$,m/sec		$\overline{T}_n$,°K		
	H&R	B	H&R	B	H&R	B	MSIS
Apr	-6.8	-25.1	-20.9	-17.7	853		
May	-25.1	-32.2	-43.3	-42.1	868		
Jun	-27.2	-32.2	-43.3	-65.1	851	835	780
Jul	-29.1	-21.7	-41.2	-64.7	849	865	795
Aug	-24.5	-1.9	-37.7	-17.1	850	810	764
Sep	-8.9	7.0	-22.2	3.3	861	834	806
Oct	1.5	12.1	-14.3	17.7	805	823	746
Nov	11.8	18.7	3.1	21.9	824	876	748
Dec	38.1	21.6	25.5	31.9	873		

Assuming their model results are representative of the diurnal winds, there is general agreement in the seasonal pattern for the zonal winds. However, for the meridional winds, the Millstone values are

123

larger, particularly in the summer, and the equinox value (September) is poleward rather than equatorward. The larger magnitude may partially be explained, as with the comparison with results from St Santin, as a geomagnetic latitude effect. Fritz Peak Observatory ($39.9°N,105.5°W$) is at a geomagnetic latitude of about $48°N$, about $9°$ further south than Millstone.

6.3.3. Models

Roble et al (1977) have extended their zonally averaged model to solar minimum conditions. The solar EUV and UV heating was reduced by a factor of two, and the high latitude heating was varied in order to produce winds similar to those reported by Hernandez and Roble (1977). For solar maximum, Dickinson et al used a height-intergrated mean global solar heating rate of 0.72 ergs $cm^{-2}sec^{-1}$. In order to reproduce winds derived from Millstone data, they required a Joule heating rate at equinox of 0.22 ergs $cm^{-2}sec^{-1}$. At solstice the auroral (Joule) heating rate was 0.38 ergs $cm^{-2}sec^{-1}$ and was partitioned with 2.5 times more heating in the summer hemisphere. For solar minimum, the mean global solar heating rate was 0.54 ergs $cm^{-2}sec^{-1}$ while the the Joule heating, at 0.09 ers $cm^{-2}sec^{-1}$, was 4.4 times smaller than at solar maximum. Most of the Joule heating was in the summer hemisphere. The global energy input due to Joule heating at solstice was 4.5×10^{17} ergs sec^{-1} at solar minimum versus 2×10^{18} ergs sec^{-1} at maximum.

The primary difference found at solar minimum is the absence of a reverse circulation cell in the high latitude winter. The meridional winds are directed from summer to winter pole at all altitudes and lati-

tudes. For the height and latitude of Fritz Peak observations, the model predicted summer and winter meridional winds of 50 msec^{-1} and 40 msec^{-1} versus the 45 msec^{-1} and 25 msec^{-1} derived form the measurements. At 45° latitude and 300 km, the calculated seasonal meridional winds are about 70 msec^{-1} and 45 msec^{-1}, which is in good agreement with the 70 msec^{-1} and 40 msec^{-1} of the Millstone results.

Roble et al found that the breakdown of the solstice circulation pattern occurred about two weeks before equinox when only solar heating and momentum forcing were included, i.e. low geomagnetic activity or solar cycle minimum. When high latitude heating is added the transition period begins only about one week before equinox.

Figures 6.8 and 6.9 depict the modulation in the mean meridional circulation for equinox and solstice as the level of high latitude heating varies from very quiet to substorm levels. The growth of the reverse circulation cell in the winter hemisphere can be seen to cause the winds to be come more equatorward, even reversing the flow for high activity. At equinox, the latitudinal distribution of the solar heating is essentially constant for the optically thin thermosphere. Therefore, fluctuations in the auroral heating, which are confined in latitude, are able to have a very pronounced effect.

6.4 Discussion

Although the density of data points decreases in the last two years of the analysis, the available data clearly follows the seasonal pattern established by the early years and predicted by the model of Dickinson et al. The mean annual meridional velocity goes to zero at solar minimum,

125
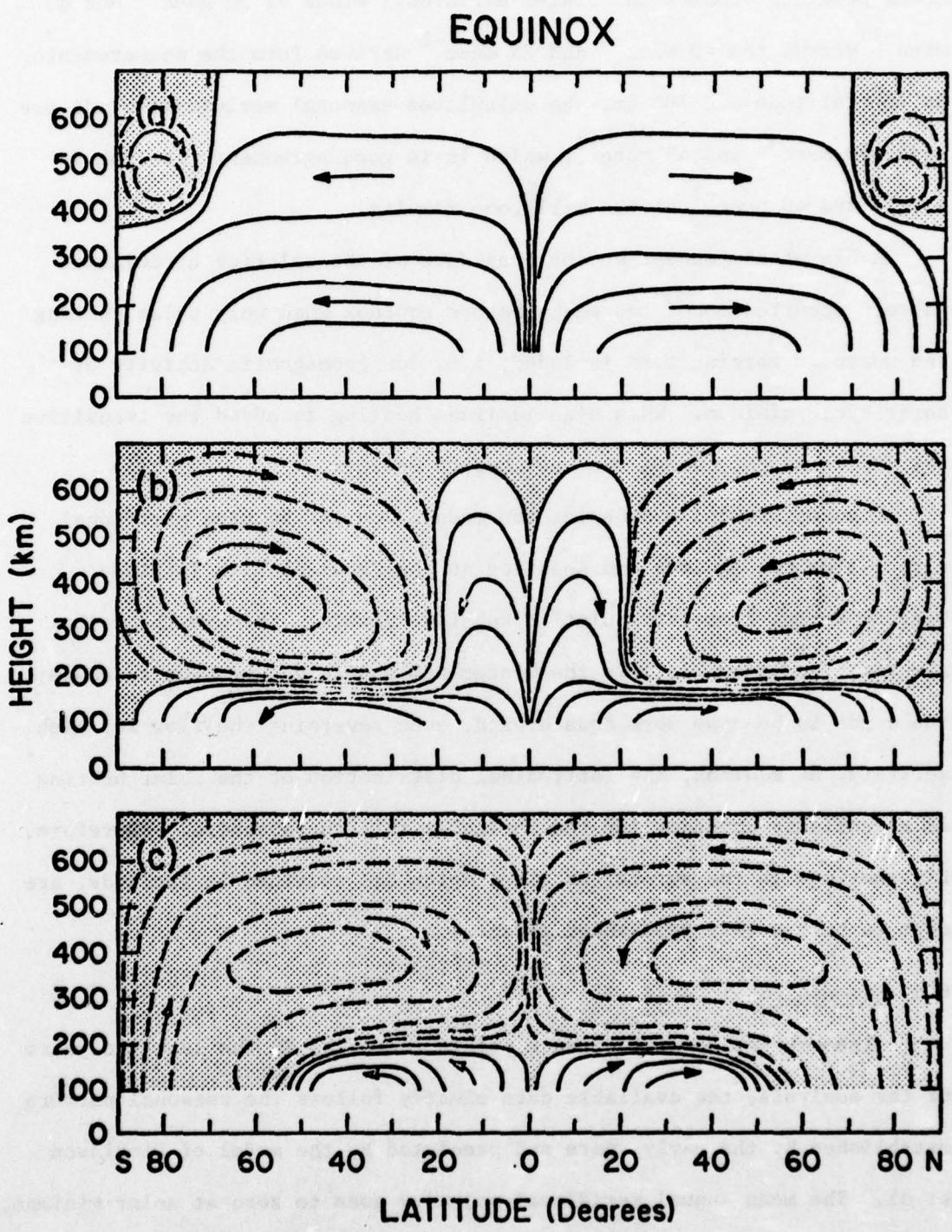
EQUINOX

Figure 6.8 Modulation of the global circulation pattern at equinox as auroral heating increases. (From Roble, 1977).

126
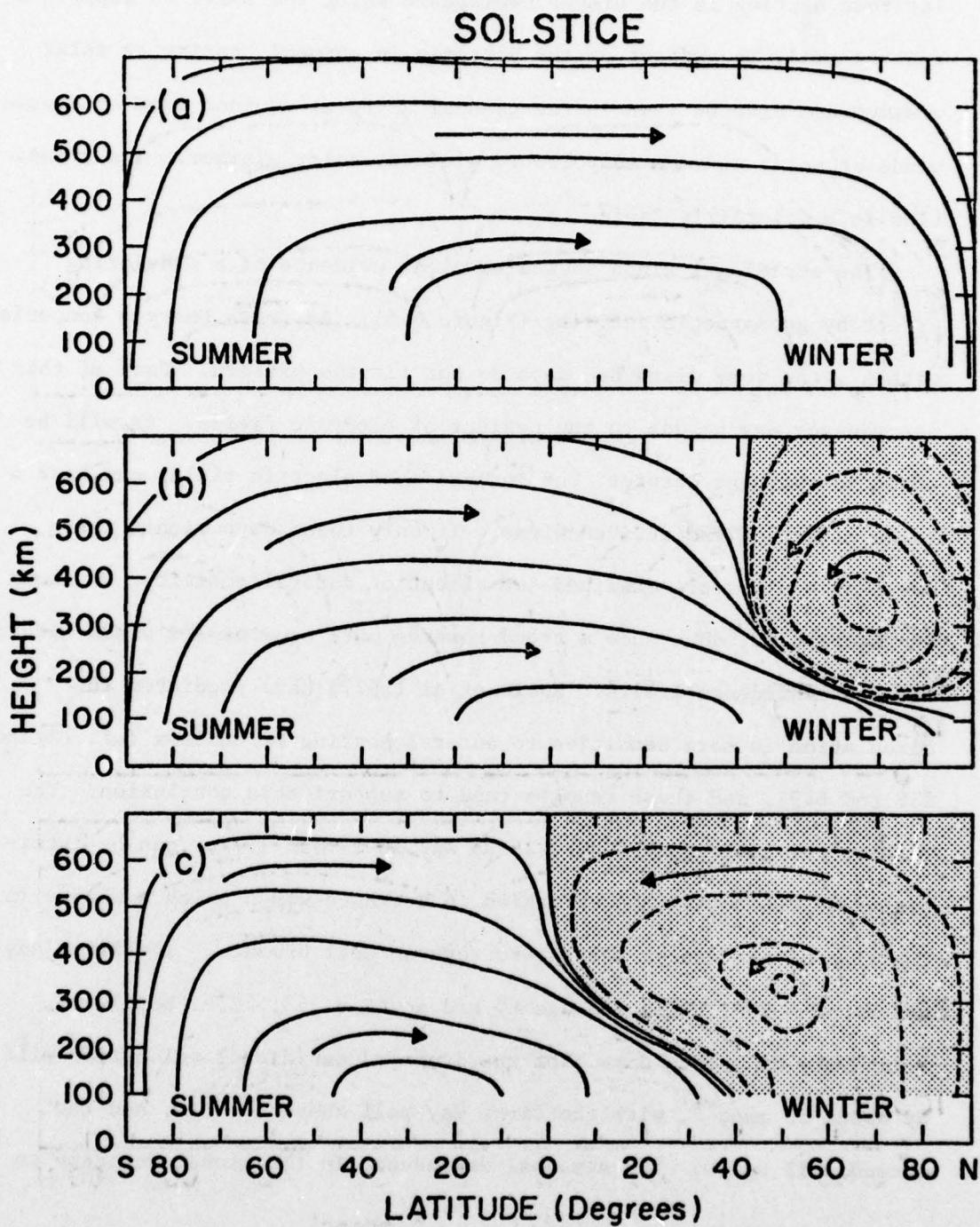
SOLSTICE

Figure 6.9   Same as Figure 6.8 except for solstice .

supporting the model prediction of Roble et al (1977) that the circulation during solstice will be one large summer-to-winter cell, with the high latitude heating in the winter hemisphere being too small to support a reverse cell. The effect of the decrease in auroral heating at solar minimum can also be seen in the gradual shift at equinox from equatorward winds at solar maximum to poleward winds at solar minimum. The transition is still fairly rapid.

The meridional winds showed no clear evidence of a modulating effect by geomagnetic activity (Figure 6.6). As with Emery's comparison with A_p, the very disturbed days do not fit the pattern. Part of this discrepancy may be due to the neglect of electric fields. As will be shown in the next chapter, the inclusion of electric fields can have a large effect on the derived winds. If only those days within three weeks of equinox are examined the effect of auroral activity, as shown in Figure 6.10, does show a trend towards more equatorward winds within the 95% confidence limits. Roble et al (1977) have predicted the circulation is more sensitive to auroral heating at equinox (cf. Figures 6.8 and 6.9), and these results tend to support this conclusion. The results for two January days, 25-26 and 26-27 Jan 1972, can be interpreted as reflecting the variation in averaged winds which a change in the size of the winter hemisphere reverse cell produce. The first day had an $\overline{AE}$ = 299, while the second had an $\overline{AE}$ = 353, i.e. both were relatively disturbed days. Yet the averaged meridional velocities differ by about 35 msec^{-1}, with the first day well above the fit, and the second well below. The seasonal dependence in the global response to

128
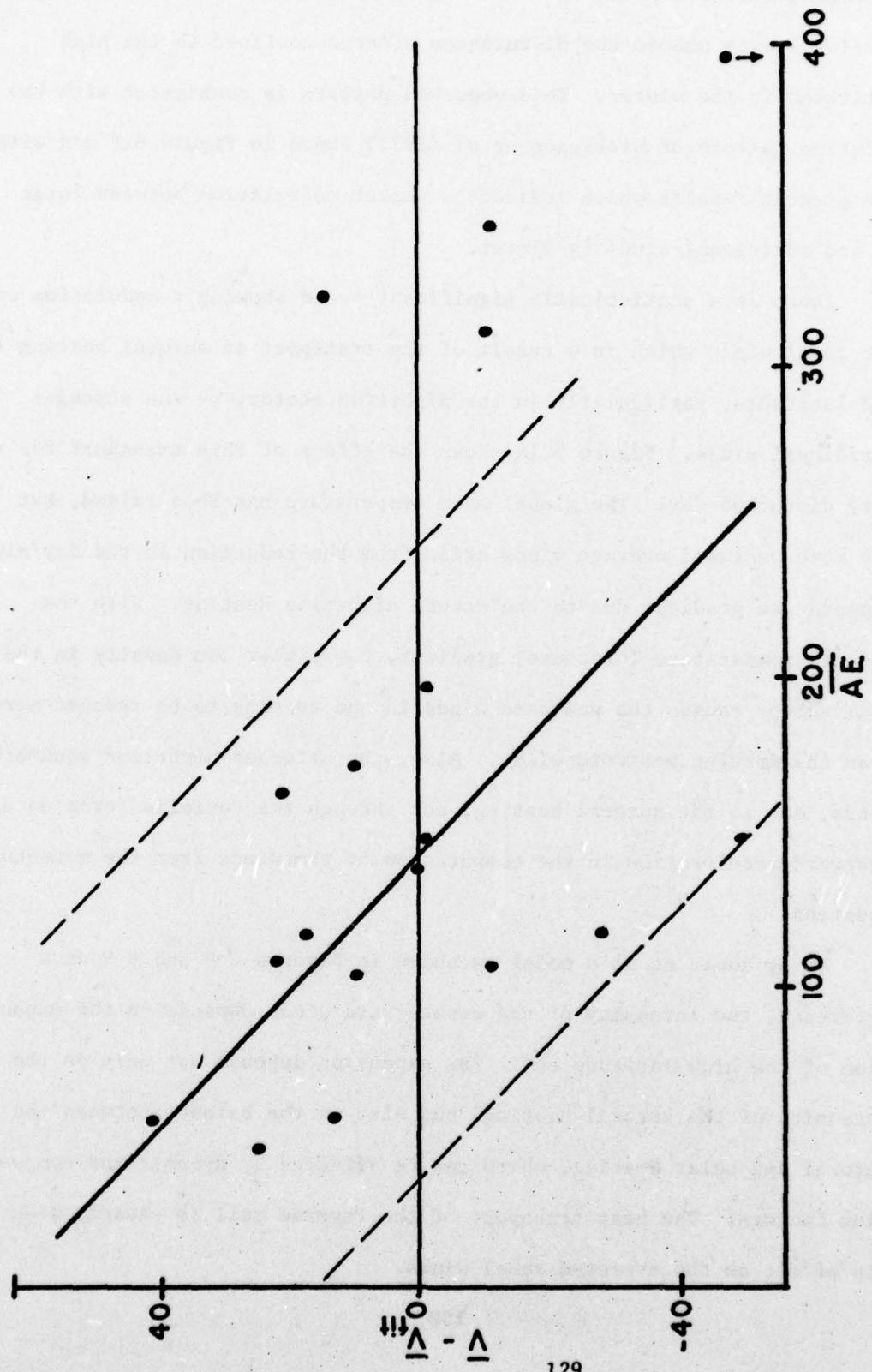
Figure 6.10 Same as Figure 6.6 except just for days within three weeks of equinox.

129

geomagnetic storms found by Prolss and von Zahn (1977) and others (ref. Section 2.4.1) showed the disturbance effects confined to the high latitudes in the winter. This observed pattern is consistent with the solstice pattern of Dickinson et al (1977) shown in Figure 6.9 and with the present results which indicate a weaker correlation between large $\overline{AE}$ and meridional winds in winter.

There is a statistically significant trend showing a modulation of the zonal winds which is a result of the transport of auroral heating to mid-latitudes, particularly in the nighttime sector, by the stronger meridional winds. Figure 5.1a shows the effect of this transport for a very disturbed day. The global mean temperature has been raised, but the more westward average winds arise from the reduction in the day/night temperature gradient due to the strong nighttime heating. With the reduced temperature (pressure) gradient, the higher ion density in the dusk sector causes the eastward winds in the evening to be reduced more than the morning westward winds. Also, the stronger nighttime equatorward winds, due to the auroral heating, act through the Coriolis force as a westward acceleration in the computation of the winds from the momentum equation.

Using Roble et al's model as shown in Figures 6 8 and 6 9 as a reference, the intensity of the equatorward winds depends on the expansion of the high latitude cell. The expansion depends not only on the intensity of the auroral heating, but also on the balance between the auroral and solar heating, which can be affected by dynamic and composition factors. The heat transport of the reverse cell is clearly seen in its effect on the averaged zonal winds.

130

This page purposely left blank

131
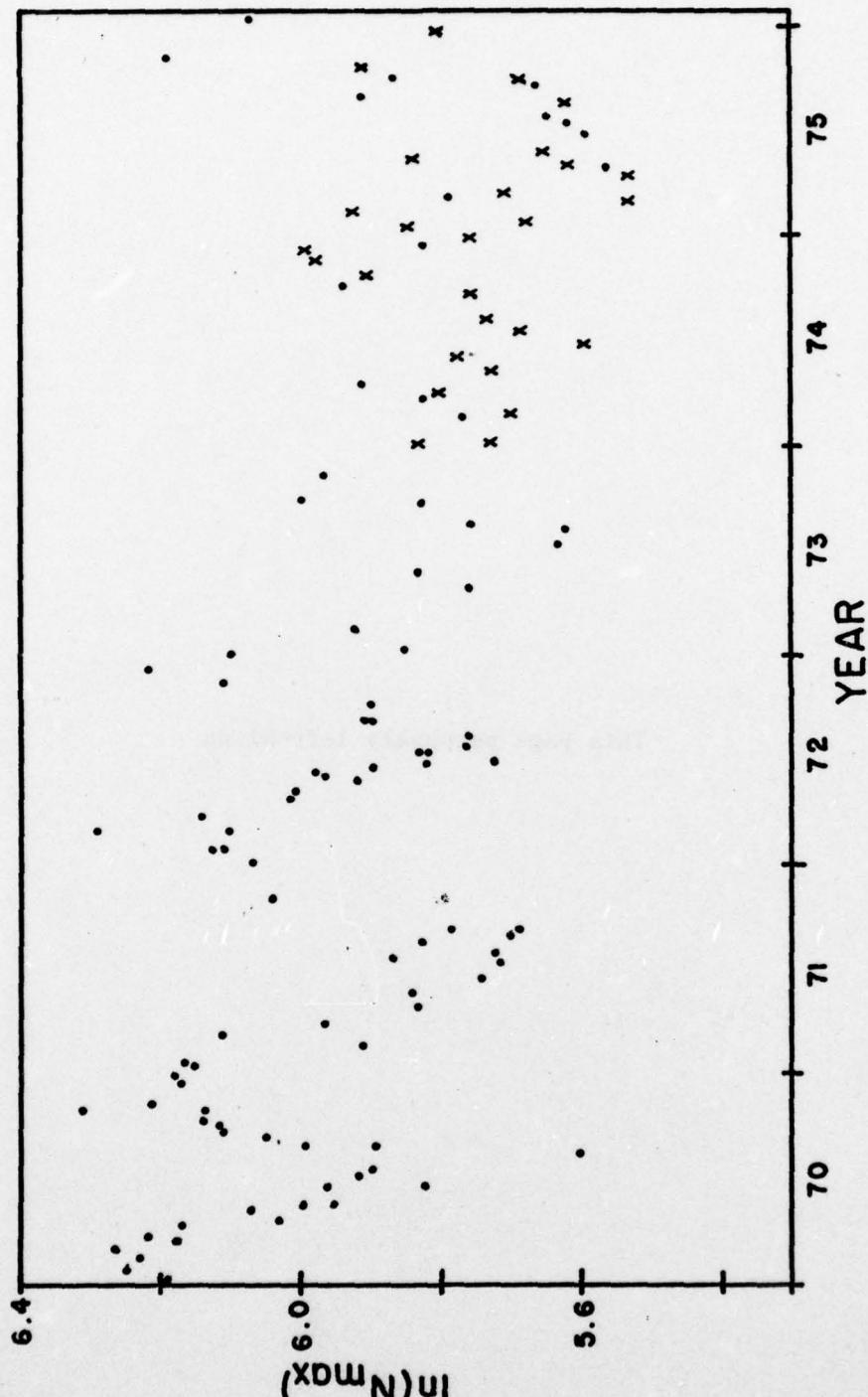
Figure 6.11 Log$_{10}$ of N F2 for 92 days when one-pulse data was taken at Millstone plus values derived from f$_o$F2 used during other Millstone experiments illustrating reduction of the seasonal variation.

132

One of the major points made in Emery's (1978) analysis is that the seasonal variation in the meridional winds is strong enough to produce the wind induced diffusion needed to create the oxygen anomaly(or helium bulge). Even though the net equatorward flow has become almost zero at solar minimum, the seasonal variation is still quite strong, with the summer winds slightly stronger than the winter winds. In Figure 6.11 the logarithm of the peal electron density, N_mF2, is plotted for the 92 days of one-pulse data (dots). For the data sparse period 1974-1975, N_mF2 has been derived from f_oF2 measurements used in other Millstone experiments (crosses). The seasonal variation is quite obvious in 1970 through 1972, but grows weaker from 1973 through 1975, with the points becoming widely scattered in 1975. This ionospheric data might suggest that the oxygen anomaly, which has been proposed to explain the N_mF2 seasonal variation, has also dissappeared. However, satellite data taken in 1974 at $F_{10.7} = 90$ by Maurersberger (1976) and von Zahn and Fricke (1978) still show a clear, although slightly diminished, oxygen bulge, with part of the reduction in the bulge explainable in the lower T_∞. Model calculations by Straus and Christopher (1978) at $F_{10.7} = 140$ and 92 showed that the winter enhancement of O below 200 km due to wind diffusion is not significantly dependent on $F_{10.7}$, which is consistent with the present results that the seasonal variation in the meridional wind does not change significantly with decreasing solar activity.

An explanation for this apparent contradiction depends upon the fact that the F2 peak is not just dependent on the local photochemistry, but is greatly effected by diffusive transport and wind dynamics, so the

133

variation of N_mF2 is not necessarily a good indicator of the photochemical ballance of the ionosphere. The ionospheric seasonal variation is actually dependent on the ratio of O/N_2 at the level of the F1 peak (about 160 km). The dissappearance of the seasonal variation in the F2 peak is related to the fact that with lower temperatures and scale heights, the F layer is formed lower in the atmosphere near sunspot minimum and at the level of the F1 peak the seasonal variation of O/N_2 due to transport appears to be approximately offset by the seasonal variation in the ionizing radiation flux due to the change in solar zenith angle.

7. VARIATIONS IN THE DIURNAL CIRCULATION PATTERN

Although the solar EUV and UV flux can vary significantly over a period of days (or even hours when there are large X-ray flares) the thermospheric response time is relatively slow. Hedin et al (1977) found that variations in temperature and density correlated best with the 3-month average, $\overline{F}_{10.7}$, with a smaller dependence on the daily $F_{10.7}$. It is presently thought that most of the variations, or "weather," in the thermosphere depend on fluctuations in the auroral heating associated with geomagnetic disturbances. Although the total heat input from this source usually remains small compared with the global EUV and UV flux, it is important because it is deposited over a small geographic area at high latitudes. It also appears that the mechnical forcing of the high latitude ion convection pattern (i.e. momentum transfer from the ions to the neutrals) can be important to the dynamics of the winds observed at lower latitudes. A third factor is the increased electric fields during high latitude disturbances which penetrate to lower latitudes, so that the ion drifts induced by the electric field drifts become an important part of the of the mid-latitude dynamics. This chapter examines the changes in the diurnal circulation pattern during geomagnetic disturbances and relates these changes to the different high latitude processes which occur during auroral storms.

All the data has been analyzed using the three modifications to the EMH model discussed in Chapter 5, viz: i) experimental values of T_∞ were used to compute neutral densities needed in the $V_{D//}$ caluculations, ii) corrections for frictional heating due to neutral winds were included in

the derivation of T_{∞}, and iii) effects of electric field-induced ion drifts were included in all computations. For the sample of disturbed days in the 1970 through 1975 period, the averaged model electric field presented in Chapter 5 was used. For two of the more recent days of observations, coincident electric field measurements were available.

7.1 Results

7.1.1 Disturbance Signatures in the Ionospheric Data

The effects of auroral disturbances can be seen immediately in the ionospheric data obtained by the Millstone ISR. Figures 7.1 through 7.4 compare contour plots of the four ionospheric parameters measured by the radar for a quiet and disturbed equinox day.

As shown in Figure 7.1(a), a "typical" electron density pattern has a peak density in the afternoon. After sunset, the E and F1 regions quickly decay. In the F layer downward diffusion of ionization from above the peak tends to maintain a distribution in the topside ionosphere that decays with a constant shape. The generally equatorward meridional winds act to lift the layer to heights where the recombination rate is slow, thereby preserving the layer for much of the night. As can be seen in Figure 7.1, the height of the peak density is higher at night than during the day. At sunrise the rapid onset of ion production at all altitudes makes the ionosphere appear to expand both upward and downward from the peak. Comparing the quiet day with the disturbed day in Figure 7.1(b), the most obvious difference is the strong lifting of the h_mF2 near midnight. This will be shown to be caused by an equatorward surge in the winds. After the surge, the downward diffusion of

136
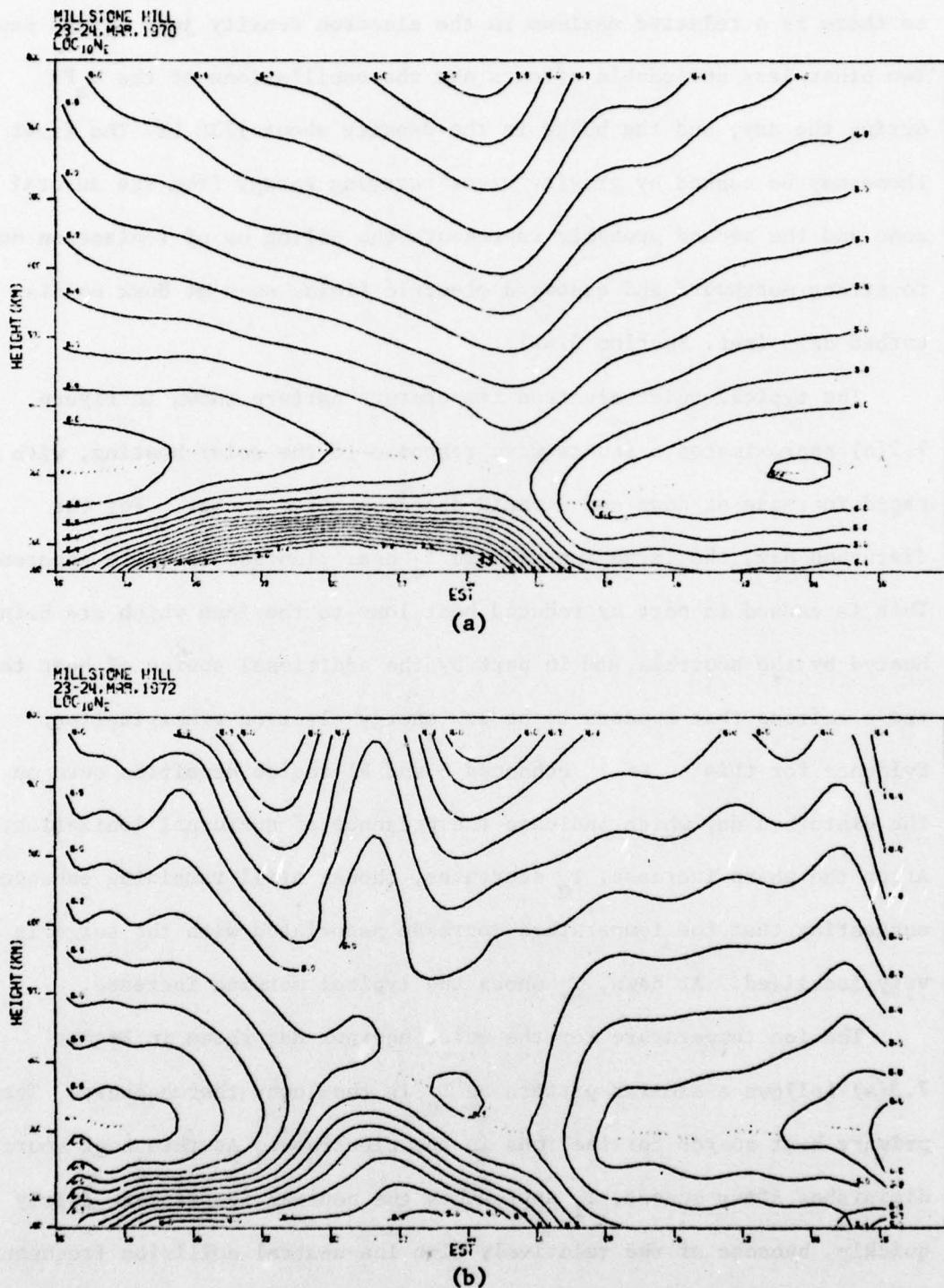
Figure 7.1 Comparison of electron density profiles for a (a) quiet day
23-24 Mar 1970 and a (b) disturbed day 23-24 Mar 1972.

137

this lifted ionization   acts as a source to the F2 peak,
so there is a relative maximum in the electron density just before dawn.
Two other less noticeable effects are the oscillations of the h_mF2
during the day, and the bulge in the density about 1730 LT. The first of
these may be caused by gravity waves carrying energy from the auroral
zone and the second probably represents the piling up of ionization due
to strong northward and eastward electric fields seen at dusk on dis-
turbed days (ref. Section 2.4.1).

The typical quiet electron temperature pattern shown in Figure
7.2(a) approximates a square wave response to the solar heating, with a
rapid increase at dawn and a rapid decrease after sunset. For the
disturbed day, the large increase in T_e near midnight is quite apparent.
This is caused in part by reduced heat loss to the ions which are being
heated by the neutrals, and in part by the additional source of heat to
the electrons that appears to be low energy electron precipitation.
Evidence for this   is   enhanced E and F1-region densities seen on
the disturbed day which indicate the presence of nocturnal ionization.
After the sharp increase, T_e decreases, though still remaining enhanced,
suggesting that the temperature increase associated with the surge is
very localized. At dawn, T_e shows the typical morning increase.

The ion temperature for the quiet equinox day shown in Figure
7.3(a) follows a similar pattern as T_e in the lower thermosphere. The
primary heat source for the ions is the electrons. As this heat source
diminishes after sunset, T_i approaches the neutral temperature fairly
quickly, because of the relatively high ion-neutral collision frequency.

138

MILLSTONE HILL
23-24,MAR.,1970
T_E

(a)

MILLSTONE HILL
23-24,MAR.,1972
T_E
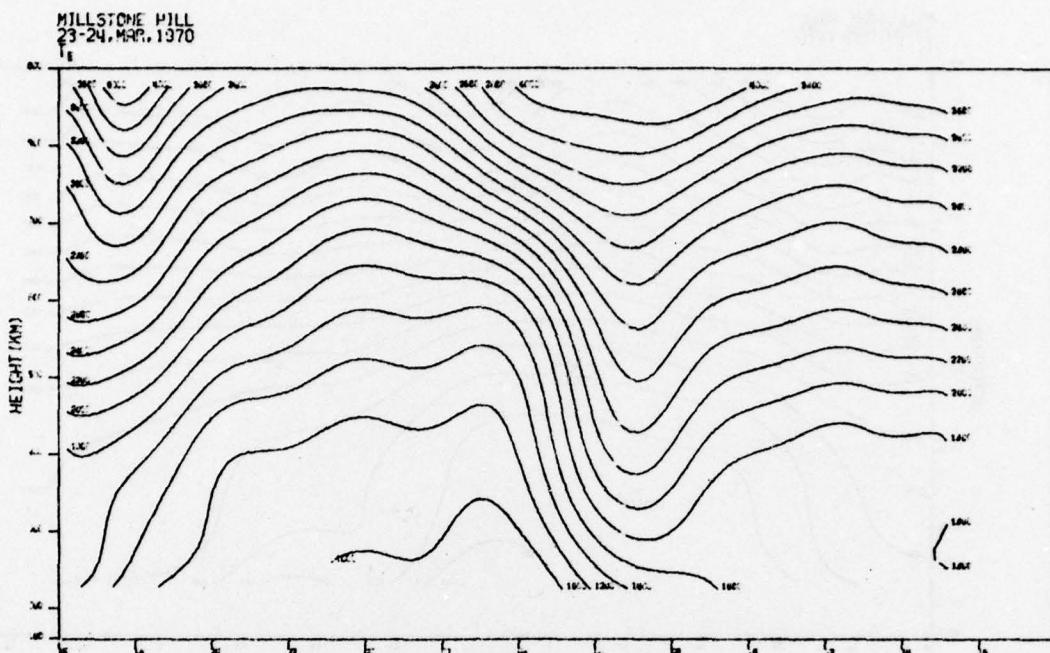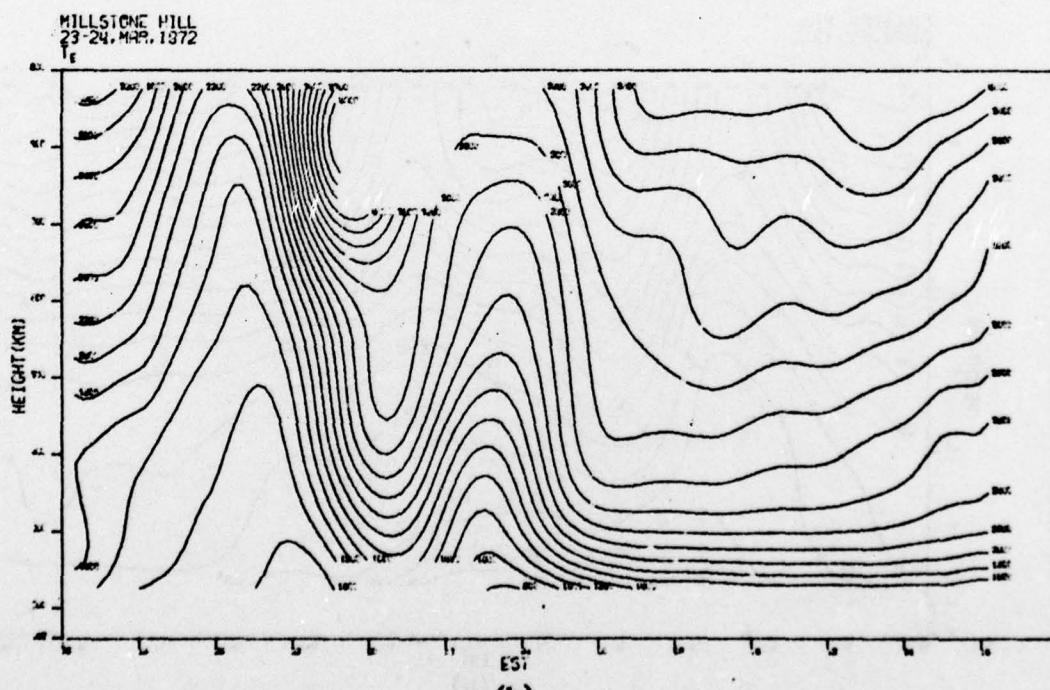
(b)

Figure 7.2   Same as Figure 7.1 except for electron temperature.

139
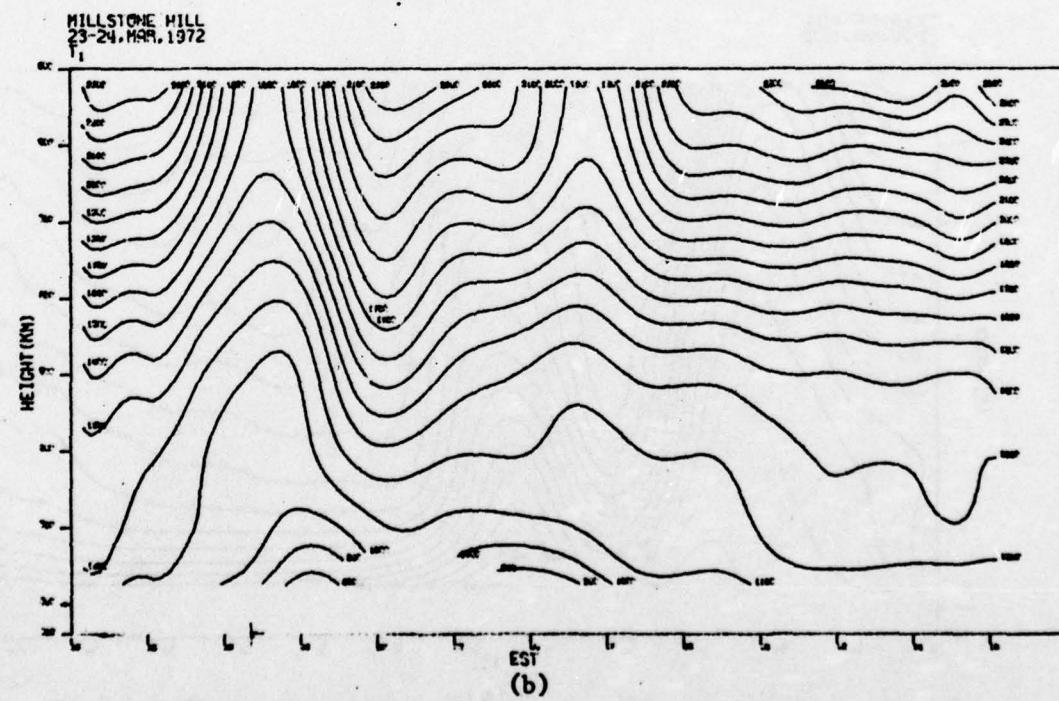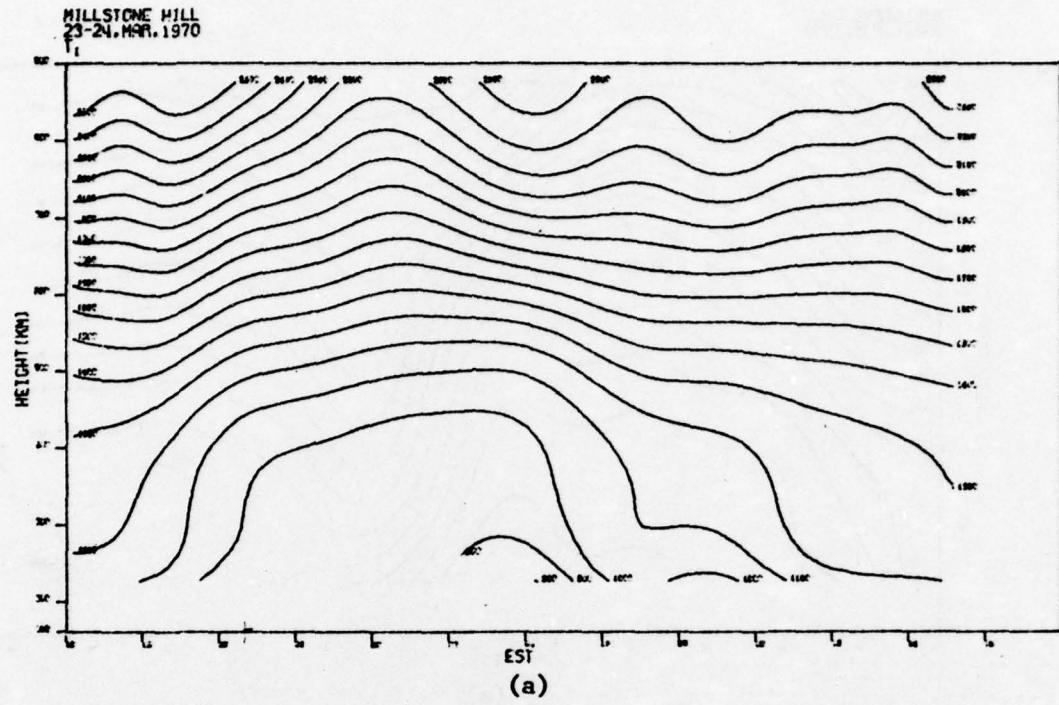
Figure 7.3 Same as Figure 7.1 except for ion temperature.

140

For the disturbed day in Figure 7.3(b), there is a rapid increase in T_i near midnight, with the temperature remaining enhanced most of the night. Frictional heating by the neutral air and heat transfer from the electrons are the responsible agents.

Figure 7.4(a) depicts the vertical ion drift for the quiet day. Large upward velocities are evident near dawn when the layer is growing and the reverse is seen at sunset. The nighttime drifts show a broad period of gradual downward velocities. Even though the equatorward winds act to drive the ions up the field lines, the larger diffusion velocity results in a net downward ion velocity. This net downward velocity persists through the day at mid and lower thermospheric heights where production exceeds loss. On the disturbed day, the dramatic lifting of the h_mF2 is evident in the large upward ion drifts at midnight. After this event the drifts become negative again, indicating the downward diffusion of the lifted ionization. The two other disturbance effects noted in the behavior of the elctron density can also be seen in V_{iz}. After sunrise and near sunset small waves in the vertical ion drifts seen at the lowest altitudes are probably a manifestation of gravity waves. The sharp increase in the V_{iz} at about 1730 LT is probably the effect of enhanced eastward electric field at dusk, which acts to lift the ions.

7.1.2 Neutral Winds

The meridional winds computed for the disturbed days show the most striking evidence of auroral disturbances. Figure 7.5 depicts the diurnal meridional wind pattern for seven winter and equinox days for which $\overline{AE}$ was greater than 300. (The Sep 1975 day had a $\Sigma K_p = 24$.) Large

141

MILLSTONE HILL
23-24. MAR. 1970
V_z

(a)

MILLSTONE HILL
23-24. MAR. 1972
V_z

(b)
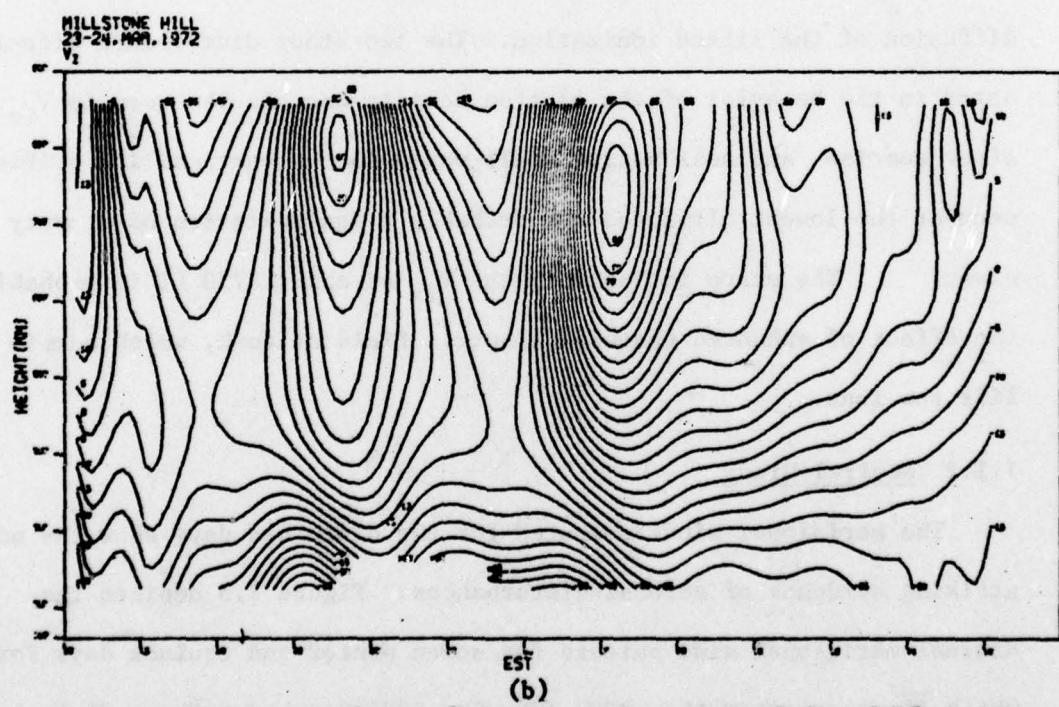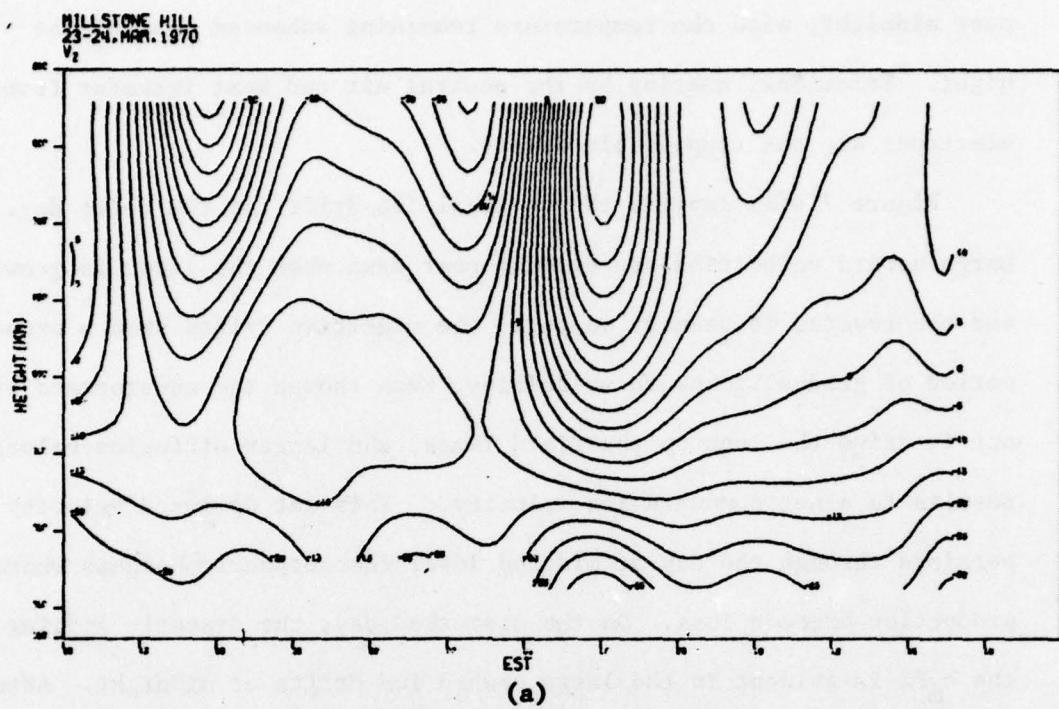
Figure 7.4 Same as Figure 7.1 except for vertical ion drift.

142
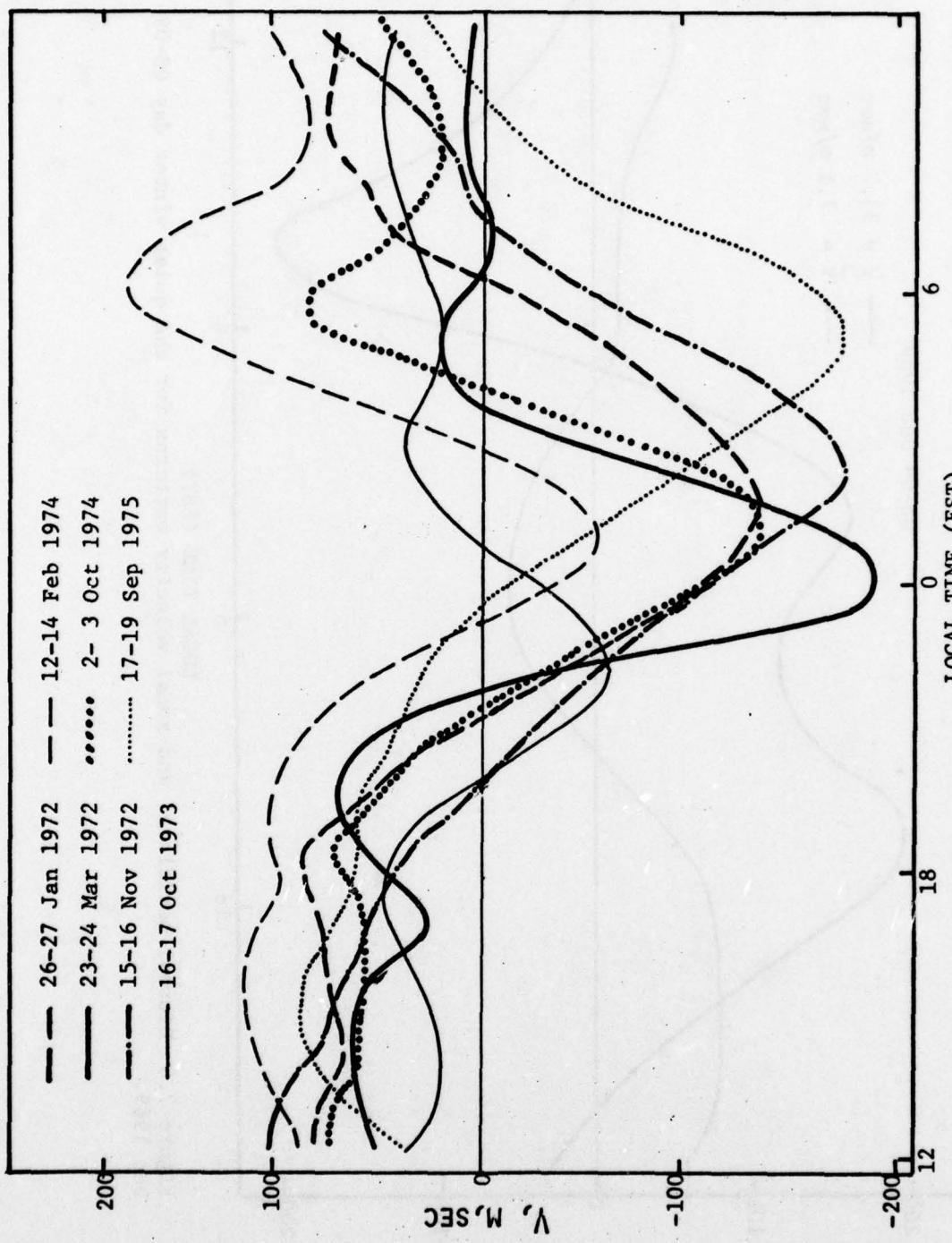
Figure 7.5 Diurnal meridional velocity pattern for seven equinox and winter disturbed days computed by the EMH model.

143
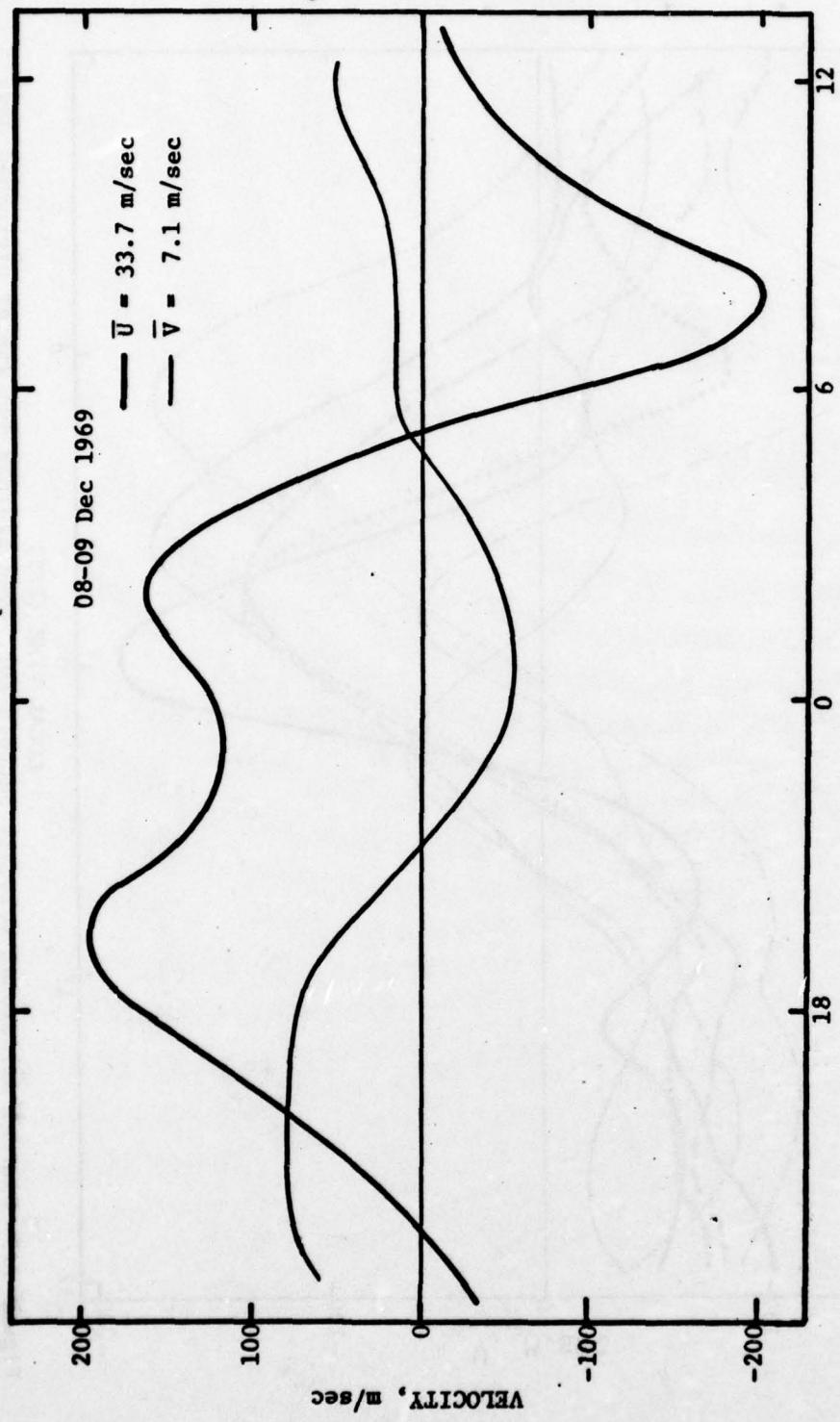
Figure 7.6 Diurnal meridional and zonal velocity patterns for the quiet winter day 08-09 Dec 1969.

144

equatorward nighttime winds are evident on all the days. The strongest
winds normally occur near local midnight. However, it appears this peak
wind can be displaced, and the exact time may depend on the occurrence
of a substorm. Since the EMH model uses a harmonic fit to the data to
calculate the gradients used in the computation of the winds, much of
the sharp features and fine structure of the experimental data is smoothed
out. This effect of the model will be discussed later in this Chapter.
Shown in Figure 7.6 is a quiet winter day (08-09 Dec 1969 $\overline{AE}$ = 104). It
is evident that in contrast to the relatively weak equatorward flow
throughout the night, the strong nighttime winds are a marked departure
from the normal pattern. The fluctuations in the wind pattern during
the daytime may be partly due to the forcing from below of the semi-
diurnal tide; most of the shorter period structure can be attributed to
gravity waves launched by the onset of auroral disturbances, as will be
shown. The daytime winds show no clear pattern of reduced poleward
winds, suggesting that on the dayside the normal wind pattern forced by
the solar heating is not significantly effected by the auroral heating.

Figure 7.7 depicts the zonal wind pattern for the same sample of
days. Typical winter days show a transition from eastward to westward
winds in the early morning, as seen in Figure 7.6. Hernandez and Roble
(1977) also saw a similar pattern, with the time of transition approach-
ing midnight at equinox. Five of the seven days shown had transitions
at or before midnight, with extremely strong westward winds after the
transition. For 15-16 Nov 1972, continuous substorm activity beginning on
the 15th appears to have enhanced the nighttime temperature, thus the

145
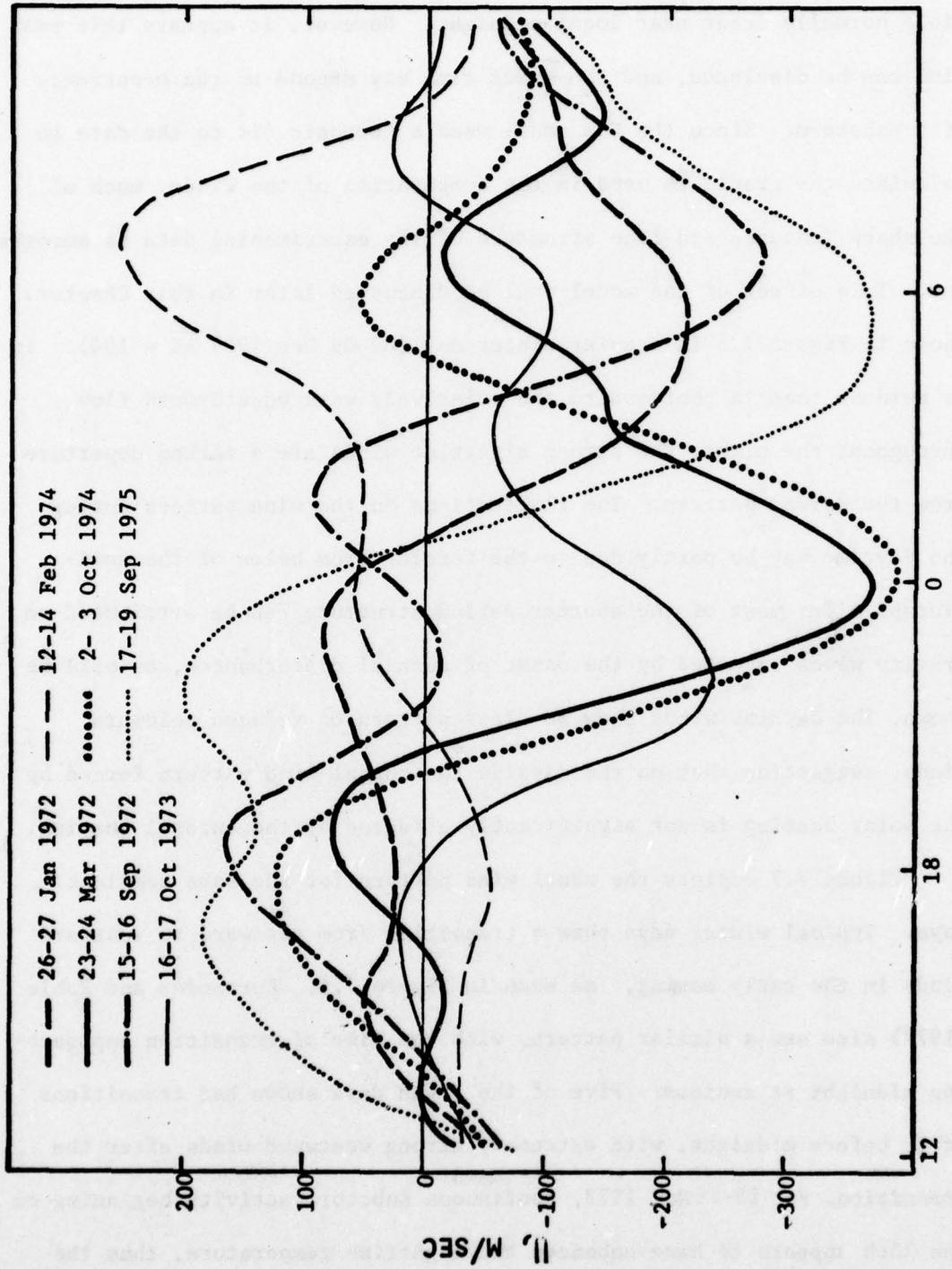
Figure 7.7 Same as Figure 7.5 except for zonal velocity.

26-27 Jan 1972 — 12-14 Feb 1974
23-24 Mar 1972 2- 3 Oct 1974
15-16 Sep 1972 17-19 Sep 1975
16-17 Oct 1973

LOCAL TIME (EST)

U, M/SEC

146

minimimum temperature did not occur until almost 0400 LT. The computed

pressure gradient forced the winds to remain eastward throughout the

night. At 0300 LT a long duration substorm began, the effect of which

is seen as a late surge in V and an enhanced exospheric temperature

(Figure 7.8). On 12-14 Feb 1974 the computed diurnal pattern is actually

reversed, with westward winds in the evening and eastward winds in the

morning.

7.1.3 Exospheric Temperature

Figure 7.8 shows the T_∞ patterns for the seven days shown previ-

ously together with the disturbed day 3-4 Apr 1974. These disturbed days

clearly do not follow the simple diurnal pattern found in the empirical

models, such as MSIS, nor the normal pattern deduced from ISR observa-

tions. All the days have large temperature enhancements near local

midnight, but there are other periods during the day when there are

sharp enhancements, some of which are directly correlated with auroral

substorms. For many of the days there are two temperature peaks during

the night, the first near midnight and a second at about 0300 LT.

Examination of the temperature pattern for 12-14 Feb 1974 explains the

strange zonal wind pattern seen in the previous section. Auroral distur-

bances began late on 11 Feb with five large substorms with AE over 1000γ

on the 11th and 12th. This apparently resulted in a large deposition of

heat in the nighttime sector and generated strong equatorward winds.

The nighttime temperature observed over Millstone is actually larger

than the daytime maximum due to solar heating. Use of a model that

considers only a narrow longitudinal belt, as the EMH model does, rather

147
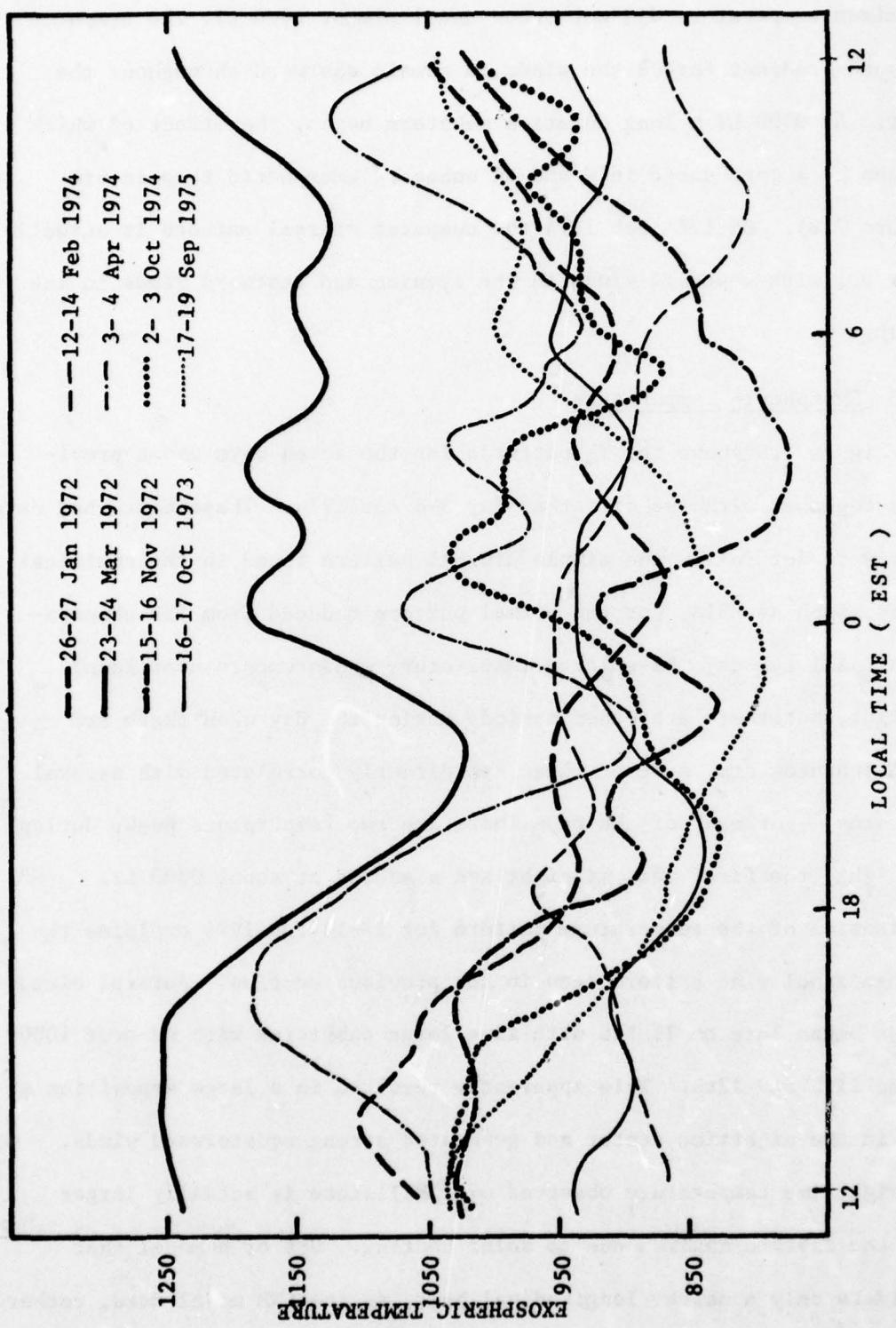
Figure 7.8 Twenty-four hour temperature profiles for a composit of disturbed days. All the days exhibit a large enhancement of temperature during the night.

26-27 Jan 1972 ———— 12-14 Feb 1974
23-24 Mar 1972 ———— 3- 4 Apr 1974
15-16 Nov 1972 ••••• 2- 3 Oct 1974
16-17 Oct 1973 ———— 17-19 Sep 1975

EXOSPHERIC TEMPERATURE

1250 · 150 · 1050 · 950 · 850

LOCAL TIME (EST)

12 · 18 · 0 · 6 · 12

than the global circulation, may not be valid in this case. The local temperature gradient does not truly represent the forcing which is driving the global circulation pattern, implying non-linear advective terms are important. This example does, however, demonstrate the importance of auroral heating on the behavior of the thermosphere at all other latitudes. For this particular day, solar activity was fairly low ($\overline{F}_{10.7}$ = 79.9), allowing a large input of auroral heating to be more important relative to the diminished solar heating.

7.1.4 Substorm Response

As mentioned above, the EMH model tends to smooth out the more detailed features in the data. Figure 7.9 shows the meridional velocity, T_∞, and hourly average AE for the disturbed summer day 17-18 Aug 1970. There are four distinct equatorward pulses in V which seem to be associated with increases in temperature. These occur near 1600 LT, at about 2000 LT just after a substorm, near 0400 LT associated with the increase in auroral activity, and a fluctuation near 1100 LT, apparently associated with the onset of a large substorm.

A more detailed look at the experimental data is given in Figure 7.10 which compares the derived neutral wind along the magnetic meridian, V_{Hn}, and AE. It can be seen that the equatorward flow near midnight actually comprises two different pulses which the harmonic fit has smoothed into one. The pulse at 2100 LT is clearly coincident with the substorm, which began at about 1940 LT, whereas the second just after midnight does not coincide with any substorm increase. The first equatorward pulse, which was near 1600 LT in the model, is closer to 1800 LT

149
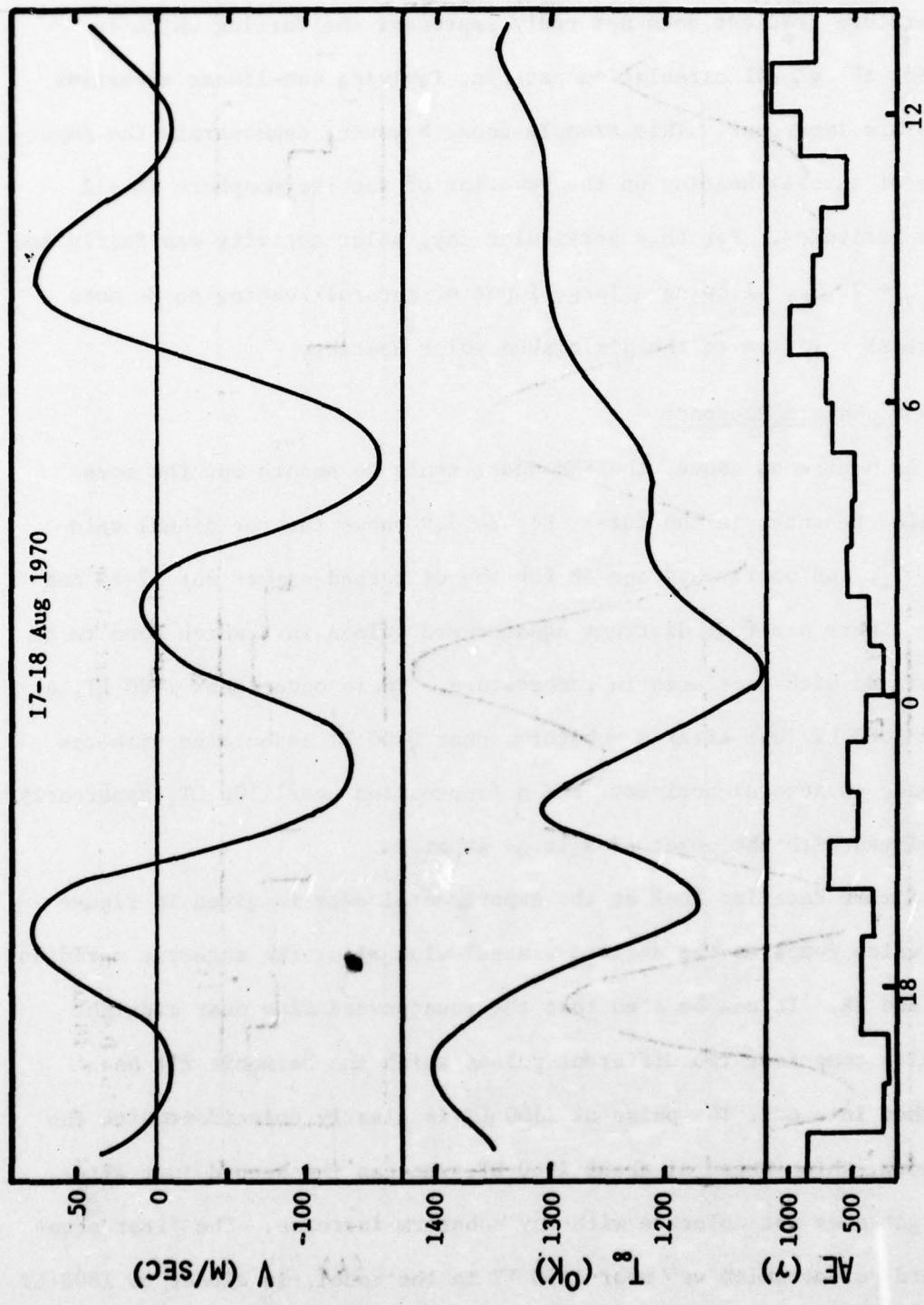
Figure 7.9 Diurnal meridional velocity pattern from the EMH model for 17-18 Aug 1970, plus the derived T_∞ pattern and the hourly average of AE.
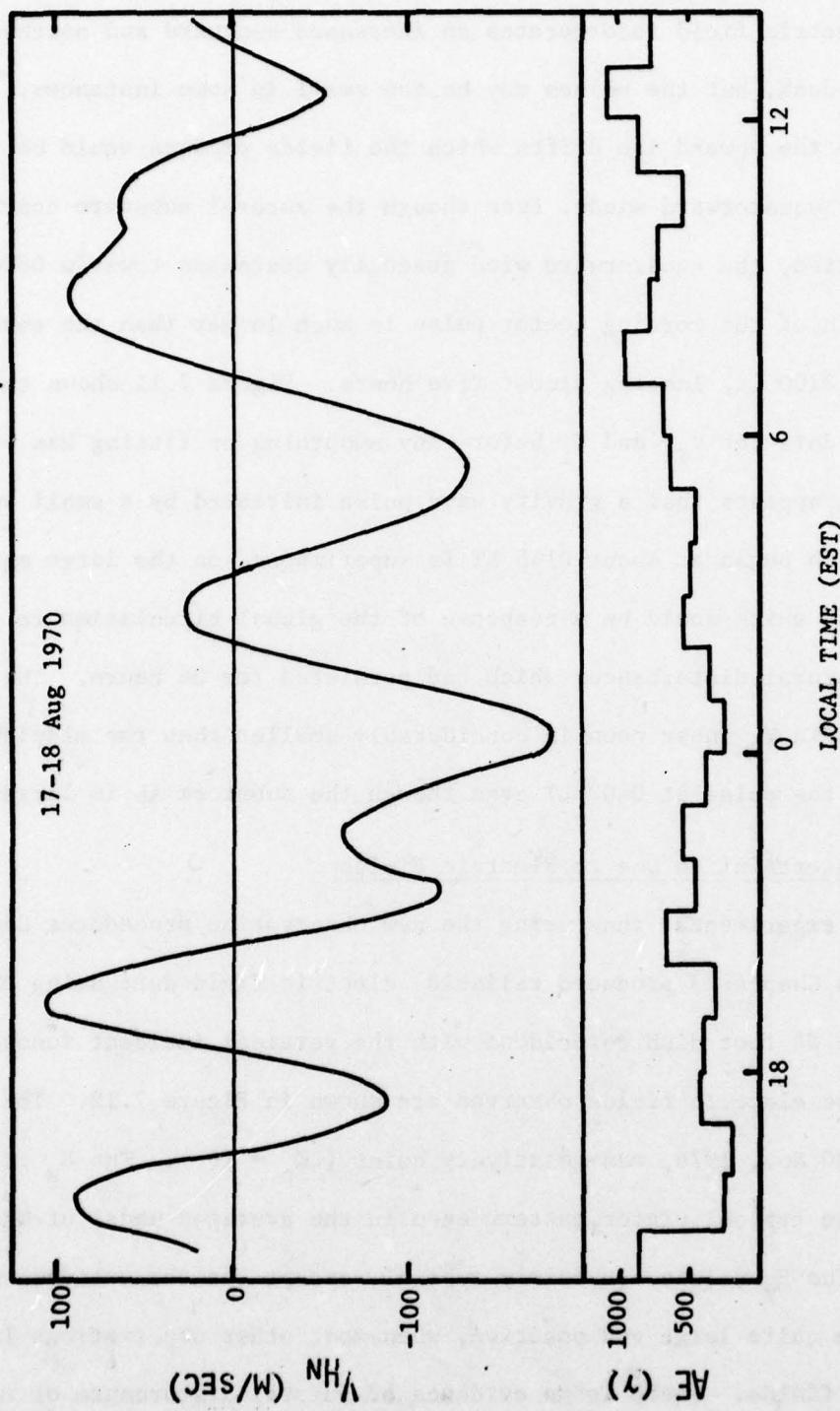
Figure 7.10 Derived neutral wind component along the magnetic meridian, V_{Hn}, and the AE Index for 17-18 Aug 1970.

in the data and may be an artifact of electic field data. The disturbed
model electric field incorporates an increased eastward and northward
field at dusk, but the values may be too small in some instances. In
this case the upward ion drifts which the fields produce would be inter-
preted as equatorward winds. Even though the auroral substorm continues
past sunrise, the equatorward wind gradually decreases towards 0800 LT.
The length of the morning sector pulse is much longer than the earlier
pulse at 2100 LT, lasting almost five hours. Figure 7.11 shows the
original data for V_{iz} and T_i before any smoothing or fitting has been
done. It appears that a gravity wave pulse initiated by a small sub-
storm which began at about 0145 LT is superimposed on the large equator-
ward winds which would be a response of the global circulation to the
strong auroral disturbances which had persisted for 24 hours. The
deviation in V_{Hn} near noon is considerably smaller than the midnight
surge or the pulse at 0400 LT even though the substorm AE is larger.

7.1.5 Uncertainites Due to Electric Fields

Two experimental runs using the new observation procedures des-
cribed in Chapter 3 produced reliable electric field data using the
steerable 84 foot dish coincident with the vertical incident ionospheric
data. The electric fields observed are shown in Figure 7.12. The first
day, 19-20 Nov, 1976, was relatively quiet (ΣK_p = 16-). The E_x values
follow the typical winter pattern seen in the averaged model of Wand
(1978). The E_y values are fairly typical, except for the pre-dawn values,
which are quite large and positive, when most other observations indicate
nefative fields. There is no evidence of auroral disturbance or related
activity. Despite the unusual structure in the morning winds, Wand

152
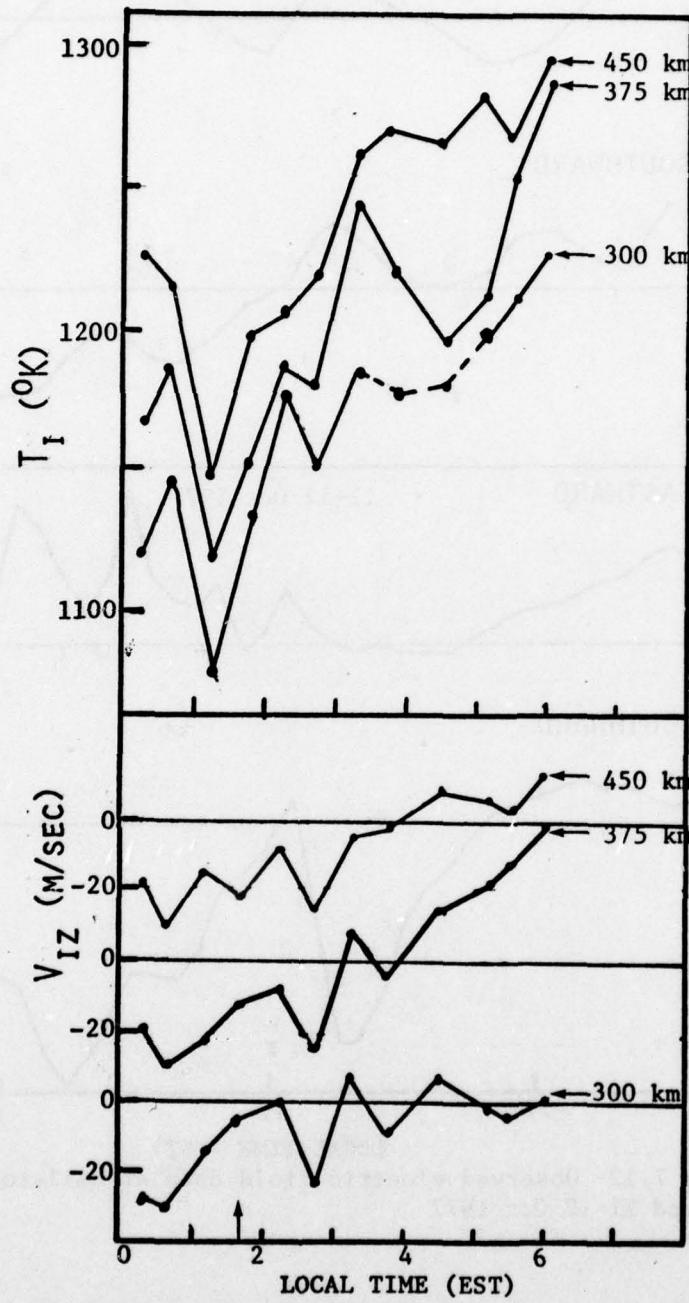
Figure 7.11 Raw data for V_{IZ} and T_i at nominal heights of 300, 375, and 450 km for 17-18 Aug 1970 showing the iono- spheric response to a small substorm which began about 0145 LT.
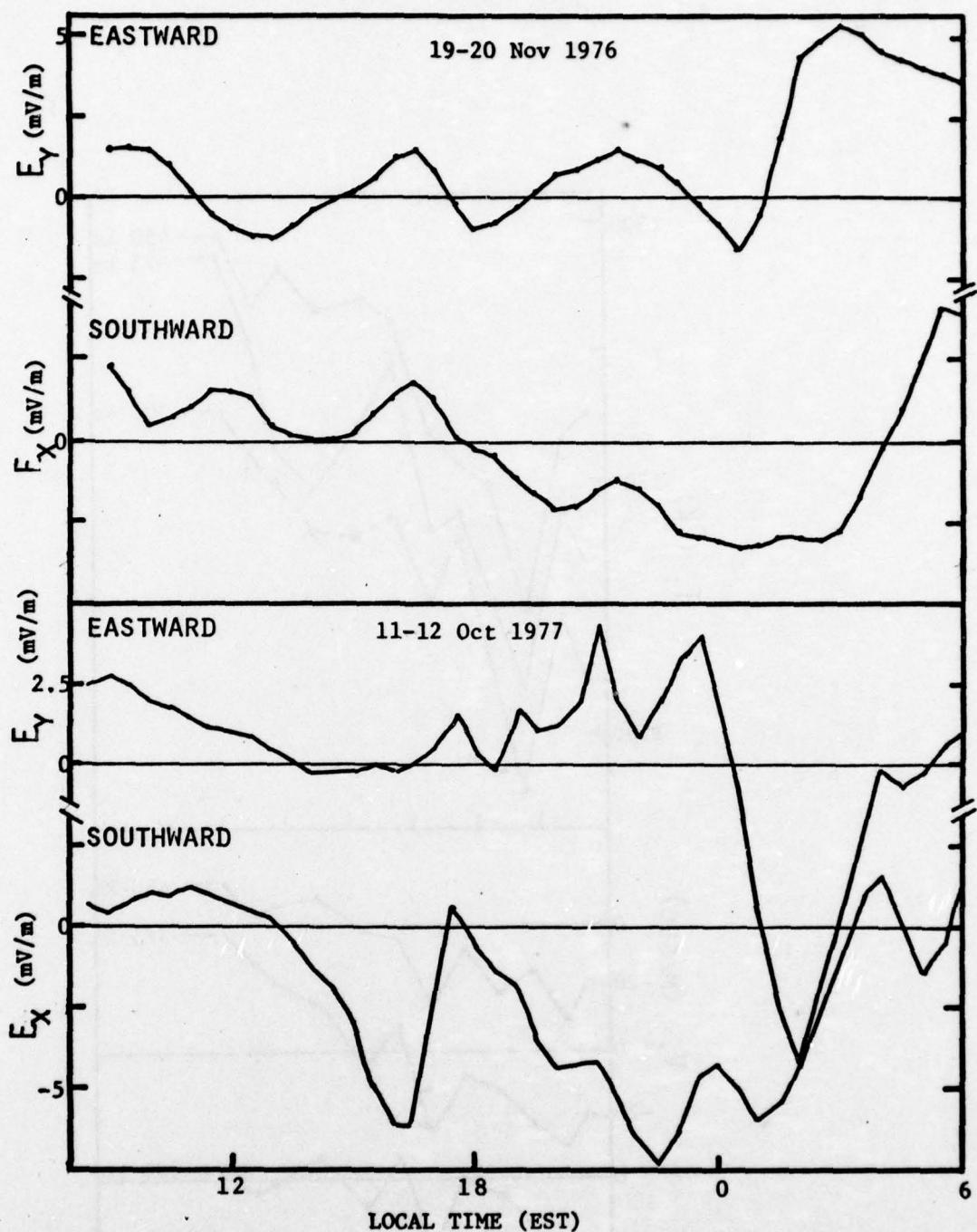
Figure 7.12 Observed electric field data at Millstone for 19-20 Nov
1976 and 11-12 Oct 1977

154

(private communication) feels the values represent the observed drifts. The electric fields for the disturbed day 11-12 Oct 1977 (ΣK_p = 36+) are typical of a disturbed day.

Each of the days was analyzed using the EMH model both with and without electric fields included. Figure 7.13 compares the zonal and meridional winds for the quiet day. The primary effect on the zonal winds on including the electric field is the net westward acceleration due primarily to the northward field at night. The field decreased the diurnally averaged wind from 31.4 m/sec eastward to 14.7 m/sec, giving a net change of 16.7 m/sec westward. The effect on the meridional winds is more pronounced, essentially because of the large E_x field in the morning. The wind pattern with the electric field is more like one would expect for a quiet winter day, suggesting that the unusual field was real. With the field there is a net change of 10.8 m/sec southward.

Figure 7.14 compares the computed winds for the disturbed day. The effect of including the proper electric field values on the meridional wind is obvious, with the midnight surge being more than doubled and considerably narrower. The inclusion of the electric field has also eliminated the slight equatorward surge near 1800 LT. For this particular day, the eastward field is small at dusk, so the overall difference is small. Despite the strong midnight surge, the net change in the mean meridional winds is only 4.7 m/sec. southward.

The zonal winds show the same net westward acceleration as the quiet day due to the northward field at night. The most noticeable difference is seen near 1600 LT where the inclusion of a large northward electric

155
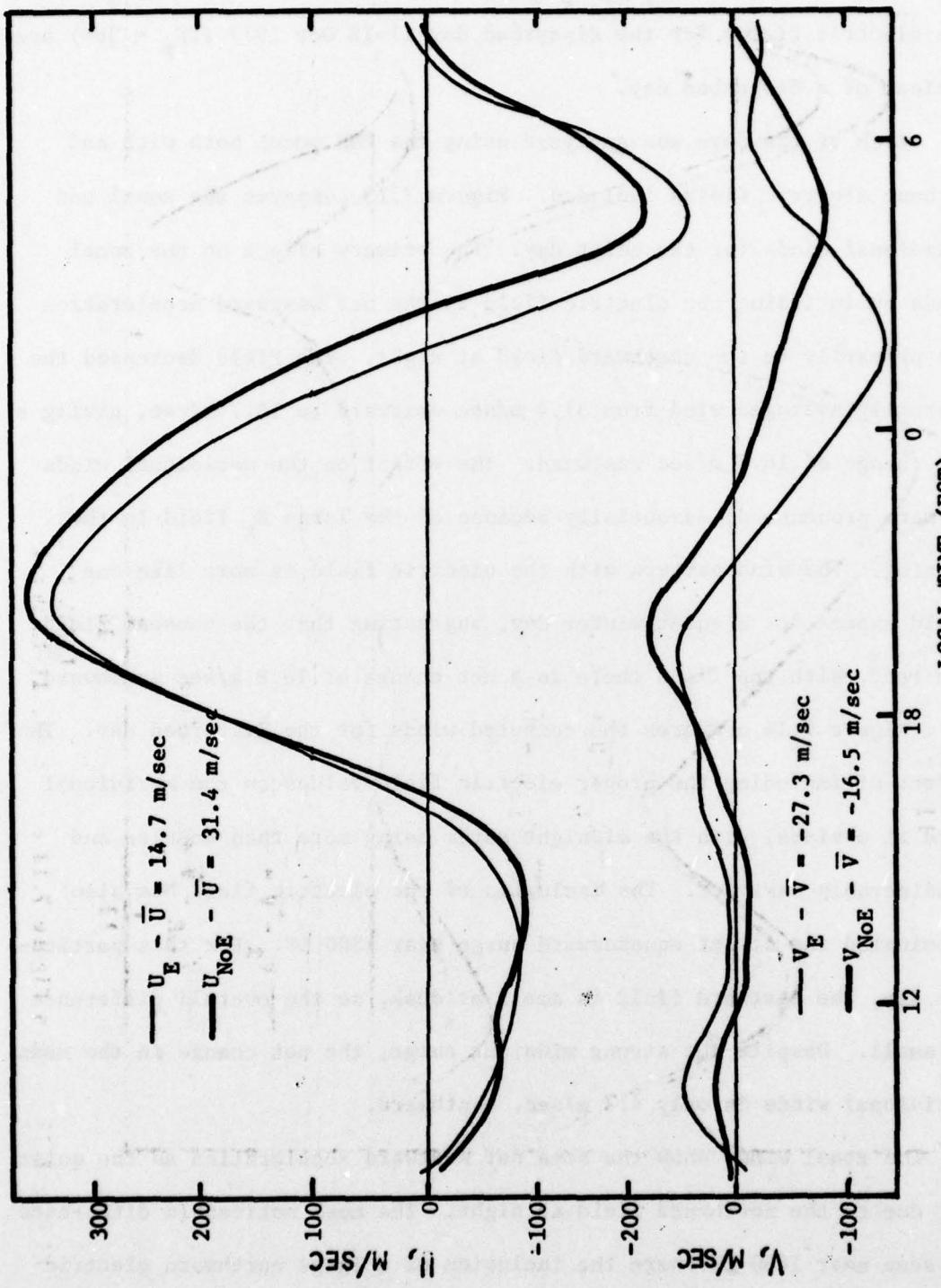
Figure 7.13 Diurnal zonal and meridional wind patterns for 19-20 Nov 1976 with and without electric field data included in the analysis.

11-12 Oct 1977

$U_E - \overline{U} = -42.4$ m/sec

$U_{NoE} - \overline{U} = -15.7$ m/sec

$V_E - \overline{V} = -24.9$ m/sec

$V_{NoE} - \overline{V} = -20.2$ m/sec

LOCAL TIME (EST)
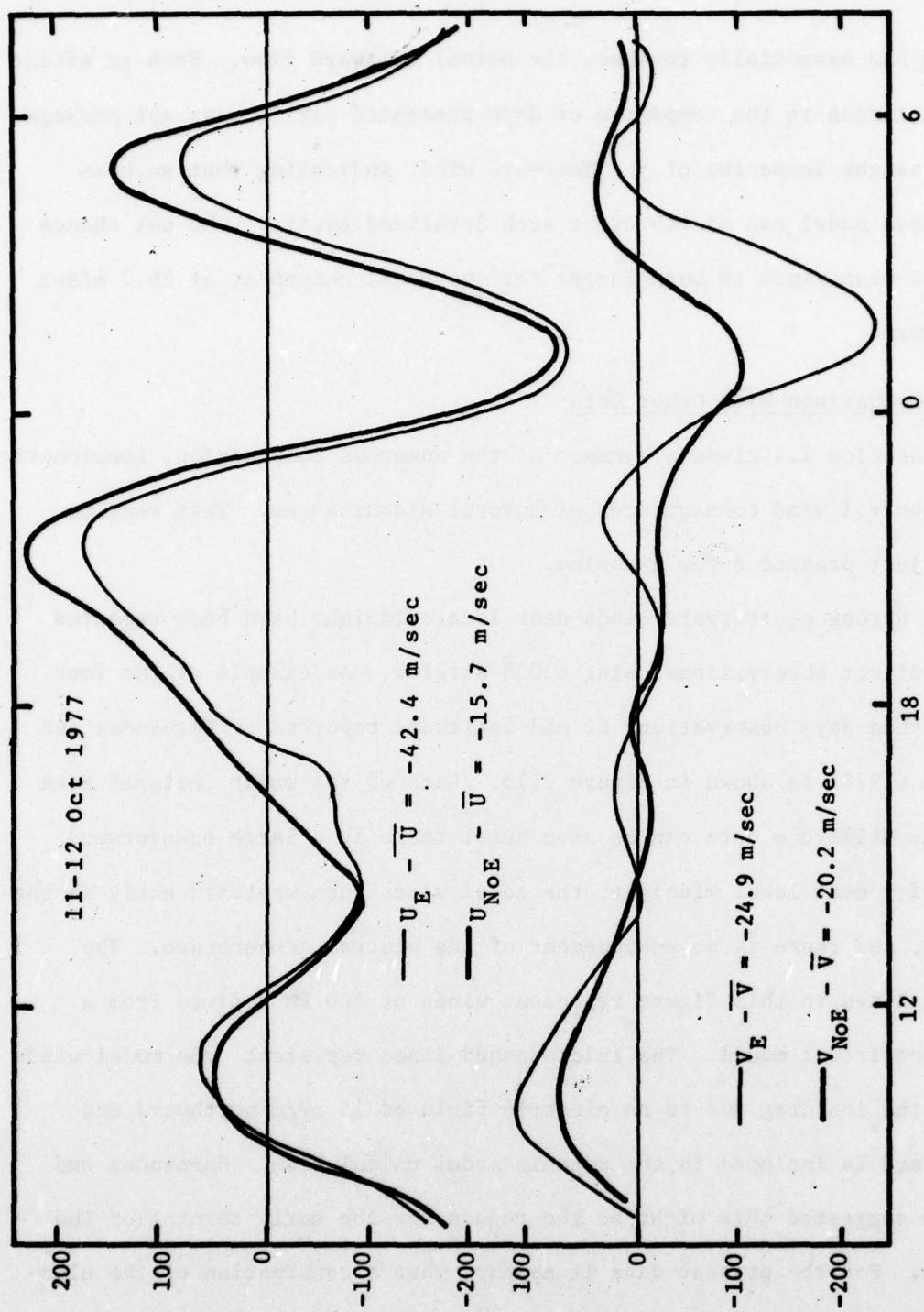
Figure 7.14 Same a Figure 7.13 except for 11-12 Oct 1977.

157

field has essentially reversed the normal eastward flow. Such an effect was not seen in the composite of days presented earlier, except perhaps as a slight lessening of the eastward wind, indicating that such an averaged model can misrepresent such localized events. The net change in the mean winds is much larger for the zonal component at 26.7 m/sec westward.

7.2 Comparison With Other Data

Section 2.4 gives a summary of the numerous composition, ionospheric, and neutral wind consequences of auroral disturbances. This section will just present a few examples.

Strong equatorward winds near local midnight have been reported from direct observations using 6300Å airglow. An example of the four disturbed days observations at mid-latitudes reported by Hernandez and Roble (1976) is shown in Figure 7.15. Each of the major features seen in the Millstone data can be seen here; there is a large equatorward velocity near local midnight, the zonal winds turn westward early in the night, and there is an enhancement of the neutral temperature. The solid lines in this figure represent winds at 300 km derived from a semi-empirical model. The thick dashed lines represent the model winds when the ion drag due to an electric field of 15 mV/m northward and westward is included in the dynamic model calculation. Hernandez and Roble suggested this might be the reason for the early turning of the winds. For the present data it appears that a combination of the electric field (about 5 mV/m northward) plus the strong nighttime heating are required to explain the results.

158
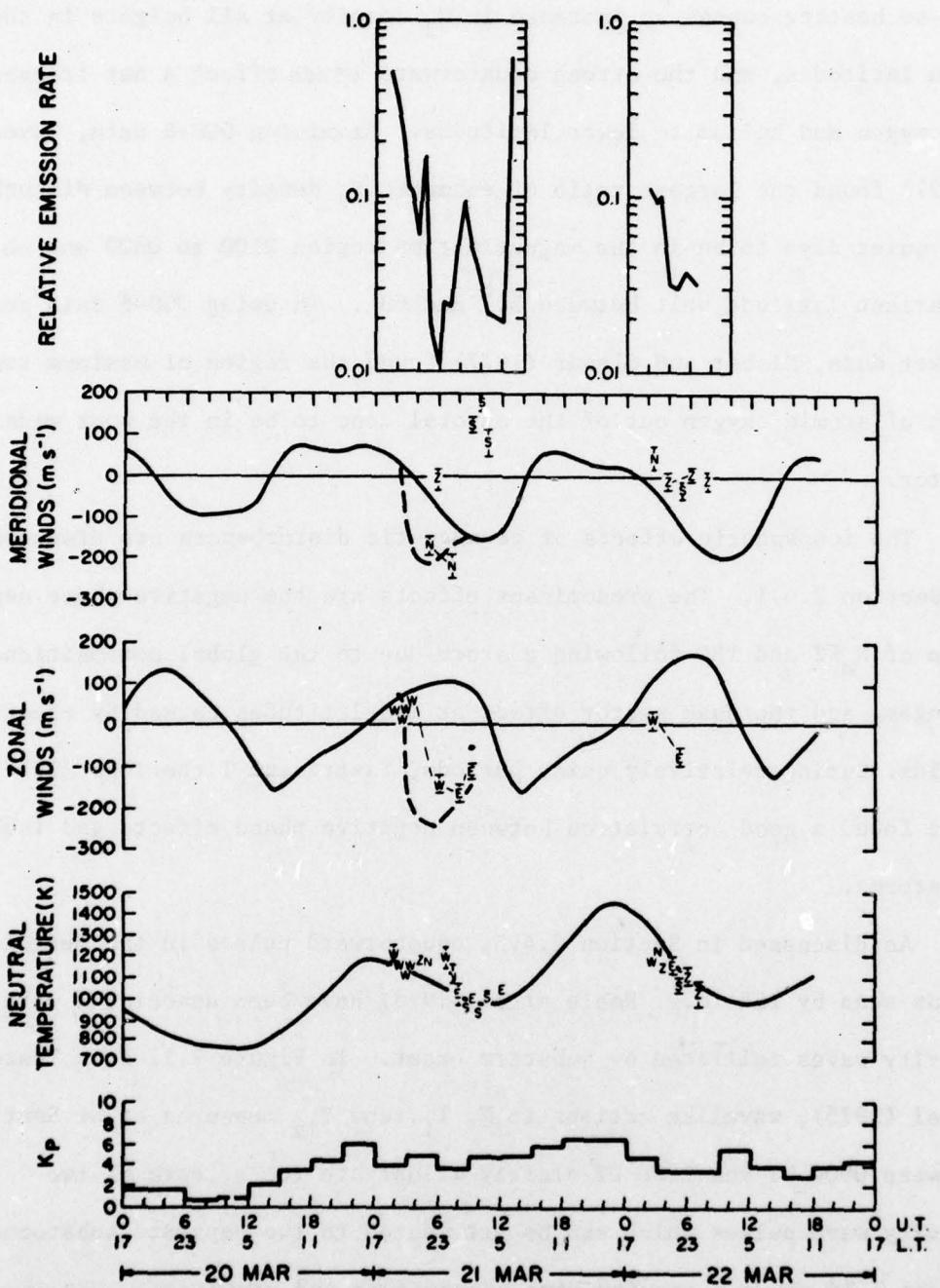
Figure 7.15 6300Å airglow observations of winds and temperatures observed by Hernandez and Roble (1976b). The letters represent the direction of individual observations. The solid and dashed lines are from a dynamic model.

159

Figure 7.16 depicts the time evolution of the neutral composition due to auroral heating and wind diffusion. The thermal expansion due to heating causes an increase in N_2 density at all heights in the high latitudes, and the strong equatorward winds effect a net transport of oxygen and helium to lower latitudes. Examining OGO-6 data, Tauesch (1977) found the largest ratio of enhanced N_2 density between disturbed and quiet days to be in the magnetic time region 2100 to 0300 and an invariant latitude belt between 50° and 60°. In using OGO-6 data and rocket data, Nisbet and Glenar (1977) found the region of maximum transport of atomic oxygen out of the auroral zone to be in the post midnight sector.

The ionospheric effects of geomagnetic disturbances are discussed in Section 2.4.1. The predominant effects are the negative phase depression of N_mF2 and TEC following a storm due to the global compositional changes, and the dusk sector effect at mid-latitudes caused by electric fields. During relatively quiet periods, Sastri and Titheridge (1977) have found a good correlation between negative phase effects and isolated substorms.

As discussed in Section 2.4.3, equatorward pulses in the meridional winds seen by 1SR (e.g. Roble et al, 1978) have been associated with gravity waves initiated by substorm onset. In Figure 7.17 from Testud et al (1975), wavelike motions in N, T_i, and V_{iz} measured at St Santin between 0900 UT and 1200 UT clearly illustrate the effects of two gravity wave pulses which can be attributed to two separate substorms. Figure 7.18 shows a gravity wave temperature and meridional wind structure 2500 km from its source from Testud et al's model. The temperature shows a wavelike oscillation, while the wind is just an equatorward pulse.

160
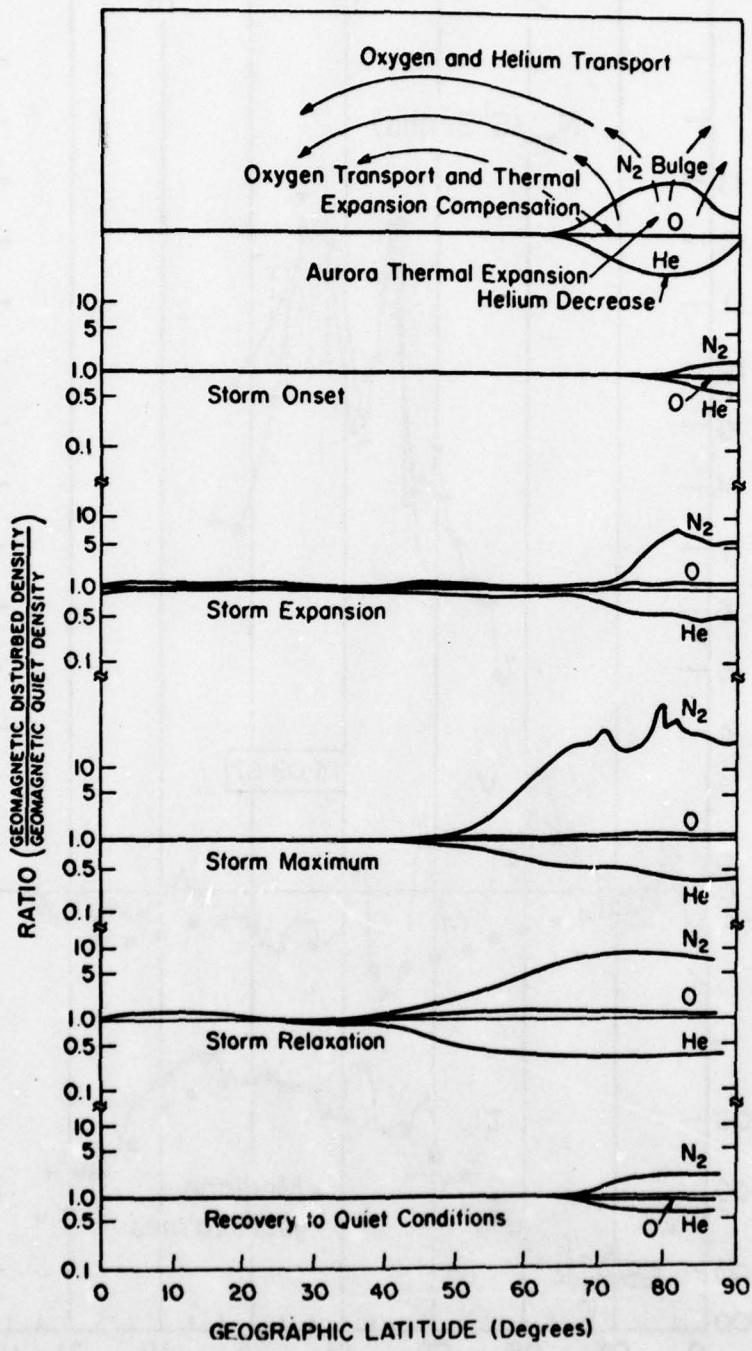
Figure 7.16 Depiction of the evolution of equatorward transport of mass and energy during a geomagnetic storm.
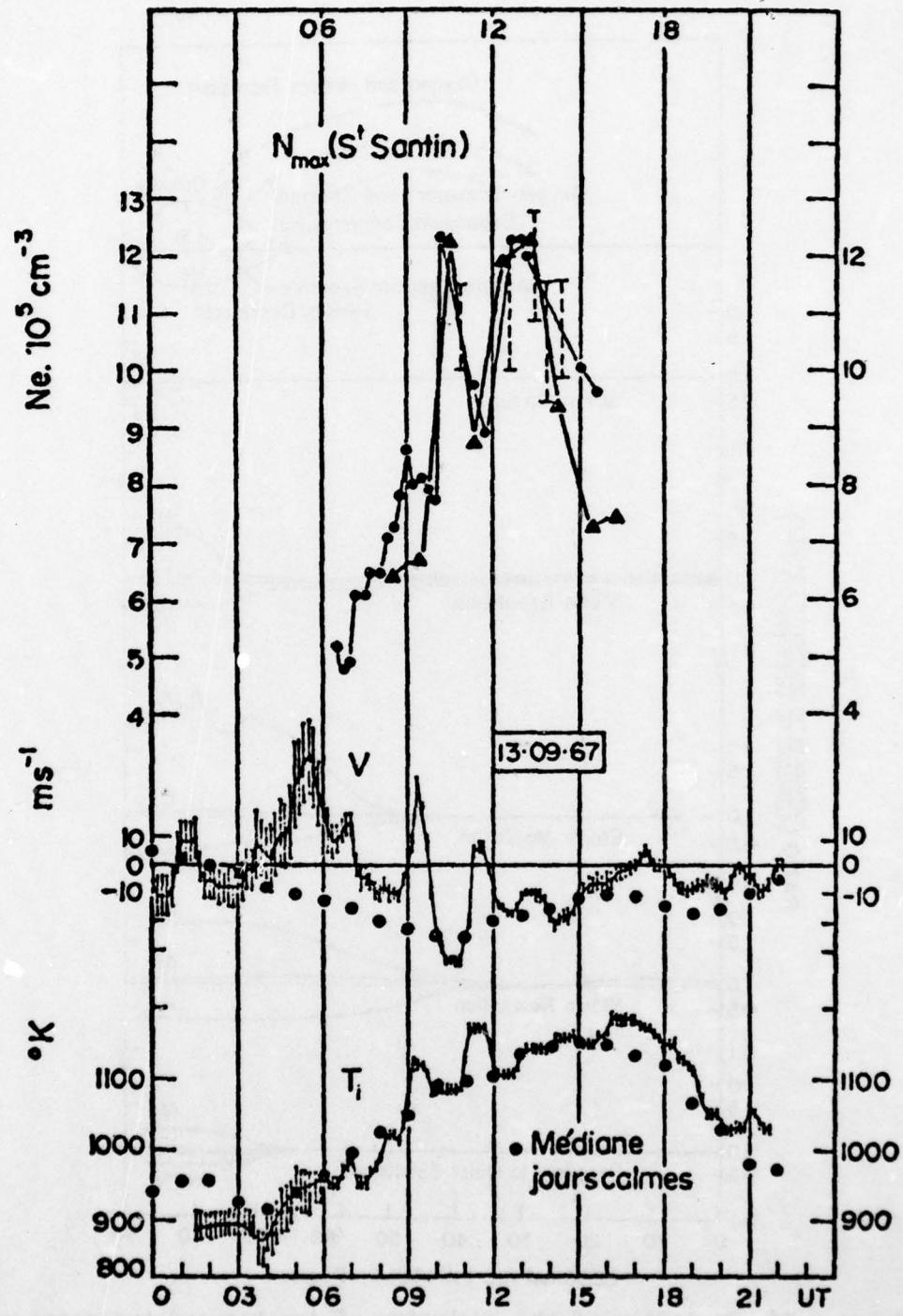
Figure 7.17 Example of ionospheric effects of gravity wave observed at St Santin. (From Testud et al, 1975).

162
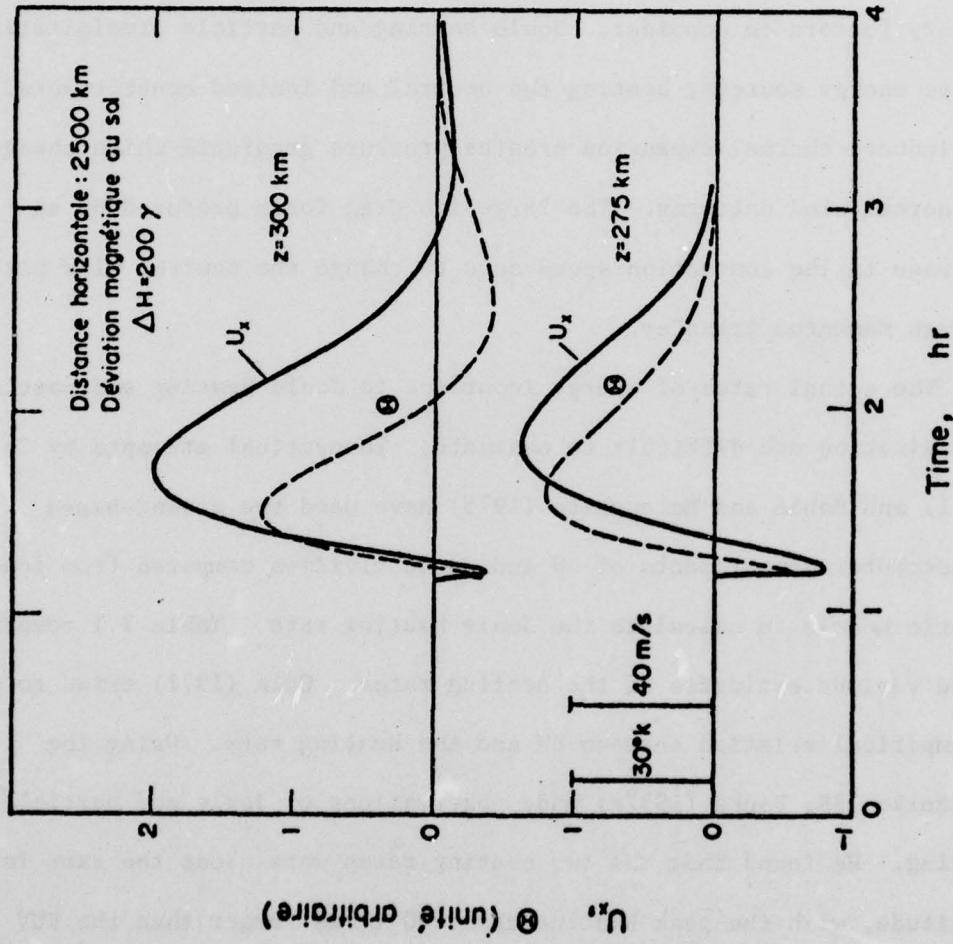
Figure 7.18 Meridional wind and temperature pattern of gravity wave 2500 km from its source from the model used by Testud et al (1975).

7.3 Discussion

7.3.1 Auroral and Polar Cap Energetics and Dynamics

Before relating the observed mid-latitude response to geomagnetic disturbance effects, it is necessary to develope a qualitative view of the high latitude processes which force the variations. There are three primary factors to consider. Joule heating and particle precipitation act as energy sources, heating the neutral and ionized constituents. The induced thermal expansion creates pressure gradients which change the normal wind patterns. The large ion drag force produced by an increase in the convection speed acts to change the neutral wind pattern through momentum transfer.

The actual rates of energy input due to Joule heating and particle precipitation are difficult to evaluate. Theoretical attempts by Cole (1971) and Roble and Matsushita (1975) have used the ground-based magnetometer measurements of ΔH and conductivities computed from iono-spheric models to calculate the Joule heating rate. Table 7.1 compares these various estimates of the heating rates. Cole (1971) tried to get an empirical relation between ΔH and the heating rate. Using the Chatanika ISR, Banks (1977a) made observations of Joule and particle heating. He found that the two heating rates were about the same in magnitude, with the peak heating about 50 times larger than the EUV heating rate. Hays et al (1975) have estimated the energy deposition in a 30 kiloRayliegh auroral arc to be more than 100 times the EUV heating, with the Joule heating about 10 times larger. Even though the particle heating in bright aurora can apparently exceed the Joule heating, Banks

164

(1977a) found most of the particle heating was too low (90-100 km) to substantially effect the thermospheric winds, while the Joule heating, which peaked between 120 and 150 km, could have a larger effect. The Joule heating rate, Q_j, is given by

$$Q_j = \sigma_p (\overline{E} + \overline{U} \times \overline{B})^2 \tag{7.1}$$

where σ_p is the Pedersen conductivity and $\overline{U}$ is the neutral wind. Uncertainty in the neutral wind magnitude can effect the ISR experimental results. For Q_j greater than 5 ergs $cm^{-2}s^{-1}$, Banks (1977a) found the uncertainty due to frictional heating below 150 km to introduce only small errors in the computed heating rate. The most recent estimates of Joule heating by Brekke and Rino (1978) claim to have considered the neutral wind effect in their theoretical development. Using a new high resolution observing procedure at the Chatanika ISR, they have presented new altitude profiles of the Joule heating rate during a relatively active period. They found the maximum heating to be in the 130 to 140 km height range.

Table 7.1

Height integrated Joule and particle precipitation heating rates in the electrojet regions. All values are in ergs/cm^{2}sec^{-1}. The values for Cole (1971) must be multiplied by the square of the local ΔH perturbation.

	Joule	Particle
Cole (1971),auroral event	$7 \times 10^{-4} \gamma^2$	
Hays et al (1975)	10	380
Roble and Matsushita (1975),quiet	0.2	
Roble and Matsushita,disturbed,peak	2.1	
Banks (1977),disturbed	20 to 50	10 to 40
Brekke and Rino (1978),disturbed	40 to 100	

165

When averaged over the hemisphere, Roble and Matsushita (1975) found the Joule heating rate was more than an order of magnitude smaller than the solar EUV heating, i.e. 0.014 ergs $cm^{-2}s^{-1}$ versus 0.68 ergs cm^{-2} s^{-1}. In order to obtain reasonable results from their model, Dickinson et al (1975) increased this by a factor of 20, but Q_j was still considerably smaller than the solar heating. Owing to the smallness of the optical depth of the atmosphere at thermospheric heights, the solar heating rate (1 - 3 ergs $cm^{-2}s^{-1}$) changes only slowly with latitude. By contrast the local Q_j of about 20 ergs $cm^{-2}s^{-1}$ at auroral latitudes is confined to the relatively small geographic area of the auroral oval making it an important driving force.

Most of the Joule heating occurs in the regions of the eastward and westward electrojets where the electric fields are largest. Around the Harang discontinuity, where the ion convective pattern diverges, the electric field reverses (Horowitz et al, 1978a), so the Joule heating rate is also small (Figure 7.18).

There is another region of heating in the daytime which is thought to play an important role in auroral dynamics. This is the "cleft" or "cusp" region located at the convergent point of the ion convective pattern. It is also a region where the magnetic field lines can connect directly with the IMF. The dynamics of the cusp region is just beginning to be understood. The cusp is thought to be a narrow throat in the ion

ION DRIFT   MILLSTONE HILL   13-14.MAY.1978
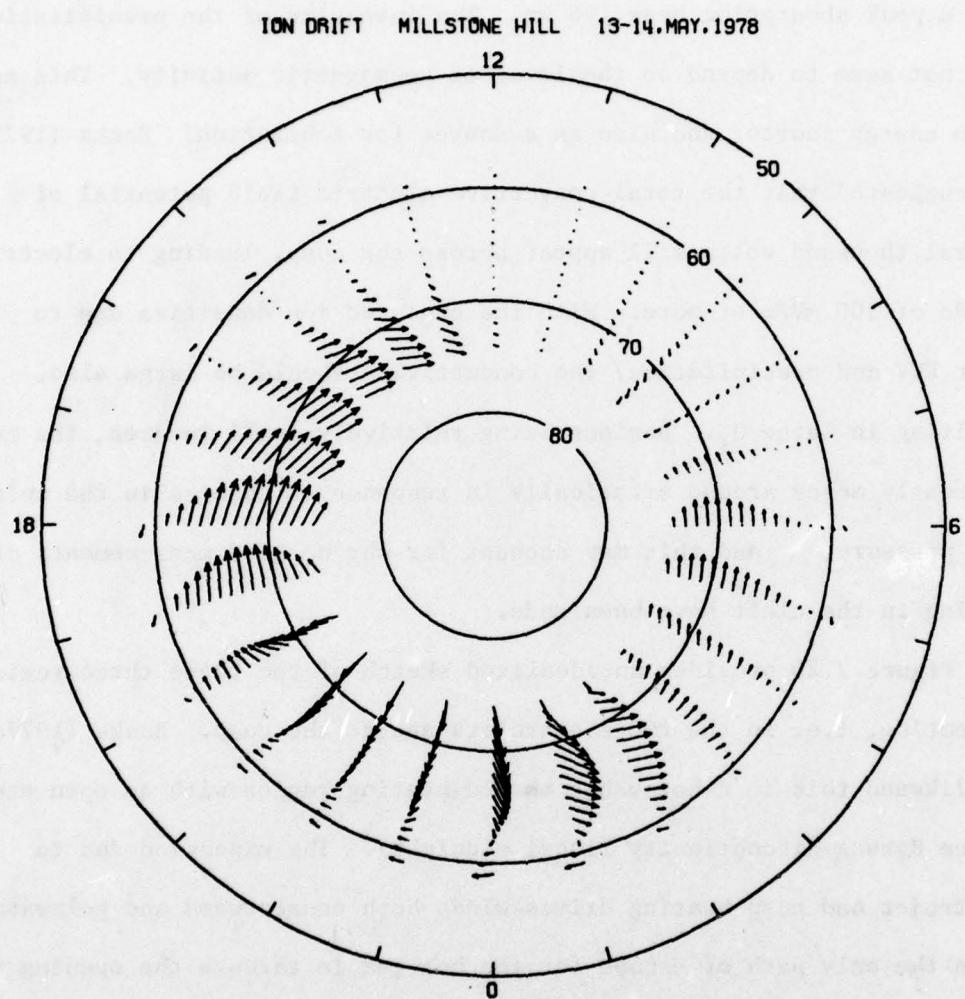
Figure 7.19   Ion convection pattern observed by the Millstone Hill ISR.

167

convective pattern about 1° to 2° wide in latitude and normally in the region between 77° and 81° invariant latitude (IL) near local magnetic noon. Satellite observations reported by Olson and Moe(1974), Doering et al (1976), and Titheridge (1976) show that there is a continous precipitation of low energy (less than 100 ev) electrons into the cleft, with a peak absorption near 196 km. The intensity of the precipitation does not seem to depend on the level of geomagnetic activity. This acts as an energy source, and also as a source for ionization. Banks (1977b) has suggested that the total convective electric field potential of several thousand volts will appear across the cusp, leading to electric fields of 100 mV/m or more. With the enhanced ion densities due to solar EUV and precipitation, the conductivity should be large also, resulting in large Q_j. Besides being relatively small in area, the cusp apparently moves around erratically in response to changes in the solar wind pressure, and this may account for why no good measurements of heating in the cleft have been made.

Figure 7.20 provides an idealized sketch of the these three regions of heating, i.e. in the two electrojets and at the cusp. Banks (1977a) has likened this to a horseshoe shaped heating region with an open end at the Harang discontinuity (local midnight). The expansion due to electrojet and cusp heating drives winds both equatorward and poleward, where the only path of escape for the hot gas is through the opening at local midnight. Figure 7.19 shows recent ISR observations of the high latitude ion convection pattern made from Millstone with the new steerable 150 foot dish. The ion drifts clearly conform to the general
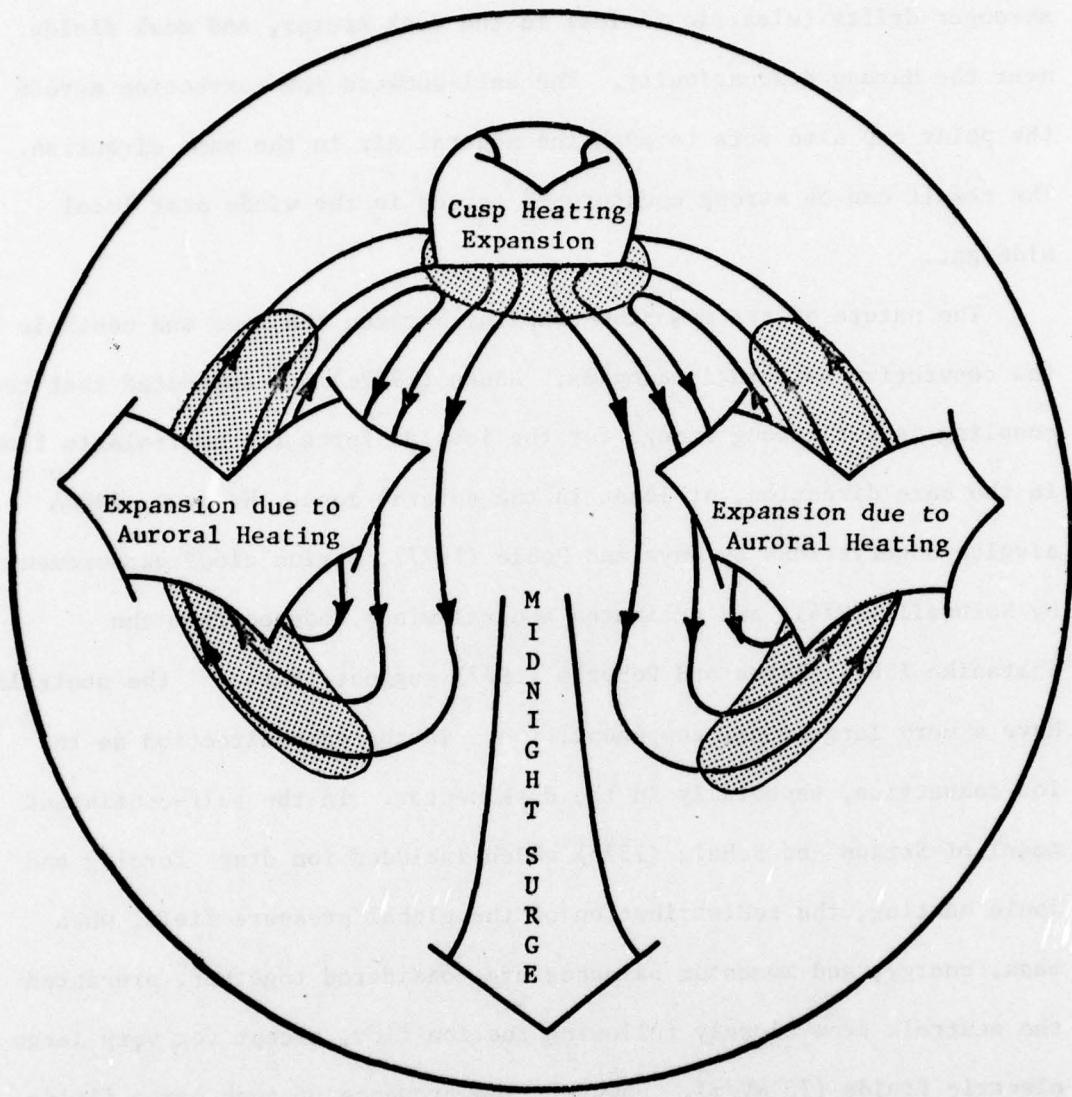
Figure 7.20 Schematic depiction illustrating the horseshoe shapped heating zones around the auroral oval which drive a neutral wind surge through the local midnight region.

pattern which has been inferred from the observed electric field and isolated barium cloud drift measurements. There are two distinct cells, stronger drifts (electric fields) in the dusk sector, and weak fields near the Harang discontinuity. The anti-sunward ion convection across the polar cap also acts to push the neutral air in the same direction. The result can be strong equatorward surges in the winds near local midnight.

The nature of the momentum coupling between the ions and neutrals in the convective pattern is complex. Banks (1977c) has suggested that the coupling is not strong enough for the ions to force the neutrals to flow in the same direction, at least in the auroral zone. However, 6300$\overset{o}{A}$ airglow observations by Hays and Roble (1977), barium cloud measurements by Rothwell (1974), and estimated neutral winds deduced from the Chatanika ISR by Bates and Roberts (1977) suggest that the neutrals have a very large zonal component, i.e. in the same direction as the ion convection, especially in the dusk sector. In the self-consistent model of Straus and Schulz (1975) which included ion drag forcing and Joule heating, the redistribution of the global pressure field, when mass, energy, and momentum balances are considered together, prevented the neutrals from closely following the ion flow, except for very large electric fields (75 mV/m). However, the presence of such large fields during substorms is not unusual (e.g. Wedde et al, 1978).

Mayr and Harris (1978) have applied their model to examine the differences between momentum and thermal forcing and conclude that the momentum forcing by the ion convection flow can force the neutrals into

170

a similar two cell pattern. But because of the non-divergent nature of the convection pattern, such momentum forcing would not play an important role in the global redistribution of mass and energy seen during auroral storms. This redistribution is accomplished by the thermal forcing.

There is one further complication that adds to the complexity of the auroral activity. The size of the auroral zone changes with the level of activity and the direction of the IMF B_z. The magnitude of the electric field also appears to increase as the size of the oval increases (Horowitz et al, 1978b). Figure 7.21 shows a schematic of the classical Akasofu substorm pattern. The auroral oval expands just before the first substorm onset and gradually contracts after each substorm. Expansion of the oval and an increase in the electric field will mean the auroral heating zone is at lower latitudes, the area of Joule heating is increased, and the magnitude of Q_j is also probably larger. Further, the momentum transfer through ion drag will be enhanced.

7.3.2 Interpretation of Wind Results

Based on the different aspects of auroral forcing just discussed, the fluctuations of the neutral winds, particularly the meridional wind, can be related to specific auroral processes. Referring to the plot of V_{Hn} in Figure 7.10 for the disturbed day 17-18 Aug 1970, the pulses at 2100 LT and 0500 LT can attributed to the equatorward forcing of the electrojet heating associated with individual substorms. Hedin et al (1977) and Trinks et al (1976) have reported localized variations in the global scale stormtime density pattern, which are consistent with brief

171
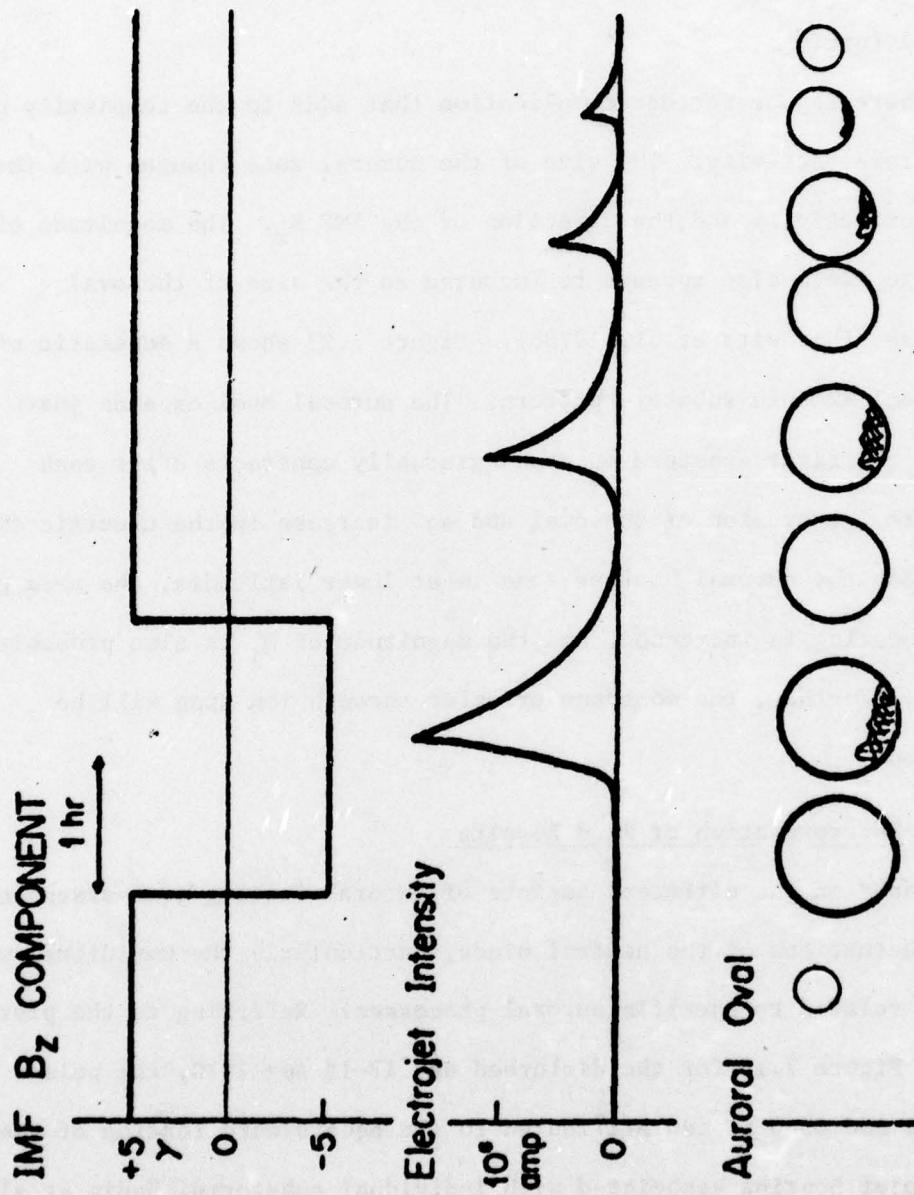
Figure 7.21 Schematic of a geomagnetic disturbance showing the expansion of the auroral oval at onset of the storm and a gradual contraction after each substorm. (From Akasofu and Lepping, 1977).

periods of enhanced equatorward transport of N_2 and O by the substorm induced winds seen here. The fact that the pulse near 0500 LT does not persist, even though the substorm activity increases is related to the rotation of the radar away from the auroral oval, which is at higher geographic latitudes during the day, and also the rotation of the radar away from the region of strongest heating, i.e. the westward electrojet. As noted previously, an increase in neutral temperature accompanies each pulse, indicative of heat transport to lower latitudes.

The equatorward pulse near noon on 17-18 Aug 1970 is probably associated with the region of heating in the cleft. The peak of the wave reached Millstone at 1230 LT. The substorm began at about 1100 LT. Assuming the cusp is at 80° IL, this would give a phase speed on the order of 500 m/sec, consistent with the gravity wave hypothesis. The effect of this pulse on N, T_e, T_i, and V_{iz} was similar to that observed by Roble et al (1978), only less dramatic.

The strong surge just after midnight, as distinct from the earlier substorm pulse,   can be interpreted as an extension of the midnight surge seen at auroral latitudes (Bates and Roberts, 1977).

Barium cloud drift measurements at subauroral latitudes (61° N IL) in the dusk sector by Roper and Baxter (1978) showed neutral winds with a large westward component, essentially parallel to the ion drifts, similar to the results of Hernandez and Roble (1976b). Using a dynamic model of the high latitude including Joule heating and electric field induced ion drifts, they found that the model could reproduce their results, with the westward acceleration due in part to the Coriolis

173

acceleration of meridional winds forced by the Joule heating and also due to the advection of westward momentum imposed on the wind by ion convection at higher latitudes. Since the EMH model neglects non-linear advection terms, these results of Roper and Baxter suggest the present model results may underestimate the westward acceleration, and so, overestimate the eastward winds in the dusk sector.

7.3.3. Electric Field Effects

The results for the disturbed day with coincident electric fields clearly demonstrate the importance of including electric field effects in the mid-latitude dynamics during periods of geomagnetic disturbances if a true picture of the diurnal circulation is to be obtained. The general features of a midnight surge and the early reversal in the zonal winds can still be seen without accurate electric field data, but the reversal in the zonal winds at dusk and the strength and narrowness of the midnight surge are not correctly represented. Also, some electric field-induced drifts, such as those in the dusk sector, may be erroneously interpreted as equatorward winds. The inclusion of accurate electric field results on the mean meridional winds introduces net changes comparable to those of including the quiettime electric fields. However, the effect on the zonal winds is quite large, with a net change of 26.7 m/sec versus 16.7 m/sec for the quiet November day. This result suggests that the inclusion of electric field drifts would make the westward shift in the diurnally averaged winds for disturbed days presented in Section 6.2.3 even more pronounced.

174

7.3.4 Solar Cycle Changes

With the variations in the diurnal wind pattern caused by auroral disturbances   so much dependent on the magnitude and local time of individual substorms, making any definitive conclusions about either seasonal or solar cycle changes is questionable. The only clear difference appears to be in the strength of the midnight surge on summer days compared with the winter and equinox days. The summer nighttime meridional winds are already relatively large, and the midnight surge is not as obvious as in winter and equinox, when the winds are weaker. The summer polar cap is sunlit 24 hours, leading to higher ion densities, higher Joule heating levels, and presumably higher momentum forcing. It may be that the enhanced heating and ion drag forcing during substorms are significantly larger in the summer that the winter hemisphere. Oliver (1977) has examined daytime measurements of T_∞ made at Millstone in an independent data set and found that the difference between observed and MSIS model temperatures when there is auroral activity is greater in the summer hemisphere. The summer days seemed to have a closer correlation between increased $\overline{AE}$ and more equatorward winds, but there is no clear evidence that there is a clear seasonal difference. The energetics and dynamics of the high latitude thermosphere are still only poorly understood, so a better explanation requires more theoretical and observational developements.

For the few disturbed days of observations gathered towards the end of the solar cycle, the midnight surge is still quite evident, and the fluctuation in V_{Hn} associated with individual substorms can still be

175

seen. For measurements made during the 10-15 Feb 1974 storm period near solar minimum, Hedin et al (1977) have reported typical disturbed period variations in the global density structure. Also, the measured O/N_2 ratio correlated well with the observed f_oF2, which showed a negative phase effect, even though the seasonal anomaly in f_oF2 was very weak.

8. SUMMARY

8.1 Conclusions

In this section we summarize the contributions of this thesis to
the understanding of the dynamics of the thermosphere and make some
suggestions for future work.

8.1.1 Analysis Procedures

We examined the role of frictional heating of the ions by the
neutral winds in the thermosphere. This effect is important because the
neglect of this heating term in the ion heat balance equation leads to
an overestimate of the computed T_∞. For relative ion-neutral velocities
of about 250 m/sec, frictional heating decreases the derived T_∞ by about
25°K. For disturbed days when there are large nocturnal winds and
periods of temperature enhancement, the inclusion of frictional heating
clearly is significant in the derivation of T_∞ and the winds computed
from the diurnal T_∞ pattern.

The importance of including electric field data in the calculation
of neutral winds during disturbed periods has been demonstrated. The
structure of the diurnal wind pattern, particularly the meridional
velocity, cannot be represented correctly without considering electric
field effects. However, the use of available model electric fields,
although better than neglecting the fields, does not provide a complete
picture of these effects.

The impact of ignoring the electric fields on the diurnally averaged
values is less severe on the meridional winds, although with the neglect
of the large ion drag effect on the zonal winds, the computed values are

177

shifted eastward by a significant amount. These two facts should be considered when comparing calculated winds with zonally averaged predictions from the model of Dickinson et al (1975, 1977).

8.1.2 Solar Cycle Variations

In order to determine if there are changes in the thermospheric circulation as solar activity decreases, data from 42 "one-pulse" experimental runs were reduced, edited, and analyzed from which 46 separate values of diurnally averaged zonal and meridional winds were obtained using the EMH dynamic model. By including 37 days analyzed by Emery (1977), a total of 83 days over the period 1970, near solar maximum, through 1975, at solar minimum, were examined. We have shown that the seasonal variation seen by Emery persists through the solar cycle with only slight changes in phase and magnitude. These results are consistent with the model of Roble et al (1977) which predicts no significant change in the annual variation in either the meridional or zonal winds. Apparently the decrease in the diurnal temperature gradient due to the decreased EUV and UV flux is balanced by an equal decrease in the ion drag as $N_m F2$ decreases. The results are also compatible with Roble et al's prediction that the high latitude reverse cell disappears at solar minimum, leading to more poleward winter winds.

8.1.3 Geomagnetic Effects

We has confirmed the existence of a modulation in the strength of the zonal circulation pattern with variations in geomagnetic activity. Although a correlation between more equatorward $\overline{V}$ and $\overline{AE}$ is not as clear (Figures 6.5 and 6.10), the examination of the diurnal wind pattern for 21 individual disturbed days with $\overline{AE} \geq 300$ clearly shows greatly enhanced

178

nighttime equatorward winds. One reason why the correlation is not stronger may be that the neglect of non-linear terms in the zonal momentum equation, plus unrealistic electric field values, results in the computed zonal winds being too eastward. In the time integration scheme, the EMH model first computes u at each time step, and then calculates vV using equation 4.7. If u were more westward in the pre-midnight sector, as observations suggest (e.g. Hernandez and Roble, 1976b), when V_{Hn} is negative, the computed v would be more equatorward. Even without these considerations, the diurnally averaged zonal winds still show a strong shift to more westward winds.

Although the superposition of the synoptic scale gravity waves on the planetary scale response to the disturbances complicates the analysis, as shown in the pulse" seen in the post midnight sector of 17-18 Aug 1970, the different responses can be differentiated. This research has demonstrated that there are three distinct disturbed period effects seen in the thermospheric winds, viz: i) the increased nighttime equatorward winds plus the more westward diurnally averaged winds seen statistically in the complete data set, which represents a planetary scale change in the circulation forced by the high latitude heating with the more westward winds resulting from the transport of heat to mid-latitudes, ii) the midnight surge consistently seen on disturbed days which is an extension of the high latitude surge forced by a combination of the ion convective flow and the thermal expansion of the horseshoe shape auroral heating region, and iii) the synoptic scale gravity wave seen on a case-by-case basis as a response to the short-time scale substorms.

179

8.2 Suggestions for Future Work

Emery (1977) suggested several improvements in the EMH model, such as inclusion of non-linear terms and using some other fit to the data than a harmonic function so variations in T and V_{Hn} which are not strictly diurnal can be considered. There is clear evidence that O is not in diffusive equilibrium below 200 km (Hedin et al, 1977). The use of some correcting factor, such as used in the MSIS model, to compensate for this could also be included. Such fine tuning of the model was not attempted in this research, since the emphasis was to examine the variation in the general pattern of the global circulation, rather than improve the accuracy of the model results. However, such improvements would certainly enhance the value of the model.

The addition of the 150 foot steerable antenna to the Millstone Hill Observatory offers exciting possibilities for improved observing programs. First, the antenna can be pointed along the field line, thus eliminating any electric field effects from the measurements which presently add uncertainty to the neutral wind deduced from the vertical incident antenna data.

The present results have related the strength of the meridional wind to Joule heating in a qualitative way using the AE index. With the present high latitude observing program, the winds deduced from the vertically incident radar can be compared with observations of the speed of the ion convection flow (recall $V_i \sim E$ and $Q_j \sim E^2$), so a more quantitative correlation of V_{Hn} and Q_j can be made.

A third possible observation program includes the installation of a

surplus Navy radar north of Millstone Hill. This radar could make forward scatter measurements using the beam transmitted from Millstone, making possible measurements of the latitudinal variation of winds and temperature.

REFERENCES

Abbreviations: JATP........Journal Of Atmospheric and Terrestrial
                                Physics
                JGR.........Journal of Geophysical Research
                PSS.........Planetary and Space Science

Akasofu, S.-I. and R.P. Lepping, 1975; Interplanetary magnetic field
and magnetospheric substorms, PSS,25,895.

Alcayde, D. and P. Bauer, 1977; Modelisation des concentrations d'oxygene
atomique observees par diffusion incoherente, Ann. Geophys., 33, 305.

Amayenc, P., 1974; Tidal oscillations of the meridional neutral winds at
mid-latitudes, Rad. Sc., 9, 281.

Antonaidis, D.A., 1976; Thermospheric winds and exospheric temperatures
from incoherent scatter radar measurements in four seasons, JATP,
38, 187.

Banks, P.M., 1966a; Collision frequencies and energy transfer, electrons,
PSS, 14, 1085.

_____, 1966b; Collision frequencies and energy transfer, ions, PSS,
14, 1103.

_____, 1967; Ion temperature in the upper atmosphere, JGR, 72, 3365.

_____, 1977a; Observations of Joule and particle heating in the
auroral zone, JATP, 39, 179.

_____, 1977b; "AGU Chapman Conference; 2nd Magnetospheric Cleft
Symposium," EØS, 58, 977.

_____, 1977c; Heat and momentum sources at high latitudes, EØS,
58, 703 (abstract).

Banks, P.M. and G. Kockarts, 1973; Aeronomy, Parts A & B, Academci
Press, New York, 430 and 355 pp.

Bates, D.R., 1959; Some problems conderning the terrestrial atmosphere
above the 100 km level, Proc. Roy. Soc. London A, 253, 451.

Bates, H.F., 1977; The circulation of the polar cap thermosphere, EØS,
58, 682 (abstract).

Bates, H.F. and T.D. Roberts, 1977a; The southward midnight surge in
F-layer wind observed with the Chatanika incoherent scatter radar,
JATP, 39, 87.

182

_____, 1977b; A technique for using incoherent scatter to estimate F-region zonal winds during Joule heating, JATP, 39, 1293.

Bauer, P., P. Waldteufel and D. Alcayde, 1970: Diurnal variations of the atomic oxygen density and temperature determined from incoherent scatter measurements in the ionospheric F region, JGR, 75, 4825.

Blanc, M. and P. Amayenc, 1976; Contribution of incoherent scatter radars to the study of middle and low latitude ionospheric electric fields, Atmos. Physics from Spacelab, J.J. Burger, ed., D. Reidel, New York.

Blanc, M., P. Amayenc, P. Bauer, and C. Taieb, 1977; Electric field induced drifts from the French incoherent scatter facility, JGR, 82, 87.

Blum, P.W. and I. Harris, 1975a; Full non-linear treatment of the global thermospheric wind system - I. mathematical method and analysis of forces, JATP, 37, 193.

_____, 1975b; Full non-linear treatment of the global thermospheric wind system - II results and comparison with observation, JATP, 37, 312.

Brekke, A. and C.L. Rino, 1978; High-resolution altitude profiles of the auroral zone energy dissipation due to ionospheric currents, JGR, 83, 2517.

Carpenter, D.L. and N.T. Seely, 1976; Cross-L plasma drifts in the outer plasmasphere; quiettime patterns and some substorm effects, JGR, 81, 2728.

Carpenter, L.A. and V.W.F.H. Kirchhoff, 1974; Daytime three dimensional drifts at Millstone Hill Observatory, Rad. Sc., 9, 217.

_____, 1975; Comparison of high-latitude and mid-latitude ionosphere electric fields, JGR, 80, 1810.

Chandra, S. and N.W. Spencer, 1976; Thermospheric storms and related ionospheric effects, JGR, 81, 5018.

Ching, B.K. and Y.T. Chiu, 1973; A phenomenological model of global ionospheric electron density in the E-, F1-, and F2-regions, JATP, 35, 1615.

Clauer, C.R. and R.L. McPherron, 1974; Mapping the local-time-universal time developement of magnetospheric substorms using mid-latitude magnetic observations, JGR, 79, 2811.

Cole, K.D., 1971; Electrodynamic heating and movement of the thermosphere, PSS, 19, 59.

Cox, L.P. and J.V. Evans, 1970; Seasonal variation of the O/N_2 ratio in the Fl-region, JGR, 75, 6271.

Creekmore, J.P., J.M. Straus, R.M. Harris, B.K. King, and Y.T. Chiu, 1975; A global codel of thermospheric dynamics I wind and density fields derived from a phenomenological temperature, JATP, 37, 491.

Davis, M.J. and A.V. DaRosa, 1969; Traveling ionospheric disturbances originating in the auroral oval during polar substorms, JGR, 74, 5721.

Dickinson, R.E. and J.E. Geisler, 1968; Vertical motion fields in the middle thermosphere from satellite drag densities, Mon. Wea. Rev., 96, 606.

Dickinson, R.E., E.C. Ridley, and R.G. Roble, 1975; Meridional circulation in the thermosphere I. equinox conditions, J. Atmos. Phys., 32, 1737.

_____, 1977; Meridional circulation in the thermosphere II. solstice conditions, J. Atmos. Phys., 34, 178.

Doering, J.P., T.A. Potemra, W.K. Peterson, and C.O. Bostrum, 1976; Characteristic energy spectra of 1-500 ev electrons observed in the high-latitude ionosphere from Atmospheric Explorer C, JGR, 81, 5507.

Emery, B.A., 1977; Seasonal wind variations in the mid-latitude thermosphere, ScD. Thesis, MIT, 315 pp.

_____, 1978; Neutral winds deduced above Millstone Hill: II. seasonal winds variations, 1970-1971, submitted to JGR.

Evans, J.V., 1969; Theory and practice of ionosphere study by Thomson scatter radar, Proc. of the IEEE, 54, 496.

_____, 1971; Measurement of F-region vertical velocites at Millstone Hill, 1, eveidence for drifts due to expansion, contraction, and winds, Rad. Sc., 6, 609.

_____, 1972a; Measurements of horizontal drifts in the E and F-regions at Millstone Hill, JGR, 77, 3241.

_____, 1972b; Ionospheric movements measured by incoherent scatter; A review, JATP, 34, 175.

_____, 1974; Some post-war developements in ground-based radiowave sounding of the ionosphere, JATP, 36, 2183.

_____, 1976; The dynamics of the ionosphere and upper atmosphere, Proc. Intl.Symp. STP, Boulder, CO., Vol II, 630.

184

Evans, J.V. and J.M. Holt, 1976; Millstone Hill Thomson scatter results for 1970, Technical Rep. No 522, MIT Lincoln Lab.

Evans, J.V., R.F. Julian, and W.A. Reid, 1970; Incoherent scatter measurements of F-region densities, temperature, and vertical velocity at Millstone Hill, Tech. Rep. No 477, MIT Lincoln Lab.

Farley, D.T., 1969; Incoherent scatter correlation function measurements, Rad. Sc., 4, 935.

Fedder, J.A. amd P.M. Banks, 1972; Convective elctric fields and polar thermospheric winds, JGR, 77, 2328.

Fejer, J., 1960; Scattering of radiowaves by an ionized gas in thermal equilibrium, JGR, 65, 2635.

Francis, S.H., 1975; Global propagation of atmospheric gravity waves; A review, JATP, 37, 1011.

Geisler, J.E., 1967; A numerical study of the wind system in the middle thermosphere, JATP, 29, 1469.

Harris, I. and H.G. Mayr, 1975; Thermospheic dynamics, I, theoretical formulation, JGR, 80, 3925.

Hays, P.B. and R.G. Roble, 1971; Direct observations of thermospheric winds during geomagnetic disturbances, JGR, 76, 5316.

_____, 1977; Thermospheric winds at high latitudes, EØS, 58, 1197 (abstract).

Hays, P.B., R.A. Jones, and M.H. Rees, 1975; Auroral heating and the composition of the neutral atmosphere, PSS, 21, 559.

Hedin, A.E., H.G. Mayr, C.A. Reber, N.W. Spencer, and G.R. Carignan, 1972; Empirical model of global thermospheric temperature and composition based on data from the OGO-6 quadropole mass spectrometer, NASA Rep. X-621-72-103, Goddard Sp Flght Ctr, Greenbelt, MD, 13pp.

_____, 1974; _____, JGR, 79, 215.

Hedin, A.E., H.G. Mayr, and I. Harris, 1977; Altitude profiles of the diurnal and semidiurnal variations of N_2, O, and He for the AE-E satellite, EØS, 58, 456.

Hedin, A.E., J.E. Salah, J.V. Evans, C.A. Reber, G.P. Newton, N.W. Spencer, D.C. Kayser, D. Alcayde, P. Bauer, L. Cogger, and J.P. McClure, 1977; A global thermospheric model based on mass spectrometer and incoherent scatter data MSIS 1. N_2 density and temperature, JGR, 82, 2139.

Hedin, A.E., C.A. Reber, G.P. Newton, N.W. Spencer, H.C. Brinton, H.G.
Mayr, and W.E. Potter, 1977; A global thermospheric modle based
on mass spectrometer and incoherent scatter data (MSIS), 2,
composition, JGR, 82, 2148.

Hedin, A.E., P. Bauer, H.G. Mayr, G.R. Carignan, L.H. Brace, H.C. Brin-
ton, A.D. Parks, D.T. Delz, 1977; Observations of neutral composi-
tions and related ionospheric variations during a magnetic storm
in Fegruary, 1974, JGR, 82, 3183.

Hernandez, G. and R.G. Roble, 1976a; Direct measurements of nighttime
thermospheric winds and temperatures 1. seasonal variations during
geomagnetic quiet periods, JGR, 81, 2065.

_____, 1976b; Direct measurements of nighttime
thermospheric winds and temperatures 2. geomagnetic storms, JGR,
81, 5173.

_____, 1977; Direct measurements of nighttime
thermospheric winds and temperatures 3. monthly variations during
solar minimum, JGR, 82, 5505.

Hinteregger, H.E., 1970; The extreme ultraviolet solar spectrum and its
variation during a solar cycle, Ann. Geophys., 26, 547.

_____, 1976; EUV fluxes in the solar spectrum below 2000Å,
JATP, 38, 791.

Horowitz, J.L., J.R. Doupnik and P.M. Banks, 1978; Chatanika radar abser-
vations of the latitudinal distributions of auroral zone electric
fields, conductivities, and currents, JGR, 83, 1463.

Horowitz, J.L., J.R. Doupnik, P.M. Banks, Y. Kamide, and S.-I. Akasofu,
1978; The latitudinal distributions of auroral zone electric fields
and ground magnetic perturbations and their response to variations
in the interplanetary magnetic field, JGR, 83, 2071.

Jacchia, L.G., 1965; Density variations in the heterosphere, Smith.
Astro. Obs. Spec. Rep. No 184, Cambridge, MA, 24 pp.

_____, 1971; Revised static models of the thermosphere and exo-
sphere with empirical termperature profiles, Special Rep.332, Smith.
Astro. Obs., Cambridge, MA.113 pp.

Jacchia, L.G., J.W. Slowey , and U. von Zahn, 1977; Temperature, density
and composition in the disturbed thermosphere from Esro 4 gas analyzer
measurements; a global model, JGR, 82, 684.

Kane, R.P. 1973; Storm-time variation of F2 region, Ann. Geophys., 29, 25.

Kelley, M.C., T.S. Jorgensen and I.S. Mikkelsen, 1977; Thermospheric
wind measurements in the polar region, JATP, 39, 211.

King, J.W., H. Kohl and R. Pratt, 1967; The effect of the atmospheric winds on the F2 layer peak at middle and high latitudes, JATP, 29, 1529.

Kirchhoff, V.W.J.H. and L.A. Carpenter, 1975; Dominance of the diurnal mode of horizontal drift velocites at F-region haights, JATP, 37, 419.

_____, 1976; The day-to-day variability in ionospheric electric fields and currents, JGR, 81, 2737.

Kohl, H. and J.W. King, 1967; Atmospheric winds between 100 and 700 km and their effects on the ionosphere, JATP, 29, 1045.

Maeda, H., 1976; Neutral winds and ion drifts in the polar ionosphere caused by convection electric fields - 1, JATP, 38, 197.

_____, 1977 Neutral winds and ion drifts in the polar ionosphere caused by convection electric fields - 2, JATP, 39, 849.

Marcos, F.A., H.B. Garrett, and K.S.W Chapman, 1977, Density variations in the lower thermosphere from analysis of the AE-C accelerometer measurements, PSS, 25, 499.

Mayr, H.G. and I. Harris, 1977; Diurnal variations in the thermosphere 2. temperatrue, composition and winds, JGR, 82, 2628.

_____, 1978; Some characteristics of electric field momentum coupling with the neutral atmosphere, JGR, 83, 3327.

Mayr, H.G. and A.E. Hedin, 1977; Significance of large scale circulation in magnetic storm characteristics with application to AE-C neutral compostion data, JGR, 82, 1227.

Mayr, H.G. and H. Volland, 1972; Theoretical model for the thermospheric annual and semiannual variations, JGR, 77, 6774.

_____, 1973; Magnetic storm characteristics of the thermosphere, JGR, 78, 2251.

Mayr, H.G., I. Harris and N.W. Spencer, 1978; Some properties of upper atmospheric dynamics, Submitted to Rev. Geophys. Sp. Sc.

Meriwether, J.W., J.P. Heppner, J.D. Stolarski and E.M. Wescott, 1973; Neutral winds above 200 km at high latitudes, JGR, 78, 6643.

Nagy, A.F., R.J. Cicerone, P.B. Hays, K.D. McWatters, J.W. Meriwether, A.E. Belon, and C.L. Rino, 1974; Simultaneous measurements of ion and neutral wind motions by radar and optical technique, Rad. Sc., 9, 315.

Nisbet, J.S., 1967, Neutral atmospheric temperature from incohernt scatter observations, J. Atmos. Phys., 24, 586.

Nisbet, J.S., 1970;"Penn State Ionospheric Model," ISR Rep. No. 355, Pennsylvannia State University, PA.

Nisbet, J.S. and D.A. Glenar, 1977, Thermospheic meridional winds and atomic oxygen depletion at high latitudes, JGR, 82, 4685.

Nisbet, J.S., B.J. Wydia, C.A. Reber and J.M. Luton, 1977; Global exospheric temperatures and densities under active solar conditions, PSS, 25, 59.

Novikov, V.M., 1976; Ionospheric substorm developement in the post-modnight sector, Aero.& Geo., __, 434.

Noxon, J.F. and J.V. Evans, 1976; Simultaneous potical and incoherent scatter observations of two low latitudinal auroras, PSS, 24, 425.

Oliver, W.L., R.H. Wand, and J.V. Evans, 1977; Millstone Hill exospheric temperatures at solar minimum, EØS, 58, 1197 (abstract).

Olson, W.P. and K. Moe, 1974; Influence of predipitating charged particles on the high latitude thermosphere, JATP, 36, 1715.

Park, C.G. 1973; Whistler observations of the depletion of the plasmasphere during a magnetospheric substorm, JGR, 78, 672.

_____, 1974; A morphological study of substorm associated disturbances in the ionosphere, JGR, 79, 2821.

_____, 1976; Substorm electric fields in the evening plasmsphere and their effects on the underlying F-layer, JGR, 81, 2283.

_____, 1977; Whistler observations of substorm electric fields in the plasmasphere, EØS, 85, 752 (abstract).

Park, C.G. and C.-I. Meng, 1971; Vertical motions of the mid-latitude F2 layer during magnetospheric substorms, JGR, 76, 8326.

_____, 1976; After effects of isolated magnetospheric substorm activity on the mid-latitude ionosphere: localized depressions in F-layer electron densities, JGR, 81, 4571.

Prolss, G.W., 1977; Seasonal variations of atmospheric-ionospheric disturbances, JGR, 82, 1635.

Prolss, G.W. and U. von Zahn, 1977; Seasonal variations in the latitudinal atructure of atmospheric disturbances, JGR, 82, 5629.

Raitt, W.J., U. von Zahn, and P. Christophersen, 1975; A comparison of thermospheric neutral gas heating and related thermal and energetic plasma phenomena at high latitudes during geomagnetic disturbances, JGR, 80, 2277.

Ratcliffe, J.A. and K. Weekes, 1960; "The Ionosphere," Physics of the Upper Atmosphere, J.A. Ratcliffe, ed., Academic Press.

Reber, C.A., 1976; Dynamical effects in the distribution of helium in the thermosphere, JATP, 38, 829.

Richmond, A.D., 1978; Large-amplitude gravity wave energy production and dissipation in the thermosphere, sumitted to JGR.

_____, 1976; Electric fields in the ionosphere and plasmasphere on quiet days, JGR, 81, 1447.

Richmond, A.D. and S. Matsushita, 1975; Thermospheric response to a magnetic substorm, JGR, 80, 2839.

Richmond, A.D., S. Matsushita, and J.D. Tarpley, 1976; On the production mechanism of electric currents and fields in the ionosphere, JGR, 81, 547.

Rishbeth, H., 1975; F-region storms and thermospheric circulation, JATP, 37, 1055.

Rishbet, H. and O.K. Garriott, 1969, Introduction to Ionospheric Physics, Academic Press, New York, 331 pp.

Roble, R.G., 1975; The calculated and observed diurnal variation of the ionosphere over Millstone Hill on 23-24 Mar 1970, PSS, 23, 1017.

_____, 1977; "The Thermosphere," The Upper Atmosphere and Magnetosphere, National Academy of Science, Washington, D.C.

Roble, R.G. and S. Matsushita, 1975; An extimate of the global scale Joule heating rates in the thermosphere due to time mean currents, Rad. Sc., 10, 389.

Roble, R.G., R.E. Dickinson and E.C. Ridley, 1977; Seasonal and solar cycle variations of the zonal mean circulation in the thermosphere, JGR, 82, 5493.

Roble, R.G., Salah. J.E. and B.A. Emery, 1977; The seasonal variation of the diurnal thermospheric winds over Millstone Hill during solar cycle maximum, JATP, 39, 503.

Roble, R.G., B.A. Emery, J.E. Salah, and P.B. Hays, 1974; Dirunal variation of the neutral thermospheric winds determined from incoherent scatter radar data, JGR, 79, 2868.

Roble, R.G. A.D. Richmond, W.L. Oliver, and R.M. Harper, 1978; Ionospheric effects of the gravity wave launched by the Sep 18, 1974 sudden commencement, JGR, 83, 999.

Roper, D.W. and A.J. Baxter, 1978; The effect of auroral energy input on neutral and ion drifts in the thermosphere, JATP, 40, 585.
189

Rothwell, P., R. Mountford and G. Martinelli, 1974; Neutral wind modifications above 150 km altitude associated with the polar substorm, JATP, 36, 1915.

Salah, J.E., 1972; A study of the midlatitude thermosphere by incoherent scatter radar, ScD. Thesis, MIT.

Salah, J.E. amd J.V. Evans, 1973; Measurements of thermospheric temperatures by incoherent scatter radar, Space Res. XII, 267.

Salah, J.E. and Holt, J.M., 1974; Mid-latitude thermospheric winds from incoherent scatter radar theory, Rad. Sc., 9, 301.

Sastri, J.H. and J.E. titheridge, 1977; Depressions in mid-latitude F-region under relatively quiet geomagnetic conditions, JATP, 39, 1307.

Sharp, L.R., D.R. Hidman, C.J. Rice and J.M. Straus, 1978; The altitude dependence of the local time variation of thermospheric density, Geo. Res. Ltr., 5, 261.

Spencer, N.W., 1977; Winds and temperatures in the thermosphere, Proc. of Atmos. Explorer Results, Bryse Mt., Va.

Spurling, P.H. and K.L. Jones, 1976, The observation of related F-region height and electron content changes at mid-latitudes during magnetic storms and their comparison with a numerical model, JATP, 38, 1237.

Straus, J.M., 1978; Dynamics of the thermosphere at high latitudes, Rev. of Geo. & Sp. Phys., 16, 183.

Straus, J.M. and L.A. Christopher, 1978; Dynamical effects on the global distribution of thermospheric atomic oxygen, Aerospace Corp. Rep. No. ATR-78(8203)-3.

Straus, J.M. and Schulz, M., 1976; Magneotspheric convection and upper atmospheric dynamics, JGR, 81, 5822.

Straus, J.M., S.P. Creekmore, R.M. Harris, B.K. Ching, and Y.T. Chiu, 1975a; Aglobal model of thermospheric dynamics - II wind, density and temperature fields generated by EUV heating, JATP, 37, 1245.

Straus, J.M.S.P., S.P. Creekmore, R.M. Harris, and B.K. Ching, ;975b; Effects of heating at high latitudes on global thermospheric dynamics, JATP, 37, 1545.

Stubbe, P., 1968; Frictional forces and collision frequencies between moving ion and neutral gases, JATP, 30, 1965.

_____, 1975; The effect of neutral winds on the seasonal F-region variation, JATP, 37, 675.

Stubbe, F
PSS,

Taeusch,
the

Testud, J
of a

Titheridg
slef

Trinks, H
lite
stor

Trinks, H
disp
by E

Trinks, H
comp
rock

Van Zandt
of t

Vasseur,
l at

von Zahn,
sphe
time
Phys

Watkins,
ther
tion

Wedde, T.
the
tati

Wand, R.H
turb

MICROCOPY RESOLUTION TEST CHART
NATIONAL BUREAU OF STANDARDS-1963-A

Stubbe, P. and S. Chandra, 1971; Ionospheric warming by neutral winds, PSS, 19, 731.

Taeusch, D.R., 1977; Structure of electrodynamic and particle heating in the disturbed polar thermosphere, JGR, 82,455.

Testud, J., P. Amayenc and M. Blanc, 1975; Middle and low latitude effect-of auroral disturbances from incoherent radar, JATP, 37, 989.

Titheridge, J.E., 1976; Ionospheric heating beneath the magnetospheric sleft, JGR, 81, 3221.

Trinks, H., S. Chandra, N.W. Spencer and U. von Zahn, 1976; A two-satel-lite study of the neutral atmosphere reponse to a major geomagnetic storm, JGR, 81, 5013.

Trinks, H., H.G. Mayr, D.C. Kayser, and W.E. Potter, 1977; Auroral energy disposition and neutral composition changes observed simultaneously by Esro 4 and AE-C at different sltitudes, JATP, 39, 287.

Trinks, H., D. Offerman, U. von Zahn and C. Steinhauer, 1978; Neutral composition measurements between 90- and 220- km altitude by a rocket borne mass spectrometer, JGR, 83, 2169.

Van Zandt, T.E., V.L. Peterson and A.R. Laird, 1971; Electromagnetic drift of the mid-latitude F2 layer during a storm, JGR, 76, 278.

Vasseur, G., 1969; Dynamics of the F-region observed with Thomson scatter 1 atmospheric circulation and neutral winds, JATP, 31, 397.

von Zahn, U. and K.H. Fricke, 1978; Empirical models of global thermo-spheric composition and temperature during geomagnetically quiet times compared with Esro 4 gas analyzer data, Rev. Geophys. Sp. Phys., 16, 169.

Watkins, B.J. and P.M. Banks, 1974; A preliminary study of high latitude thermospheric temperatures from incoherent scatter radar observa-tions, JGR, 79, 5307.

Wedde, T., J.R. Doupnik and P.M. Banks, 1977; Chatanika observations of the latitudinal structure of electric fields and particle precipi-tation on November 21, 1975, JGR, 82, 2743.

Wand, R.H., 1978; Average electric fields at Millstone for quiet and dis-turbed conditions, EØS, 59, 338 (abstract).